TUNABLE OPTICAL PROPERTIES OF Dy^{3+}; Eu^{3+} DOPED, Dy^{3+}/ Bi^{3+}; Dy^{3+} /Ce^{3+};Dy^{3+}/ Eu^{3+}; Tb^{3+} /Ce^{3+} CODOPED $LaBO_3$

A THESIS SUBMITTED TO
THE GRADUATE SCHOOL OF NATURAL AND APPLIED
OF
MIDDLE EAST TECHNICAL UNIVERSITY

BY

ÖZDE CEREN HIZAL ABACI

IN PARTIAL FULFILLMENT OF THE REQUIREMENTS
FOR
THE DEGREE OF MASTER OF SCIENCE
IN
CHEMISTRY

AUGUST 2017

Approval of the thesis:

TUNABLE OPTICAL PROPERTIES OF Dy^{3+}; Eu^{3+} DOPED, Dy^{3+}/ Bi^{3+}; Dy^{3+}/Ce^{3+}; Dy^{3+}/Eu^{3+}; Tb^{3+} /Ce^{3+} CODOPED *$LaBO_3$*

submitted by **ÖZDE CEREN HIZAL ABACI** in partial fulfillment of the requirements for the degree of **Master of Science in Chemistry Department, Middle East Technical University** by,

Prof. Dr. Gülbin Dural Ünver _____
Dean, Graduate School of **Natural and Applied Sciences**

Prof. Dr. Cihangir Tanyeli _____
Head of Department, **Chemistry Department**

Prof. Dr. Ayşen Yılmaz _____
Supervisor, **Chemistry Department, METU**

Assoc. Prof. Dr. Okan Esentürk _____
Co-Supervisor, **Chemistry Department, METU**

Examining Committee Members

Prof. Dr. Nurşen Altuntaş Öztaş _____
Chemistry Department, Hacettepe Uni.

Prof. Dr. Ayşen Yılmaz _____
Chemistry Department, METU

Assoc. Prof. Dr. Okan Esentürk _____
Chemistry Department, METU

Prof. Dr. Enver Bulur _____
Physics Department, METU

Prof. Dr. Ceyhan Kayran İşçi _____
Chemistry Department, METU

Date: **10.08.2017**

I hereby declare that all information in this document has been obtained and presented in accordance with academic rules and ethical conduct. I also declare that, as required by these rules and conduct, I have fully cited and referenced all material and results that are not original to this work.

Name & Last Name: Özde Ceren Hızal Abacı

Signature:

ABSTRACT

TUNABLE OPTICAL PROPERTIES OF Dy^{3+}; Eu^{3+} DOPED, Dy^{3+}/ Bi^{3+}; Dy^{3+} /Ce^{3+}; Dy^{3+}/ Eu^{3+}; Tb^{3+} /Ce^{3+} CODOPED $LaBO_3$

Abacı Hızal, Özde Ceren

M. Sc. Department of Chemistry

Supervisor: Prof. Dr. Ayşen Yılmaz

Co-Supervisor: Assoc. Prof. Dr. Okan Esentürk

August 2017, 103 pages

In recent years, light emitting materials especially trivalent rare earth ions (RE^{3+}) doped inorganic borate phosphors have attracted much attention due to their useful applications in several fields, which include flat panel displays, white light emitting diodes (WLEDs), solar cells, thermoluminescence dosimeters.

In this research, single phase Dy^{3+}; Eu^{3+} doped Dy^{3+}/ Bi^{3+}; Dy^{3+}/ Ce^{3+}; Dy^{3+}/ Eu^{3+}; Tb^{3+}/ Ce^{3+} codoped lanthanum orthoborate phosphors were prepared by microwave assisted solid state synthesis method using metal oxides and carbonates as initial reactants. This method is preferential for us because previous microwave treatment of mixture before heating sample at high temperature in furnace reduces duration of heat and leads to produce fine powders.

Crystal structure, morphology, vibrational band modes, low frequency vibrational modes, photoluminescence properties of all synthesized phosphors were investigated by X-Ray Diffraction (XRD), Scanning Electron Microscope (SEM), Attenuated

Total Reflectance (ATR), Far Infrared (Far-IR), Fluorescence spectrometers, respectively. The colors of phosphors were detected with CIE 1931 color space chromaticity coordinates and photographs of materials were taken under 355 nm excitation.

The XRD patterns prove that undoped, single doped and codoped $LaBO_3$ powder crystalline samples were prepared successfully. Except high doping concentrations of Ce^{3+} ions that lead to observation of XRD pattern of $CeBO_3$ with very low intensities, no significant changes are observed in the patterns of doped $LaBO_3$ products. SEM images of synthesized materials show that fine particle size and regular morphology were obtained. ATR spectra of the products support the formation of planar borate units (BO_3^{3-}). Far-IR spectra showed the variation in low frequency vibrational modes $LaBO_3$ with various type and amounts of doping. Results of the luminescence studies showed that optical properties of samples can be tuned by codoping. Especially, Dy^{3+}/ Ce^{3+} and Tb^{3+}/ Ce^{3+} codoped samples had highest luminescence intensity among the all synthesized phospors. Moreover, Luminescence lifetimes were recorded at the highest emission bands in order to explain possible energy transfer mechanisms. Emission colors of phosphors were presented as red, pale yellow, white, green and yellow-orange, for Eu^{3+} doped; Dy^{3+} doped and Dy^{3+}/ Bi^{3+} codoped; Dy^{3+}/ Ce^{3+}; Tb^{3+}/ Ce^{3+}; Dy^{3+}/ Eu^{3+} codoped phosphors respectively.

Keywords: Lanthanum orthoborate, cerium, dysprosium, europium, terbium, rare earth luminescence, urea, color, microwave assisted solid state synthesis.

ÖZ

Dy^{3+}; Eu^{3+} TEKLİ, Dy^{3+}/ Bi^{3+}; Dy^{3+} /Ce^{3+}; Dy^{3+}/ Eu^{3+}; Tb^{3+} /Ce^{3+} İKİLİ KATKILI $LaBO_3$ ORTOBORATLARIN AYARLANABİLİR OPTİK ÖZELLİKLERİNİN ARAŞTIRILMASI

Abacı Hızal, Özde Ceren

Yüksek Lisans, Kimya Bölümü

Tez Yöneticisi: Prof. Dr. Ayşen Yılmaz

Ortak Tez Yöneticisi: Doç. Dr. Okan Esentürk

Ağustos 2017, 103 Sayfa

Son yıllarda, özellikle üç değerlikli nadir toprak iyonları (NT^{3+}) katkılı inorganik borat fosforları; ışık yayan malzemeler, düz panel ekranlar, beyaz ışık yayan diyotlar (WLED), güneş hücreleri, termolüminesans gibi çeşitli alanlarda faydalı uygulamaları nedeniyle çok dikkat çekmektedir.

Bu araştırmada tek fazlı Dy^{3+}; Eu^{3+} tekli, Dy^{3+}/ Bi^{3+}; Dy^{3+}/ Ce^{3+}; Dy^{3+}/ Eu^{3+}; Tb^{3+}/ Ce^{3+} ikili katkılı lantan ortoborat fosforları, ilk tepken maddeler olarak metal oksitler ve karbonatlar kullanılarak mikrodalga yardımlı katı hal sentezi yöntemi ile hazırlandı. Yüksek sıcaklıkta fırınlanmadan önce mikrodalga fırında ısıtılması, fırınlanma süresini kısaltarak enerji tasarrufu sağlamakla birlikte küçük toz kristaller üretmeyi mümkün kılar. Malzemelerin kristal yapısı, morfolojisi, anyonik gruplarının titreşim bant modları, düşük frekans bant modları, fotolüminesans özellikleri sırasıyla X ışınları toz kırınımı (XRD), taramalı elektron mikroskobu (SEM), zayıflatılmış toplam yansıma (ATR), uzak kızılötesi (Far-Ir) ve flüoresans

spektrometreler yardımıyla araştırılmıştır. CIE 1931 hesaplamalarıyla fosforların renk koordinatları belirlenmiştir.

Ayrıca, 355 nm dalga boyu eksitasyonu altında fosforların fotoğrafları çekilmiştir.

XRD desenleri katkısız, tek katkılı ve ikili katkılı $LaBO_3$ toz malzemelerin başarılı bir şekilde sentezlendiğini göstermektedir. Katkılayıcı olarak yüksek konsantrasyonlarda Ce^{3+} iyonları içeren XRD desenleri küçük şiddetlerde $CeBO_3$ içermesine rağmen, diğer desenlerde ciddi bir değişim gözlenmemiştir. SEM görüntüleri ürünlerin ince tanecik boyutu ve düzenli morfolojiye sahip olduğunu göstermektedir. ATR sonuçları lantan ortoboratın sahip olduğu düzlemsel borat (BO_3^{3-}) yapısını kanıtlamıştır. Far-IR spektrumları lantan boratın düşük frekanstaki salınım bantlarını içermektedir. Bu bantlardaki değişimlere bakılarak katkılamanın türü araya girme veya yer değiştirme olarak belirlenebilir. Lüminesans çalışmaları lüminesans şiddetinin ikili katkılamalarla ayarlanabilir olduğunu göstermiştir. Özellikle Dy^{3+}/ Ce^{3+} ve Tb^{3+}/ Ce^{3+} ikili katkılamalarının en yüksek lüminesans şiddetlerine sahip olduğu kaydedilmiştir. Ek olarak, fosforların lüminesans ömürleri sahip oldukları en yüksek emisyon bantlarına göre, olası enerji transfer mekanizmalarını açıklamak için kaydedilmiştir. Fosforların ışıma renkleri Eu^{3+} katkılı, Dy^{3+} katkılı ve Dy^{3+}/ Bi^{3+} ikili katkılı, Dy^{3+}/ Ce^{3+}; Tb^{3+}/ Ce^{3+}; Dy^{3+}/ Eu^{3+} ikili katkılamaları için sırasıyla kırmızı, açık sarı, beyaz, yeşil ve sarı-turuncu olarak hesaplanmış ve fotoğrafları ile uyumlu sonuçlar elde edilmiştir.

Anahtar Sözcükler: Lantan ortoborat, seryum, disprosyum, terbiyum, öropiyum, lüminesans, üre, mikrodalga yardımlı katı hal sentezi.

To my parents Fevzi and Demet, my sister Sabiha, and my husband Afşin

ACKNOWLEDGEMENTS

I would like to thank my advisor Prof. Dr. Ayşen Yılmaz and co-advisor Assoc. Prof. Dr. Okan Esentürk for their invaluable guidance with full support, comments and insights as well as patience during the study.

I would like to express my gratitude for Prof. Dr. Ahmet M. Önal, Prof. Dr. Enver Bulur, and Assoc. Prof. Dr. Alpan Bek for their assistance by letting me to utilize their research laboratory during the study.

I would like to thank Diren Maraba for decay curve measurements and Kurtuluş Abak for his cooperation and understanding.

I would like to give my dearest thanks to my lab mates Sera İflazoğlu, Zeynep Seda Eren, Pelin Akman, M. Gencay Çelik, Ali Farid and Metehan Severoğlu for their support and the shared memories.

I would like to thank Öykü Yıldırım, Seza Göker, Ozan Erlik for their lovely friendship and sharing years together. They were always with me whenever I need them.

I would like to thank Belde Bayındırlı for her beautiful friendship, relaxing conversations, understanding. She reminds me the meaning of sisterhood.

I owe my special thanks to Afşin Abacı for his true love, patience, support and especially for always holding my hand to overcome the difficulties. I believe I can cope with anything as long as he is right beside me.

Special thanks go to Sabiha Hızal, my other half, my sister. She makes my life meaningful and easier. I cannot imagine a life without her.

I want to give the best love and gratitude to my mother and father. Without their love, support, I could not succeed anything.

TABLE OF CONTENTS

ABSTRACT v

ÖZ vii

ACKNOWLEDGEMENTS x

LIST OF TABLES xiv

LIST OF FIGURES xv

CHAPTERS 1

1.INTRODUCTION 1

1.1 Properties and applications of phosphors 1

1.2 Luminescence 4

1.3 Rare earth elements: general characterization 5

1.3.1 Photoluminescence properties of Dysprosium ions (Dy^{3+}) 9

1.3.2 Photoluminescence properties of Terbium ions (Tb^{3+}) 10

1.3.3 Photoluminescence properties of Europium ions (Eu^{3+}) 11

1.3.5 Energy transfer mechanisms 14

1.4 Photoluminescence decay lifetimes 16

1.5 Chromaticity coordinates 17

1.6 Host materials 19

1.6.1 Borates 19

1.6.2 Crystal structure and IR studies of $LaBO_3$ 21

1.7 Synthesis methods 22

1.8 Aim of the study 25

2. MATERIALS AND METHOD 27
2.1 Materials 27
2.2 Instrumentation 28
2.2.1 Furnace 28
2.2.2 Powder X-ray diffraction (XRD) 28
2.2.3 Attenuated total reflectance- fourier transform infrared spectrometer (ATR- FTIR) 28
2.2.4 Far-IR spectrometer 28
2.2.5 Luminescence spectrometer 29
2.2.6 Scanning electron microscope (SEM) 29
2.2.7 Luminescence lifetime measurement 29
2.2.8 Laser source for photoshoot 29
2.3. Synthesis of codoped $LaBO_3$ powders 30
3. RESULTS AND DISCUSSION 35
3.1 X-ray Diffraction Patterns of undoped, doped, codoped $LaBO_3$ 35
3.2 SEM images of undoped, doped, codoped $LaBO_3$ 40
3.3 ATR-FTIR spectra of undoped, doped, codoped $LaBO_3$ 42
3.4 Far- IR results of undoped, doped, codoped $LaBO_3$ 49
3.5 Photoluminescence (PL) results of undoped, doped, codoped $LaBO_3$ 58
3.6 CIE results of doped, codoped $LaBO_3$ 71
3.7 Decay curves of undoped, doped, codoped $LaBO_3$ 77
4. CONCLUSION 85
REFERENCES 89
APPENDICES 95
A.Luminescence intensity comparision of microwave assisted solid state synthesis and solid state synthesis without urea 95

B.Luminescence intensity comparision of $Dy_{0.07}La_{0.93}BO_3$ and $Dy_{0.09}Ce_{0.05}La_{0.88}BO_3$ 97

C. Luminescence intensity comparision of $Tb_{0.07}La_{0.93}BO_3$ and $Tb_{0.07}Ce_{0.05}La_{0.88}BO_3$ 99

D.Summary of double exponential decay function fit parameters 101

E. Summary of single exponential decay function fit parameters 103

LIST OF TABLES

TABLES

Table 1. Electronic configurations and ground state terms symbols of RE^{3+} 6
Table 2. Distribution of boron reserves. 20
Table 3. Used materials, their intended purpose and labels 27
Table 4. Stoichiometric amounts of Dy^{3+} doped $LaBO_3$ 30
Table 5. Stoichiometric amounts of Eu^{3+} doped $LaBO_3$ 31
Table 6. Stoichiometric amounts of Dy^{3+}/ Bi^{3+} codoped $LaBO_3$ 31
Table 7. Stoichiometric amounts of Dy^{3+}/ Ce^{3+} codoped $LaBO_3$ 32
Table 8. Stoichiometric amounts of Dy^{3+}/ Ce^{3+} codoped $LaBO_3$ 32
Table 9. Stoichiometric amounts of Dy^{3+}/ Eu^{3+} codoped $LaBO_3$ 32
Table 10. Stoichiometric amounts of Tb^{3+}/ Ce^{3+} codoped $LaBO_3$ 33
Table 11. Moles and weight of used materials for pure $LaBO_3$ and pure $CeBO_3$ 33
Table 12. Reported decay times of Dy^{3+}, Eu^{3+}, Tb^{3+} emissions in different hosts. 77
Table 13. Summary of the exponential fit function parameters and their errors 78
Table D.1. Double exponential decay function fit parameters..... 101
Table E.1. Single exponential deceay function fit parameters..... 103

LIST OF FIGURES

Figure 1. Phosphor compositions [5] 2
Figure 2. Application fields of phosphor devices [3]..... 3
Figure 3. Jablonski diagram [8] 4
Figure 4. Energy levels of RE^{3+} ions (Reproduced with permission [14]) 8
Figure 5. Energy level diagram of of Dy^{3+} ions. (Reproduced with permission [20])10
Figure 6. Energy level diagram of Tb^{3+} ions..... 11
Figure 7. Energy level diagram of Eu^{3+} ions..... 12
Figure 8. Excited 5d energy levels of Ce^{3+} in several host matrixes [3]..... 13
Figure 9. Excitation and Emission spectra of Ce^{3+} ions (Reproduced with permission [28]) 14
Figure 10. Energy level diagram of the possible energy transition mechanisms a) from Ce^{3+} to Dy^{3+} ion (Reproduced with permission [28]), b) Dy^{3+} to Eu^{3+} ion, and c) from Ce^{3+} to Tb^{3+}ion 16
Figure 11. CIE chromaticity diagram (left) and color matching functions (right) [34]18
Figure 12. Crystal structure refinement and data of Lanthanum orthoborates [53]... 21
Figure 13. Crystal structure of $LaBO_3$ [53]. 22
Figure 14. XRD patterns of undoped and Dy^{3+} doped $LaBO_3$..... 36
Figure 15. XRD patterns of undoped and Eu^{3+} doped $LaBO_3$ 36
Figure 16. XRD patterns of undoped and Dy^{3+}/Bi^{3+} codoped $LaBO_3$. 37
Figure 17. XRD patterns of $CeBO_3$, undoped, and Dy^{3+}/Ce^{3+} codoped $LaBO_3$.
40 Figure 18. XRD patterns of $CeBO_3$, undoped, and Dy^{3+}/Ce^{3+} codoped $LaBO_3$. .. 38
Figure 19. XRD patterns of undoped and Dy^{3+}/ Eu^{3+} codoped $LaBO_3$..... 39
Figure 20. XRD patterns of $CeBO_3$, undoped, and Tb^{3+}/Ce^{3+} codoped $LaBO_3$..... 39
Figure 21. SEM images of a) undoped, b) Dy^{3+} doped, c) Dy^{3+}/ Ce^{3+} codoped, d)Dy^{3+}/ Eu^{3+} codoped, e) Dy^{3+}/ Bi^{3+} codoped, f) Tb^{3+}/ Ce^{3+} codoped $LaBO_3$ materials 41
Figure 22. ATR spectra of undoped and Dy^{3+} doped $LaBO_3$ materials. 42

Figure 23. ATR spectra of undoped and Eu^{3+} doped $LaBO_3$ materials. 43
Figure 24. ATR spectra of undoped and Dy^{3+}/ Bi^{3+} codoped $LaBO_3$ materials..... 44
Figure 25. ATR spectra of undoped and Dy^{3+}/Ce^{3+} codoped $LaBO_3$ materials..... 45
Figure 26. ATR spectra of undoped and Dy^{3+}/Ce^{3+} codoped $LaBO_3$ materials..... 46
Figure 27. ATR spectra of undoped and Dy^{3+}/ Eu^{3+} codoped $LaBO_3$ materials..... 47
Figure 28. ATR spectra of undoped and Tb^{3+}/Ce^{3+} codoped $LaBO_3$ materials. 48
Figure 29. Far-IR spectra of undoped and Dy^{3+} doped $LaBO_3$ materials. 49
Figure 30. Far-IR spectra of undoped and Eu^{3+} doped $LaBO_3$ materials..... 51
Figure 31. Far-IR spectra of undoped and Dy^{3+}/Bi codoped $LaBO_3$ materials..... 52
Figure 32. Far-IR spectra of undoped and Dy^{3+}/Ce^{3+} codoped $LaBO_3$ materials. 53
Figure 33. Far-IR spectra of undoped and Dy^{3+}/Eu^{3+} codoped $LaBO_3$ materials 54
Figure 34. Far-IR spectra of undoped and Tb^{3+}/Ce^{3+} codoped $LaBO_3$ materials..... 55
Figure 35. Far-IR spectra of a) $TbBO_3$, b) $DyBO_3$, c) $CeBO_3$, d) $EuBO_3$ material ... 56
Figure 36. Far-IR spectra of oxides of rare earth elements and boric acid. 57
Figure 37. a) Excitation spectra, b) emission spectra of Dy^{3+} doped $LaBO_3$ materials59
Figure 38. a) Excitation spectra, b) emission spectra of Eu^{3+} doped $LaBO_3$ materials.61
Figure 39. a) Excitation spectra of Dy^{3+}/ Bi^{3+} codoped $LaBO_3$, b) emission spectra of 5 % Dy^{3+} and Dy^{3+}/ Bi^{3+} codoped $LaBO_3$ materials. 63
Figure 40. Excitation spectra of Dy^{3+}/ Ce^{3+} codoped $LaBO_3$ materials. 64
Figure 41. Emission spectra of Dy^{3+}/ Ce^{3+} codoped $LaBO_3$ materials..... 65
Figure 42. Emission spectra of Dy^{3+}/ Ce^{3+} codoped $LaBO_3$ materials..... 66
Figure 43. Excitation spectra of Dy^{3+}/ Eu^{3+} codoped $LaBO_3$ materials a) λ_{em} = 575 nm b) λ_{em} = 615 nm..... 67
Figure 44. Emission spectra of Dy^{3+}/ Eu^{3+} codoped $LaBO_3$ materials a) λ_{ex} = 351 nm b) λ_{ex} = 394 nm..... 68
Figure 45 Excitation spectra of a) Tb^{3+} doped, b) Tb^{3+}/ Ce^{3+} codoped $LaBO_3$ materials. 69
Figure 46. Emission spectra of a) Tb^{3+} doped (λ_{ex} = 378 nm) and b) Tb^{3+}/ Ce^{3+} codoped (λ_{ex} = 331 nm) $LaBO_3$ materials. 70
Figure 47. CIE coordinates and inset photographs of undoped, Dy^{3+} doped $LaBO_3$ materials. 71
Figure 48. CIE chromaticity and inset photographs of Eu^{3+} doped $LaBO_3$ materials 72

Figure 49. CIE chromaticity and inset photographs of Dy^{3+}/ Bi^{3+} codoped $LaBO_3$ materials. 73
Figure 50. CIE chromaticity and inset photographs of Dy^{3+}/ Ce^{3+} codoped $LaBO_3$ materials 74
Figure 51. CIE chromaticity and inset photographs of Dy^{3+}/ Eu^{3+} codoped $LaBO_3$ materials. 75
Figure 52. CIE chromaticity and inset photographs of Tb^{3+}/ Ce^{3+} codoped $LaBO_3$ materials. 76
Figure 53. Decay curve of Dy^{3+} doped $LaBO_3$ materials..... 79
Figure 54. Decay curve of Eu^{3+} doped $LaBO_3$ materials 79
Figure 55. Decay curve of Tb^{3+} doped $LaBO_3$ materials 80
Figure 56. Decay curve of Dy^{3+} / Ce^{3+} codoped $LaBO_3$ materials 81
Figure 57. Decay curve of Dy^{3+} / Eu^{3+} codoped $LaBO_3$ materials 82
Figure 58. Decay curve of Tb^{3+} / Ce^{3+} codoped $LaBO_3$ materials..... 82
Figure A.1. Emission spectra of Dy^{3+} doped $LaBO_3$ with and without urea ……....95
Figure B.1 Emission spectra of $Dy_{0.07}La_{0.93}BO_3$ and $Dy_{0.09}Ce_{0.05}La_{0.88}BO_3$ ...…….. 97
Figure C.1 Emission spectra of $Tb_{0.07}La_{0.93}BO_3$ and $Tb_{0.07}Ce_{0.05}La_{0.88}BO_3$ ……..…99

CHAPTER 1

INTRODUCTION

1.1 Properties and applications of phosphors

The term ‘phosphor’, which is invented in 17th century, refers to ‘light barrier’ in Greek language and still being used for luminescent or light emitting materials [1]. According to historical accounts, the first known phosphor material is barite ($BaSO_4$). It was explored by an alchemist Vinventinus Casciarolo of Bologna when he heated a shiny and crystal stone which was found in the volcano to obtain valuable metal. Although all his efforts, he could only obtain BaS product which emitted red light after exposure to sunlight instead of precious metal. Nowadays, this product is used as a host for luminescent materials. After its discovery, luminescent materials started to be named as phosphors [2].

Generally, phosphors are solid luminescent materials. There is no certain definition of the word ‘phosphor’ and it changes in accordance with the user objective. More particularly, it is used to refer inorganic phosphors which are usually synthesized in powder form to be used in practical applications. Although, many organic molecules, thin films, or single crystals exhibit luminescent property, they are rarely referred as ‘phosphor’ [3].

Phosphors are able to convert the radiation energy which is originated from excitations sources such as X-rays, cathode rays, UV light, heat etc. into near-ultraviolet, visible, or near-infrared light. Luminescent materials can be classified as host luminophores, host- activator type and host-activator-sensitizer type depending on their composition. The host-activator compositions are composed of inactive host

that is not able to emit light by itself e.g. $LaBO_3$ and luminescent ions which are named as activators. Activators e.g. rare earth ions, defects, s^2 valence shell electronic configuration ions, transition metal ions can emit light after exposure of excitation source. **Figure 1** represents the possible compositions in the periodic table. For example, although as a host material $LaBO_3$ does not show any luminescent character, Dy^{3+} doped $LaBO_3$ sample can emit light. In some cases, a sensitizer can be needed in composition. In the host-activator-sensitizer composition, sensitizers enhance luminescent properties of phosphors by absorbing the excitation energy and transferring it to activator ions. For instance, Ce^{3+} ion is useful sensitizer for Dy^{3+} and Tb^{3+} ions in the $LaBO_3$ host. In addition to these compositions, some host materials which are called as host luminophores i.e. vanadate, tungstate, and titanate etc. exhibit luminescent character thanks to their luminescent centers [4].

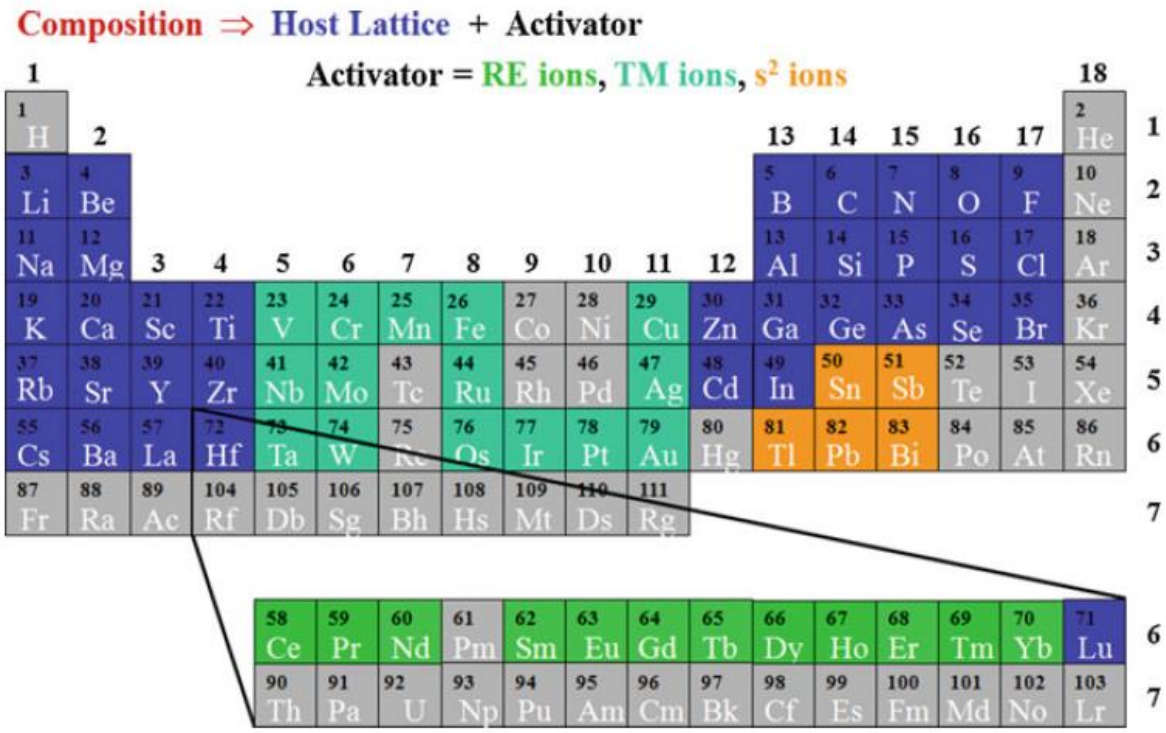

Figure 1. Phosphor compositions [5]

Luminescent materials have various application fields depending on their luminescence lifetimes and excitation sources. Phosphors are applied in cathode ray tubes (CRT), lamps, luminescent dosimeters, plasma displays etc. [6]

Figure 2 presents some possible usage of phosphor devices that is directly associated with their excitation source. Those devices are encountered in TV, laser, lamp, radar in the daily life.

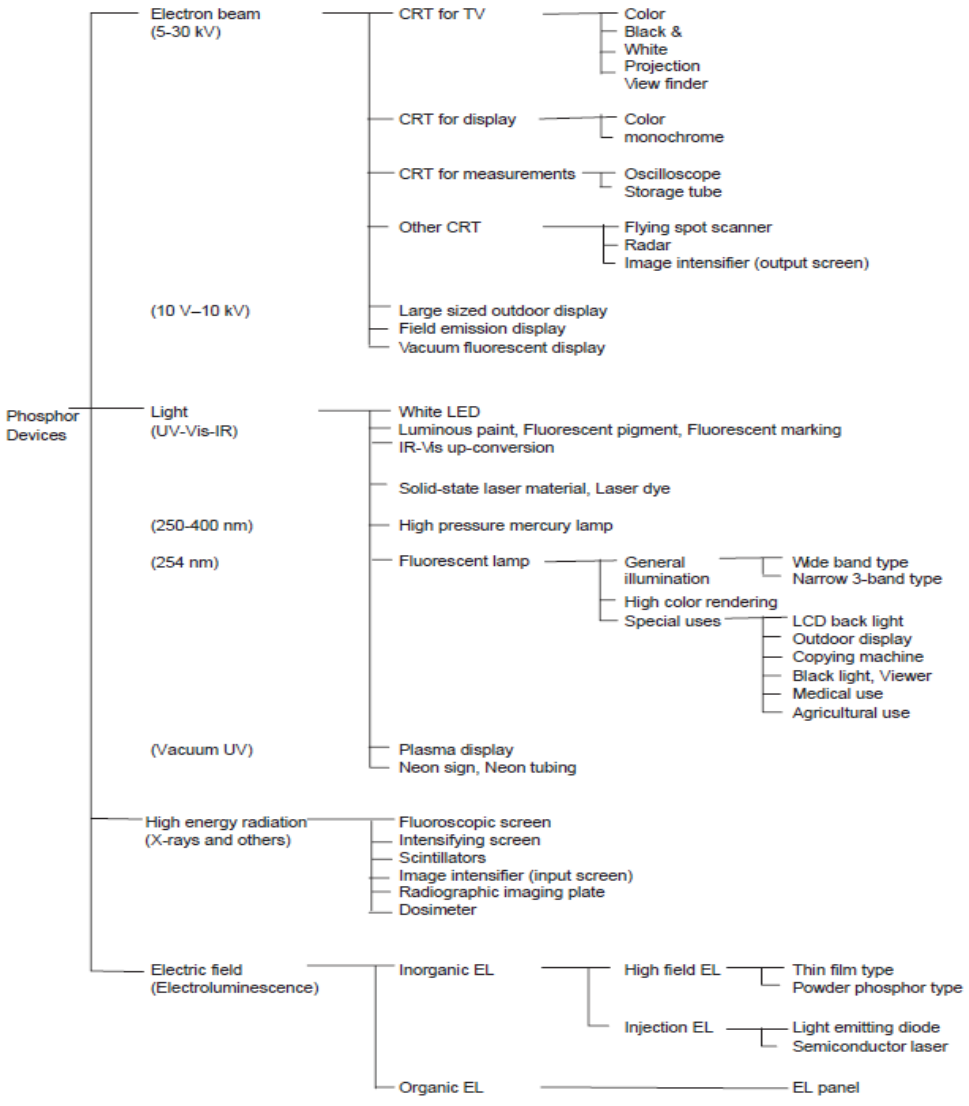

Figure 2. Application fields of phosphor devices [3]

1.2 Luminescence

Luminescence is a phenomenon in which a material emits light when subjected to an energy input. Naming of the type of the luminescence is based on the energy source that is included in the excitation process. For example, in photoluminescence (PL), cathodoluminescence, electroluminescence phosphors are excited via photons, energetic electrons, and electronic voltage, respectively. If a chemical reaction is needed to excite a phosphor, it is named as chemiluminescence.

Alexander Jablonski explained that exposure of radiant energy leads to excitation of a material to higher energy levels in his work, in 1933 [7]. In the representation of Jablonski diagram [8] (**Figure 3**) basic concepts of luminescence i.e. phosphorescence, fluorescence, internal conversion and intersystem crossing are demonstrated. It is indicated that an excited atom or a molecule returns its ground state in any case.

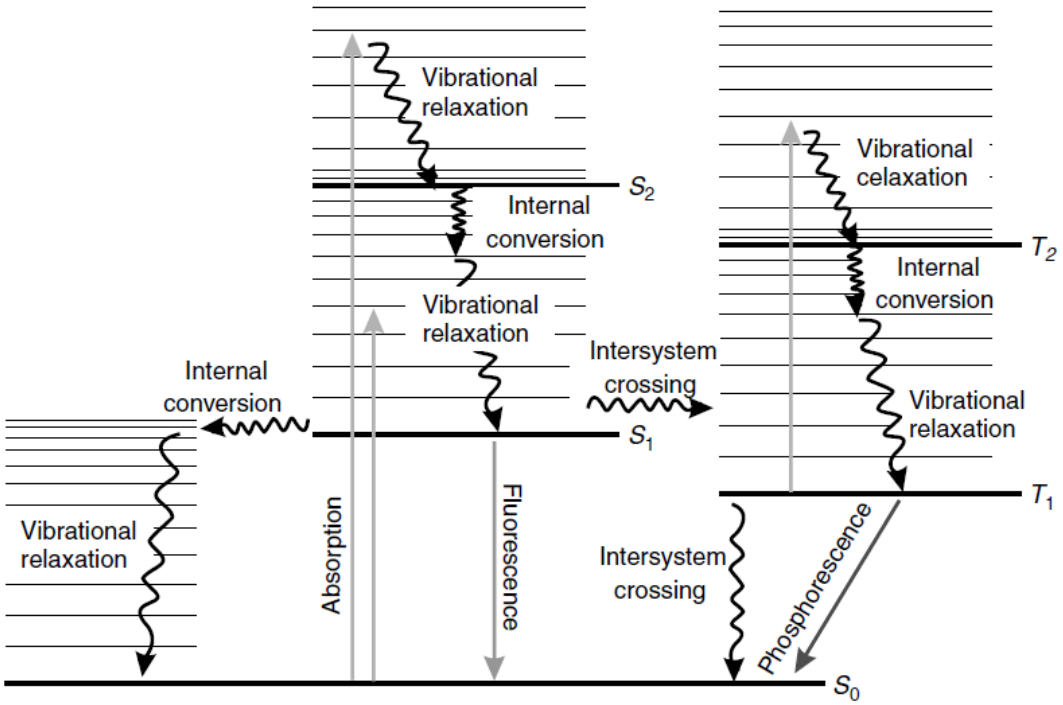

Figure 3. Jablonski diagram [8]

In particular, photoluminescence includes fluorescence and phosphorescence processes both of which arise from excitation of a molecule via photons. The main difference between fluorescence and phosphorescence is explained by emission duration of phosphors after they are excited. Generally, the emitted light is detectable until the excitation ends in the fluorescence, whereas it endures after excitation in the phosphorescence. Some molecules with comparable emission lifetimes can be differentiated by the spin state of their excited electrons. In the case of fluorescence, spin multiplicity is conserved while it changes in the phosphorescence. In other words, a material is not able to emit the absorbed energy immediately due to the change of the spin state during the phosphorescence [9]. In the luminescence phenomenon, the gap between the excitation and emission energy separates phosphors as an up conversion (UC) or a down conversion emission. In down conversion, most of the fluorescent materials obey the Stokes law which proposes that energy of the emitted photon is lower than the absorbed radiation energy with shorter wavelength [10]. Contrary to down conversion, up conversion one follows the anti-Stokes shifts in which wavelength of the emitted light is shorter than wavelength of the absorbed photons. It is important to note that luminescence mostly attributes to down conversion pathway [5] .

1.3 Rare earth elements: general characterization

Rare earth elements (REE) are composed of fifteen lanthanide (Ln) elements with atomic number varying between 57 and 71 as well as scandium (Sc, Z= 21) and yttrium (Y, Z= 39). Lanthanides are the transition metals that are included in the 4f-block and sixth period of the periodic table. Besides having a unique luminescence character, lanthanides are classified as non-toxic elements. Those elements are applicable in several modern technologies i.e. computers, TVs, plasma displays due to their emissions in UV, Vis, near-IR ranges. Moreover, their high color purity and luminescence yield, great Stokes shift, narrow band emissions, and long-lasting luminescence decay times make REE very popular for many utilization fields [11]. Characteristic electronic configuration of trivalent ions of rare earth elements (RE^{3+}) has an electron configuration of $[Xe]4f^{n}$. Electronic configurations, spin angular momentum (S), orbital angular momentum (L), and the total angular momentum of

RE^{3+} are represented in the **Table 1**. Total angular momentum is equal to J = |L – S| if the number of 4f electrons is smaller than 7, and equal to J = |L + S| if the number of 4f electrons is larger than 7. Besides, 2S+1 refer to the spin multiplicity. Electronic states are represented via term symbols with $^{2S+1}\mathbf{L_J}$ notation. L presents S, P, D, F, G, H… depending on the L= 0, 1, 2, 3, 4, 5… values, respectively. Ground state term symbols is determined according to electronic configuration that follows the Hund's rule and Pauli exclusion principle [12].

Table 1. Electronic configurations and ground state terms symbols of RE^{3+}

Atomic number	**Ions**	**Corresponding element**	***4f* electrons**	**S** ∑s	**L** ∑l	**J** ∑(l+s)
21	**Sc^{3+}**	Ar		0	0	0
39	**Y^{3+}**	Kr		0	0	0
57	La^{3+}			0	0	0
58	Ce^{3+}	Xe	↑	1/2	3	5/2
59	Pr^{3+}	Xe	↑ ↑	1	5	4
60	Nd^{3+}	Xe	↑ ↑ ↑	3/2	6	9/2
61	Pm^{3+}	Xe	↑ ↑ ↑ ↑	2	6	4
62	Sm^{3+}	Xe	↑ ↑ ↑ ↑ ↑	5/2	5	5/2
63	Eu^{3+}	Xe	↑ ↑ ↑ ↑ ↑ ↑	3	3	0
64	Gd^{3+}	Xe	↑ ↑ ↑ ↑ ↑ ↑ ↑	7/2	0	7/2
65	Tb^{3+}	Xe	↑↓ ↑ ↑ ↑ ↑ ↑ ↑	3	3	6
66	Dy^{3+}	Xe	↑↓ ↑↓ ↑ ↑ ↑ ↑ ↑	5/2	5	15/2
67	Ho^{3+}	Xe	↑↓ ↑↓ ↑↓ ↑ ↑ ↑ ↑	2	6	8
68	Er^{3+}	Xe	↑↓ ↑↓ ↑↓ ↑↓ ↑ ↑ ↑	3/2	6	15/2
69	Tm^{3+}	Xe	↑↓ ↑↓ ↑↓ ↑↓ ↑↓ ↑ ↑	1	5	6
70	Yb^{3+}	Xe	↑↓ ↑↓ ↑↓ ↑↓ ↑↓ ↑↓ ↑	1/2	3	7/2
71	Lu^{3+}	Xe	↑↓ ↑↓ ↑↓ ↑↓ ↑↓ ↑↓ ↑↓	0	0	0

Lanthanide elements owe their luminescent properties to their partially filled 4f orbitals. Due to the empty 4*f* orbitals of rare earth ions, Sc^{3+}, Y^{3+}, La^{3+}, and Lu^{3+}, are not able to present luminescence property in or near the visible range. On the contrary, partially filled 4*f* orbitals of RE^{3+} ions between Ce^{3+} and Yb^{3+} allow the utilization of those ions as a luminophore in several host matrixes, usually by replacing RE^{3+} (RE= Y, Gd, La, Lu) ions [3]. Therefore, optical spectra of rare earth elements arise from transitions between $4f^n$ (n= 1-13) configuration levels. The locations of these levels are determined by the combination of the coulomb interactions between the electrons, the spin orbit coupling, and the crystal electric field. Electrostatic interaction gives the term $^{2S+1}\mathbf{L}$ with a spacing of 10^4 cm^{-1}. The spin-orbit interaction is then split into J with splitting of 10^3 cm^{-1} and gives the $^{2S+1}\mathbf{L_J}$ term. Dieke [13] assigned the energy levels of the 4*f* orbital electrons of trivalent rare earth ions by considering that each ion has the $LaCl_3$ crystal structure. Energy level diagram given in the **Figure 4** is usually consistent with ions in nearly all host matrixes [14]. It is worth noting that the effect of the host environment on the energy levels of ions is negligible as 4*f* electrons are shielded strongly by the $5s^2$ and $5p^6$ electrons. Therefore, 4*f* electrons are not significantly affected by the electric field, which causes Stark splitting, in the surrounding.

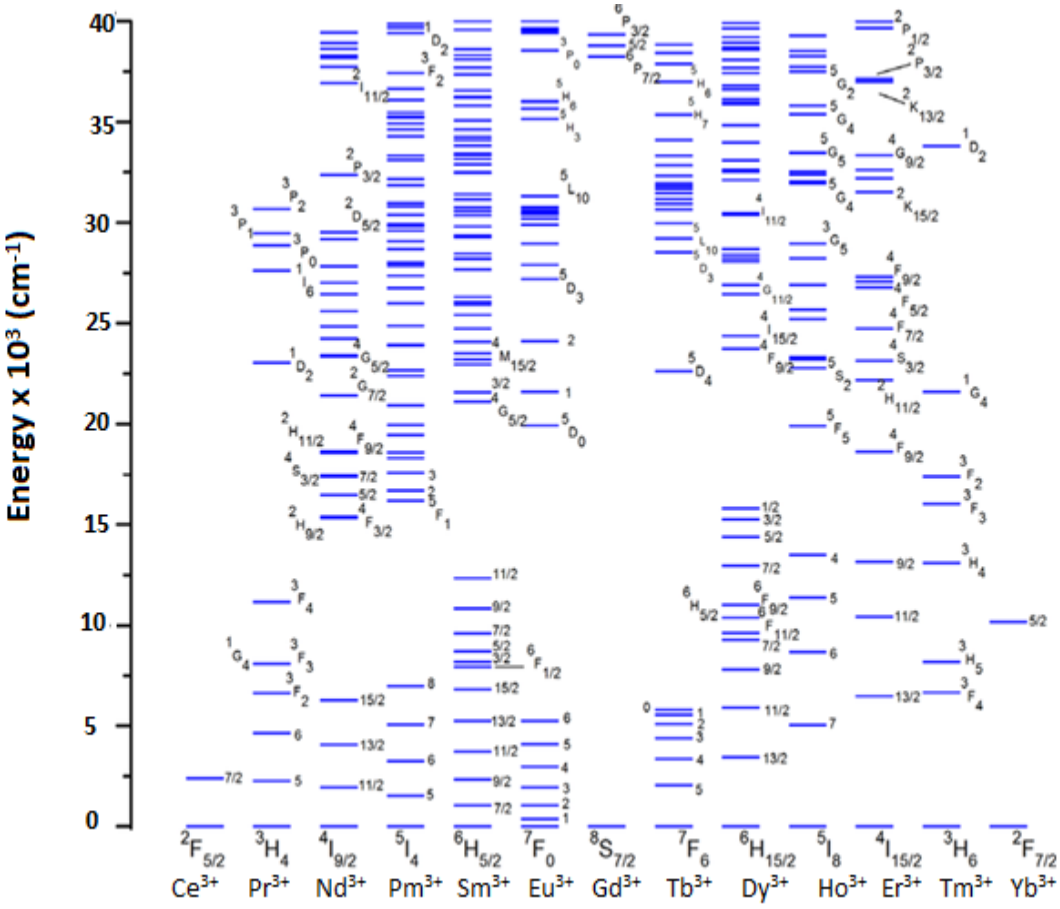

Figure 4. Energy levels of RE^{3+} ions (Reproduced with permission [14])

Apart from Ce^{3+} and Yb^{3+}, RE^{3+} ions have a great number of 4*f* energy levels. Energy levels that are associated with photoluminescence are excited via UV light and other levels are mostly omitted. Electric dipole and magnetic dipole interactions are mainly the reasons for the electronic transitions among 4*f* energy levels. According to the selection rule, electric dipole *f*-*f* transitions are not allowed due to the unchanged parity. Nevertheless, the interaction between RE^{3+} ion and host lattice or crystal field leads to change in the parity in 4*f* states and makes the transitions are available in this state [15]. Since 4*f*-4*f* transitions are forbidden, luminescence lifetimes of these transitions are generally in the range of milliseconds [3]. Besides the transitions between 4*f* levels, transitions can occur in 4*f*-5d states and charge-transfer states (CTS). Electrons are transferred from 4*f* orbitals to 5*d* orbitals in the 4*f*-5*d* states, while electrons of neighboring anions are transferred to the 4*f* orbitals in the CTS.

Both of this transfer processes which lead to powerful optical absorptions are permitted. Moreover, surroundings affect the energy of these states more than the energies of 4*f* levels. Optical absorptions that arise from *f-d* transitions are common in Ce^{3+}, Eu^{2+}, Sm^{2+} ions [3].

1.3.1 Photoluminescence properties of Dysprosium ions (Dy^{3+})

Amongst trivalent ions of rare earth elements, Dy^{3+} is very popular as it is crucial for devices requiring white light [16]. Emission spectrum of Dy^{3+} includes both strong blue (B) $^4F_{9/2}\rightarrow{}^6H_{15/2}$ band transition and yellow (Y) $^4F_{9/2}\rightarrow{}^6H_{13/2}$ band transition. The $^4F_{9/2}\rightarrow{}^6H_{15/2}$ transition which result from magnetic dipole transitions is not affected by the environment, whereas $^4F_{9/2}\rightarrow{}^6H_{13/2}$ transition that occurs as a result of electric dipole transitions is sensitive to the nature of the surroundings because they are not parity allowed. The latter transition is allowed when Dy^{3+} ions pertain to the low symmetry site [17]. There are various studies about Dy^{3+} doped phosphors in literature [18, 19].

In a study by N. Wazir et al., the emission bands of Dy^{3+} doped lithium calcium borate are reported as 490, 578, 674 nm with 349 nm excitation wavelength **(Figure 5)**. In their study, yellow emission of Dy^{3+} is higher than the blue one. Thus, they reported that Dy^{3+} ions may prefer the low symmetry site because of the similar radius size of Dy^{3+} and the Ca^{2+} ions in the host material. Additionally, intensity ratio of Y/B is used for the determination of the host environment of RE ions. The increase or decrease of the Y/B intensity ratio indicates the changes in surroundings. For instance, increase of the Y/B ratio with the increasing concentration of Dy^{3+} accounts for the alteration in the crystal field around the Dy^{3+} ions [20].

In general, Y/B ratio increases with the increasing difference in the radius of the Dy^{3+} ion and its circumjacent elements. If radius of Dy^{3+} ions and surrounding elements are equivalent, Y/B ratio does not vary with the change in the Dy^{3+} concentration. However, if they are inequivalent, concentration variation of Dy^{3+} could affect the crystal structure and Y/B ratio could vary with the Dy^{3+} ion concentration [4].According to study of N. Wazir et al**.,** the possible transitions of the Dy^{3+} ions in lithium calcium borate host upon 349 nm excitation is reported as $^4F_{9/2}\rightarrow{}^6H_{15/2}$ (490 nm), $^4F_{9/2}\rightarrow{}^6H_{13/2}$ (578 nm), and $^4F_{9/2}\rightarrow{}^6H_{11/2}$ (674 nm) which correspond to the blue, yellow, and red emissions, respectively [20].

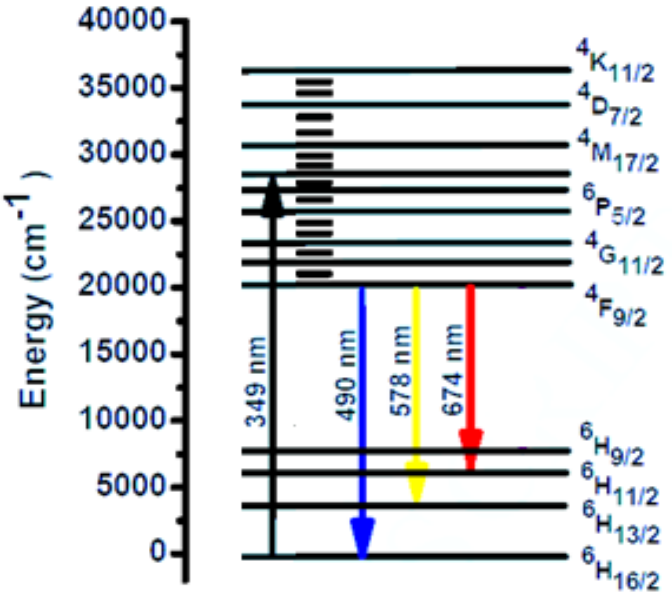

Figure 5. Energy level diagram of of Dy^{3+} ions. (Reproduced with permission [20])

1.3.2 Photoluminescence properties of Terbium ions (Tb^{3+})

Terbium is one of the most applied ion among the rare earth elements because of its efficient optical properties. Tb^{3+} activated phosphors are utilized in optical technologies such as plasma display panels [21], fluorescent lamps, mercury free lamps [22], UV radiation sensors [23]. Emission bands of Tb^{3+} in the visible range from transitions; $^5D_4 \rightarrow {}^7F_J$ (J= 0-6), attributed to green (G), and $^5D_3 \rightarrow {}^7F_J$ correspond to blue (B) region. Intensity of emission lines of $^5D_3$ state becomes lower by increasing terbium ion concentration because of the cross relaxation. Besides, B/G intensity ratio depends on both Tb^{3+} concentration and the host materials [3].

J. Zmojda et al. studied emission bands of Tb^{3+} doped phosphate glasses. They reported that $^5D_4 \rightarrow {}^7F_5$ transition associated with the peak at 543 nm has the maximum luminescence intensity [23].

In general, the emission peak is the strongest in mostly all host matrixes as it is originated from both electric dipole and magnetic dipole transitions [3]. According to proposed diagram in the study of J. Zmojda et al., main transitions of Tb^{3+} are $^5D_4 \rightarrow {}^7F_6$, $^5D_4 \rightarrow {}^7F_5$, $^5D_4 \rightarrow {}^7F_4$, and $^5D_4 \rightarrow {}^7F_3$ which correspond to 489, 544, 586 and 622 nm, respectively (**Figure 6)** [23].

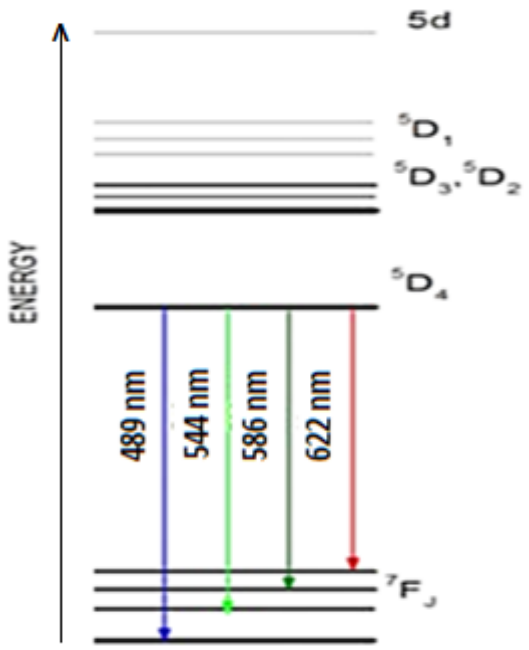

Figure 6. Energy level diagram of Tb^{3+} ions [23].

1.3.3 Photoluminescence properties of Europium ions (Eu^{3+})

Luminescence properties of Eu^{3+} activated phosphors with different host materials have been examined for their deep red emissions. Eu^{3+} activated materials have a wide range of practical applications such as light emitting diodes [24], flat panels e.g. plasma display panels [25].

In a study by G. Jia et al., Eu^{3+} doped phosphors possess mainly emissions which result from $^5D_0 \rightarrow {}^7F_J$ (J= 0-4) transitions which are located about 578, 590, 614, 652, and 701, respectively [26]. It was reported that the emission band around 590-600 nm which occurs because of the magnetic dipole transition $^5D_0 \rightarrow {}^7F_1$ is insensitive to the changes in the surroundings of activator ion. However, the emission of electric dipole $^5D_0 \rightarrow {}^7F_2$ transition in the vicinity of 610-630 nm is hypersensitive to the changes in the environment around the Eu^{3+} ion [26].

S. K. Sharma *et al.* investigated the emission spectrum of Eu^{3+} ions upon exciting at different wavelengths (390, 465, 530 nm) and reported that although intensity of the emitted lines varied with the changes in excitation wavelength, band positions were conserved [27]. As it is represented in **Figure 7**, those emission lines that are mentioned above are observed in different excitation wavelengths.

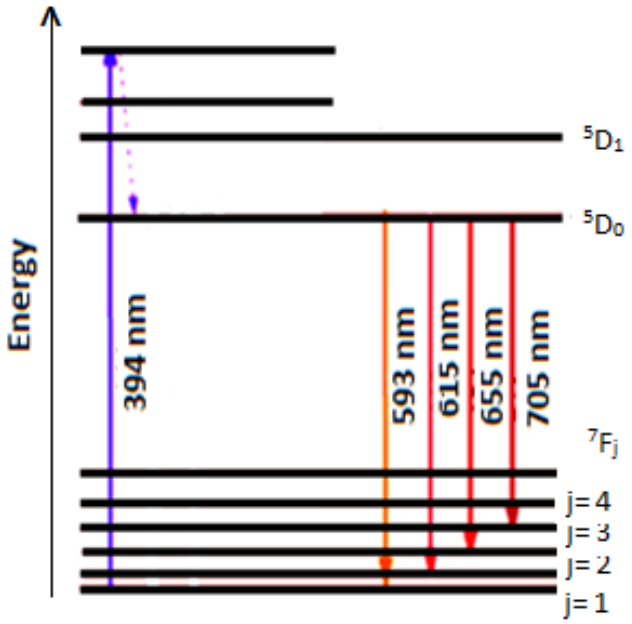

Figure 7. Energy level diagram of Eu^{3+} ions [27].

1.3.4 Photoluminescence properties of Cerium ions (Ce^{3+})

Among the rare earth ions, Ce^{3+} ions have the lowest $4f \rightarrow 5d$ transition energy. However, energy gap between $5d^1$ state and the closest $^2F_{7/2}$ state is large enough for efficient light emission. The host matrixes affect the excited energy levels of Ce^{3+} ions by the way of crystal field splitting of 5*d* orbitals, as given in **Figure 8**. Thus, energy of the emitted photon is directly linked to structure of the host material [3].

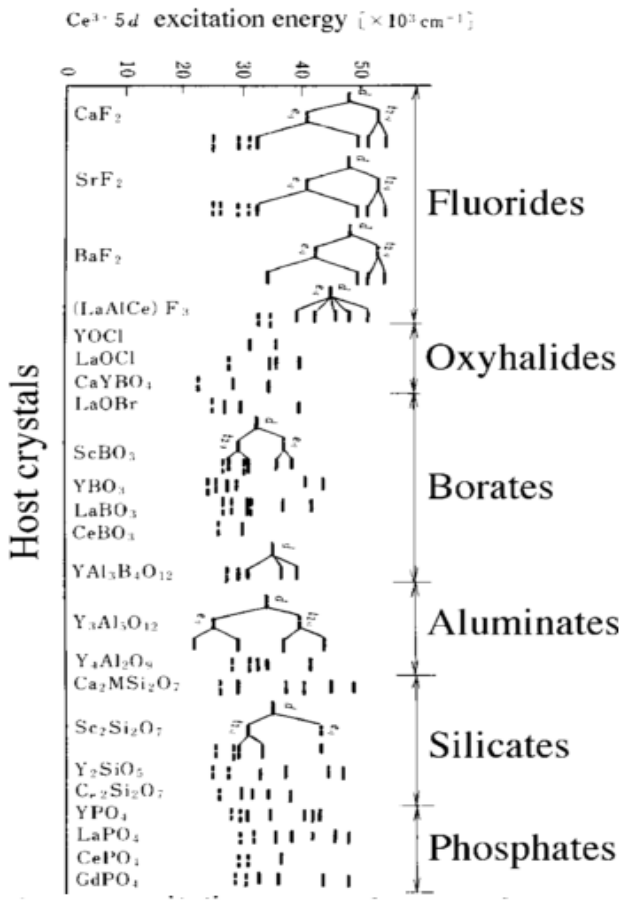

Figure 8. Excited 5*d* energy levels of Ce^{3+} in several host matrixes [3]**.**

C.H. Yang *et al.* investigated the emission spectra of Ce^{3+} doped phosphors upon 328 nm excitation. A broad band is centered in the vicinity of 400 nm is due to the transition of $5d \rightarrow {}^2F_J$ (J= 5/2, 7/2) **(Figure 9)** [28].

The decay life of Cerium ion emissions which is in the range of 100 ns and 10 ns is the shortest among the lanthanide ions. Parity and spin allowed transitions from $5d^1$ state to $4f^1$ state result in short emission lifetimes. Owing to short luminescence decay time, Ce doped materials are utilized for the flying spot scanners and beam index cathode- ray tubes [3]. Furthermore, Ce^{3+} ions are excellent sensitizers for some ions such as Tb^{3+}, Dy^{3+}, Eu^{2+}, and Mn^{2+} in various kinds of host crystals [4].

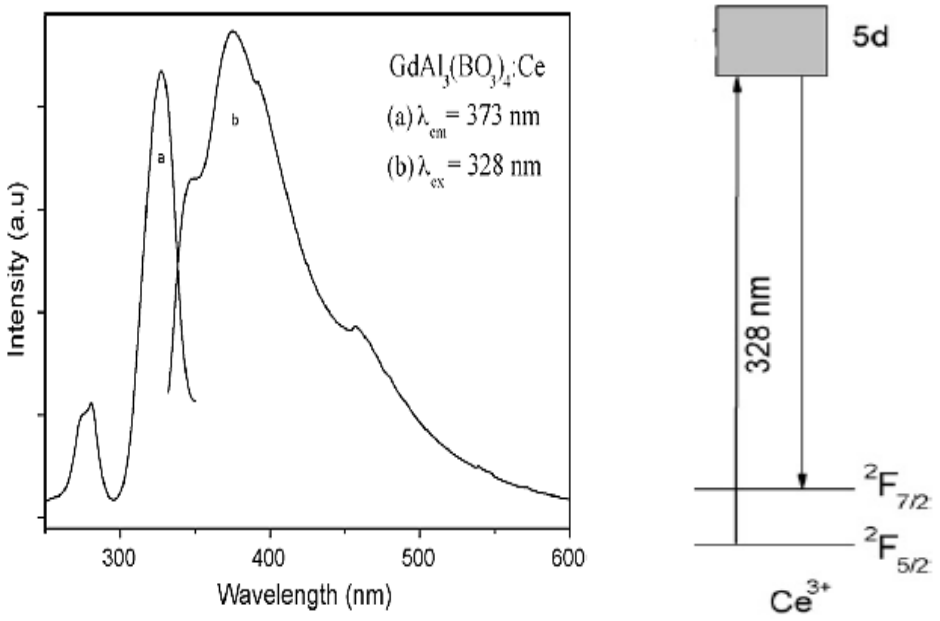

Figure 9. Excitation and Emission spectra of Ce^{3+} ions (Reproduced with permission [28])

1.3.5 Energy transfer mechanisms

The process of migration of excitation energy of an ion to another one is named as energy transfer which is a common process for phosphors with luminescent centers (e.g. REE ions, transition metal ions etc.). Phosphors are activated by the different or identical luminescent centers. Concentration quenching which is reducing the desired emission intensity takes place when the energy transfer occurs through same kind of luminescent centers. It can be expected that activator luminescence intensity is on the rise with the increasing concentration of luminescent centers. However, this trend is valid until the critical concentration is reached since above this concentration excited ions begin to lose energy non-radiatively to adjacent ions which are in their ground states [15]. On the other hand, energy transfer can lead to an increase in emission intensities of luminescent centers when they are not identical. This phenomenon is called as sensitized luminescence which includes the activator and the sensitizer ions. In co-doped phosphors, not only emissions of the activator but also the sensitizer ions may be observed. Therefore, double or triple doped phosphors provide light emissions in various colors concurrently with the single excitation wavelength. Owing to these properties, multiple doped phosphors are desirable for designing white light production [5].

Color tunable white light emitting materials which can be obtained by combining three different phases based on red, green and blue light emitted phosphors have some disadvantages such as low luminescence efficiency, the strong reabsorption of the blue light by the red and green phosphors [4, 29]. On the other hand, these problems can be eliminated by designing single phase white light emitting phosphors with multiple doping.

Energy transfer mechanisms were first studied by Förster [30] who paid attention only between two allowed electric dipole transitions which are common in organic systems. Besides, another fundamental explanation for forbidden transition of activator and allowed transition of sensitizer in inorganic solids was revealed by Dexter [31] who considered high order transitions such as dipole-quadrupole, quadrupole-quadrupole interactions. According to both Föster and Dexter, energy transfer probability decreases with the increasing distance of activator-sensitizer, and it becomes negligible about 10-20 A°. Therefore, the energy levels of activator and sensitizer ions should be as close as possible for efficient energy transfer.

Possible energy transitions from Ce^{3+} to Dy^{3+} ions, Dy^{3+} to Eu^{3+}, and Ce^{3+} to Tb^{3+} are represented in **Figure 10(a-c),** respectively. In all transition mechanisms, excitation of sensitizer ions leads to strong emission bands of activator ions at their specific wavelengths. There are consistent studies in literature **[**28**,** 32,33].

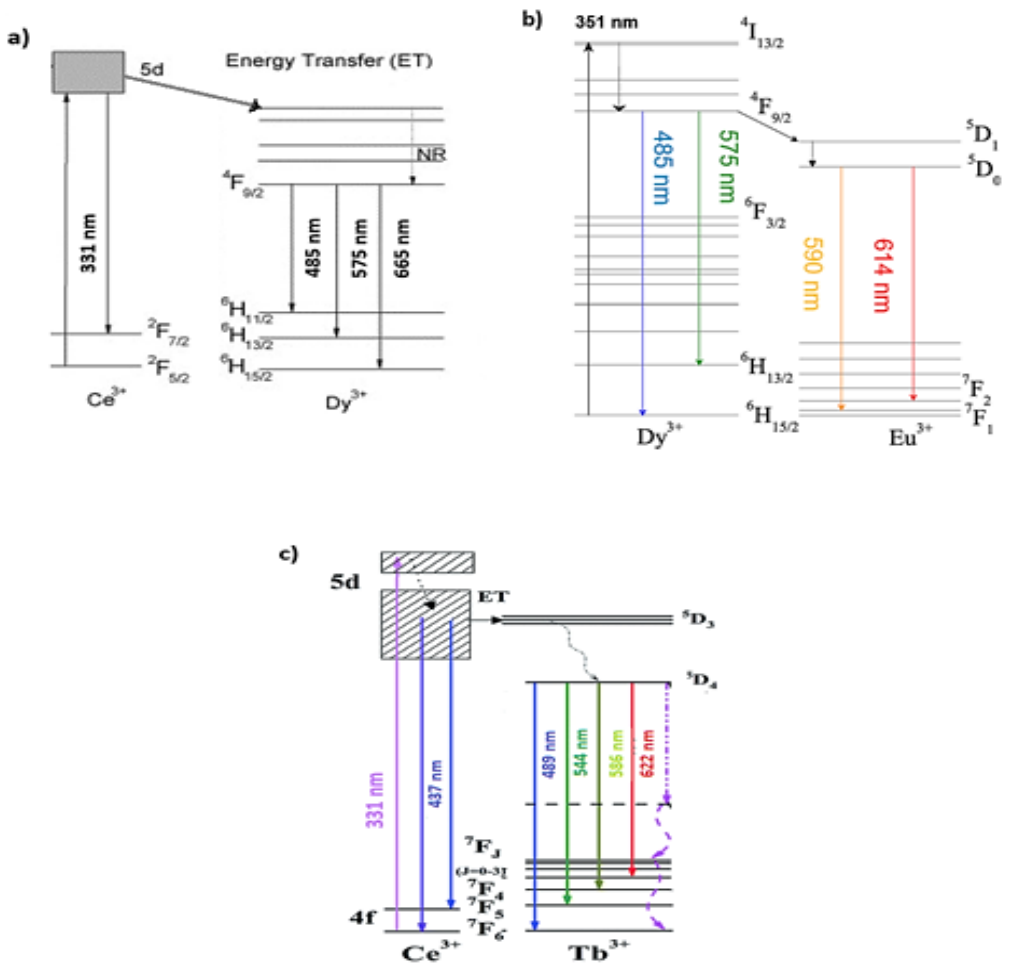

Figure 10. Energy level diagram of the possible energy transition mechanisms **a)** from Ce^{3+} to Dy^{3+} ion (Reproduced with permission [28]), **b)** Dy^{3+} to Eu^{3+} ion [32], and **c)** from Ce^{3+} to Tb^{3+}ion [33]

1.4 Photoluminescence decay lifetimes

Photoluminescence decay time studies are subpart of the luminescence measurements. Lifetimes of samples are recorded by exciting them with radiation which has short pulse ranges (i.e. from fs to ns depending on the material). Basically, duration of the emission is measured after the excitation. Each emission line may have different decay rates that are affected by its environment [34]. Generally, obtained decay curves of phosphors may fit to single exponential decay equation **(1.4.1)** which includes initial intensity (I_0) at t = 0, luminescence intensity at t time (I_t) and the decay life time (τ). On the other hand, some of the decay curves may be required to fit by double exponential decay equation **(1.4.2)**. The terms τ_1 and τ_2 are fast and slow components of lifetimes which are associated with the

intensity constants I_1 and I_2, respectively. Moreover, the average decay lifetimes can be calculated with the formula given in **1.4.3**. [35, 36].

$$I_{(t)} = I_0 e^{-t/\tau} \qquad (1.4.1)$$

$$I_{(t)} = I_1 e^{-t/\tau_1} + I_2 e^{-t/\tau_2} \qquad (1.4.2)$$

$$\tau = \frac{I_1\tau_1^2 + I_2\tau_2^2}{I_1\tau_1 + I_2\tau_2} \qquad (1.4.3)$$

Multi-exponential fits with the decay curves of phosphors can give information about energy transfer and quenching mechanisms. In general, single exponential functions are mostly used for the radiative transition of two levels. If the emission lines are produced by the activator ions, measured lifetimes would base on the coordination geometry of these ions. In other words, different lifetimes can be obtained with varied geometries of the ions. Therefore, the number of coordination sites of the activators may be revealed by the quantity of the exponential fit [34].

1.5 Chromaticity coordinates

The observed color by human eye can be defined in a chromaticity diagram. In order to predict how the color of light is detected by human eye, CIE color chromaticity coordinates were accepted in 1931. CIE abbreviation comes from the French name 'Commission International de I'Eclairage'. There are three primary light colors for which cone cells in the retina are sensitive. Red, green, and blue color matching functions (**Figure 11, right**) denoted as $\bar{x}(\lambda)$, $\bar{y}(\lambda)$, and $\bar{z}(\lambda)$, respectively, were designed based on the sensitivity of each cone cells which are responsible for color vision of human. X, Y, and Z values named as tristimulus values are calculated with the equations given in 1.5.1 to 1.5.3 in which spectral energy distribution is denoted by $P(\lambda)$. Those tristimulus values are used for the calculation of the chromaticity coordinates (x, y) (Eq. 1.5.4-1.5.5). Therefore, one can predict the color of perceived light by human eye from the point of the calculated coordinates (x, y) on a CIE diagram (**Figure 11, left**).

$$X = \int_{380}^{780} \mathrm{P}(\lambda)\bar{x}(\lambda)\mathrm{d}\lambda \quad (1.5.1)$$

$$Y = \int_{380}^{780} \mathrm{P}(\lambda)\bar{y}(\lambda)\mathrm{d}\lambda \quad (1.5.2)$$

$$Z = \int_{380}^{780} \mathrm{P}(\lambda)\bar{z}(\lambda)\mathrm{d}\lambda \quad (1.5.3)$$

$$x = \frac{X}{X+Y+Z} \quad (1.5.4)$$

$$y = \frac{Y}{X+Y+Z} \quad (1.5.5)$$

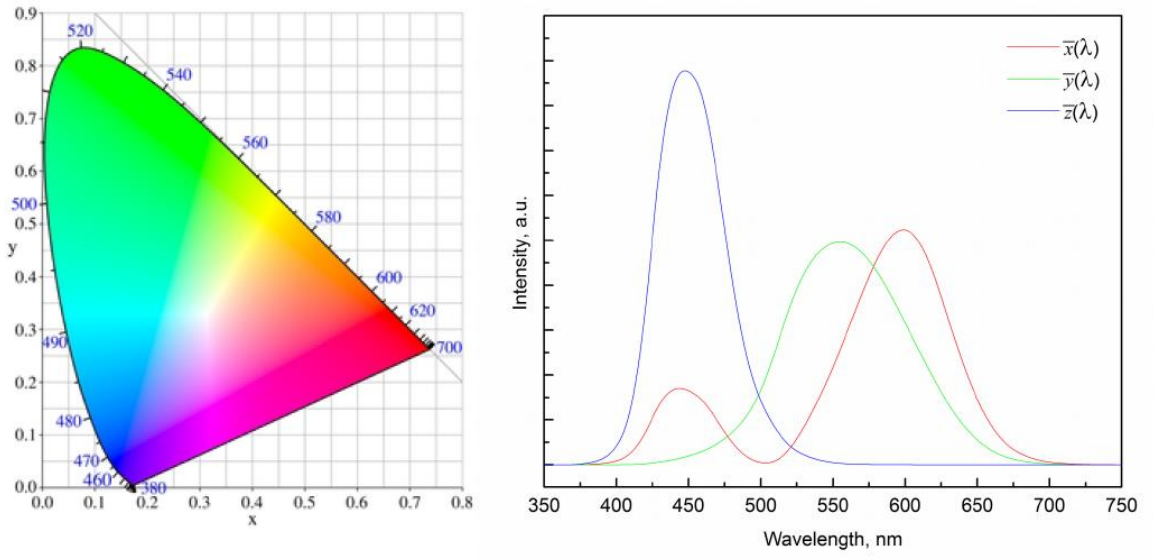

Figure 11. CIE chromaticity diagram (left) and color matching functions (right) [34]

1.6 Host materials

Host materials should have thermal and chemical resistance to endure at high temperatures and to provide durable luminescence. As long as there is no energy transfer between the host and the dopant, transparent host matrixes are preferred for the emission processes [4]. Crystalline and the amorphous (glass) forms of matrixes can be utilized in applications. There are various types of host matrixes which are studied for production of lanthanide based luminescent materials. Phosphates [32], tungstates [37], silicates [38], and borates are the most common host materials that are involved in phosphor synthesis. Phosphates have easy applicability in technology and high thermal stability. Owing to these advantages they are preferred in many studies in literature such as $Sr_3Y(PO_4)_3$: Dy^{3+}, Eu^{3+} [39], $KMgLa(PO_4)$: Dy^{3+} [40] $Sr_3GdNa(PO_4)_3F$: Dy^{3+} [41].

Charge transfer mechanism between oxygen and the metal ion in tungstate based phosphors provide large and dense absorption bands in near ultraviolet region. Thus, they can be applicable for white light production [42]. In this study, borate host materials were included due to their high abundance in our country and advantages that will be discussed in detail in the next section.

1.6.1 Borates

Boron which is called as semi-metallic element is the first element of group 3A in the periodic table with the atomic number 5. Amongst its isotopes, most stable ones are found in nature with the atomic mass 10 and 11. Boron 10 isotope is preferred in nuclear power plants as it has high neutron capture capability. Boron acts as a nonmetal in its compounds while it conducts electricity like carbon in its elemental form. Because of its high reactivity boron cannot be found in nature as a free element [43]. Most abundant forms of borate minerals are Tincal ($Na_4B_4O_2$. $10H_2O$), kernite ($Na_2B_4O_7$. $4H_2O$), colemanite ($Ca_2B_6O_{11}$. $5H_2O$) and ulexite ($NaCaB_5O_9$. $8H_2O$) [44]. The total reserve of the world boron minerals is reported as 1.304.000 thousand tons in 2016. **Table 2** summarizes the percentages of boron reserves of countries. Turkey is leading in the world by having the 72.8 percent of total deposit of world boron minerals based on boron oxide. [44]. Minerals that contain boron are named as borates. Moreover, borates have several application fields in the

industry such as glass and porcelain manufacture, production of leather, carpets, cosmetics, and photographic chemicals, fertilizers, wire drawing, and welding and brazing of metals [45].

Table 2. Distribution of boron reserves**.**

Countries	**Total Reserves (Thousand tons B_2O_3)**	**Distribution (%)**
Turkey	950.000	72.9
U.S.A	80.000	6.1
Russia	100.000	7.7
China	47.000	3.6
Argentina	9.000	0.7
Bolivia	19.000	1.5
Chile	41.000	3.1
Peru	22.000	1.7
Kazakhstan	15.000	1.2
Serbia	21.000	1.6
Total	1.312.300.100	

Rare earth orthoborates, e.g. $LnBO_3$ (Ln: La, Gd, Y) have become promising inorganic photoluminescence materials because of their good transparency in the ultraviolet (UV) and visible range, excellent thermal stability, high luminous efficiency, strong absorption in vacuum ultraviolet (VUV) to UV region [28, 46]. Generally, borate compounds are synthesized at lower temperature and duration of heating than phosphate and tungstate compounds [37]. With their transparency in the UV-Vis range, rare earth orthoborates can be applied in Hg-free lamps and plasma display panels [47]. Light emitting diodes [48], non-linear optics [49] and lasers are the various applications of phosphors of borates. Lanthanide orthoborates ($LnBO_3$) were studied by Levin et al. in 1961. The study reported that depending on the type of the rare earth ion, $LnBO_3$ crystallize in the three different forms of calcium carbonate ($CaCO_3$) which are vaterite, aragonite and calcite [50].

For instance, while the larger lighter rare earth elements (La-Nd) possess aragonite type structure, smaller heavier ones (Sm-Lu) have vaterite type structure [51]. Nevertheless, currently five crystal structures that are based on the calcium carbonate crystals forms are known: the hexagonal vaterite type with P63/m space group, the orthorhombic aragonite type with Pnma space group, the rhombohedral vaterite type with R32 space group, and rhombohedral calcite type with R3c space group, and monoclinic pseuowollastonite type with C2/c space group [52].

1.6.2 Crystal structure and IR studies of $LaBO_3$

Lanthanum orthoborate compounds present aragonite form of $CaCO_3$ with Pnma space group, orthorhombic crystal structure and unit cell parameters: a= 5.87 Å, b=5.10 Å, c= 8.25 Å (JCPDS no: 12-0762) as it represented in **Figure 12**. Volume of the structure equals to 247.570 $Å^3$ and Z= 4 for per unit cell.

Emprical Formula	$LaBO_3$
Molar mass	197.7 g/mol
Crystal System	Orthorhombic
Space Group	*Pnma*
Powder diffractometer	Panalytical X'Pert Pro
Radiation	CuKα(λ=1.54051Å)
Unit-cell dimensions	a=5.8761(1) Å
	b=5.10535(9) Å
	c=8.252(1) Å
Volume	247.570 (8) $Å^3$
Step (°)	0.013
2 Theta Range	10-150 °
R_{wp}	0.1076
R_p	0.0844
χ^2	5.101

Figure 12. Crystal structure refinement and data of Lanthanum orthoborates [53].

The crystal structure of $LaBO_3$ was shown in the **Figure 13**. Lanthanum orthoborate structure includes trigonal planar borate units $(BO_3)^{3-}$ which are located on c axis. IR spectroscopy, which provides information about the stretching and bending vibrational modes of structures, is the most reliable way to detect planar anionic borate units.

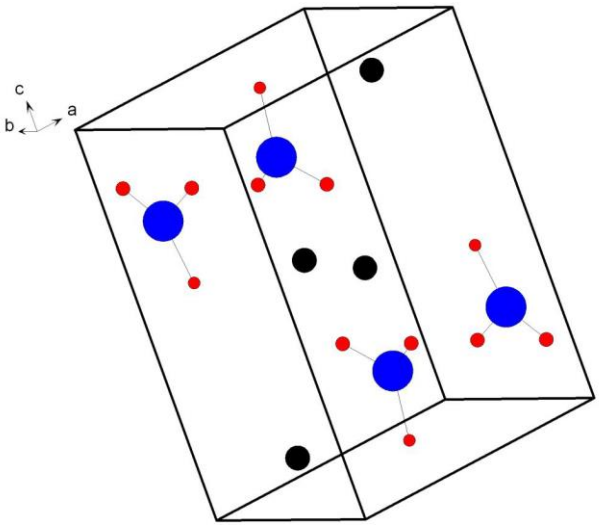

Figure 13. Crystal structure of $LaBO_3$ [53].

Vibrational modes of $LaBO_3$ are reported as ν4 (in-plane bending) at 670 cm^{-1}, ν3 (asymmetric stretching) between the range of 1100 and 1400 cm^{-1}, ν2 (out of plane bending) in the range of 700 to 800 cm^{-1}, ν1 (symmetric stretching) centered around 940 cm^{-1} . It has been reported that observed vibrational modes between the range of 1350 and 1150 cm^{-1} are associated with the stretching frequencies of a coordinated BO_3^{3-} unit [54].

1.7 Synthesis methods

There are various kinds of synthesis methods which have involved in the production of inorganic phosphors. Solid state synthesis [55], combustion synthesis [28], sol-gel synthesis [46], hydrothermal synthesis [56], microwave assisted synthesis [57] are some of those methods which are utilized in the synthesis of rare earth orthoborates. Each method has its own advantages and disadvantages.

In a solid state synthesis, the reactants are allowed in the chemical reaction without the presence of a solvent. Removal of the solvent from the reaction in a solid state reaction means that more products can be produced in a cost effective way for

industrial applications. Rare earth complexes and alkali earth compounds are utilized in oxides and carbonates forms, respectively. This method does not have any complicated process. Basically, all reactants are mixed in stoichiometric amounts and then grounded. After grounding process, mixture is calcined at higher temperatures for a couple of hours. Although this method finds itself a large extend of utilization field, it has some disadvantages. Using higher heating temperatures is energy consuming process and may lead to loss of compounds that are desired to synthesize [34]. Moreover, ideal processing should result in homogeneous and uniform material, but some solid state reactions could not do that. The preparation of a single-phase compound is sometimes difficult by the conventional solid state method.

Preparation of phosphors with sol gel method is accepted as a wet method. This method is a chemical technique which include hydrolysis, gelling, drying and heating processes. As a starting step, a sol which contains solvent, RE ions sources, linking agents, chelating agents, and anions is prepared. Linking agents such as polycondensable compounds are utilized to formation of polymer network which can also be named as gel [58]. Chelating agents prevent precipitation by forming complexes with metal ions [59]. After gelation process is completed, a xerogel is produced via drying of obtained gel [60]. The xerogel process enable formation of inorganic nanoparticles [34]. This method has some advantages over other conventional heating methods. For example, doped ions tend to diffuse more homogenously which can prevent concentration quenching. Moreover, temperature may be low in the sol-gel process. Thus, this process allows the doping of organic and biological molecules into porous inorganic materials. Nevertheless, in this process it is very difficult to remove residual hydroxyls completely from the sol-gel material. In order to remove this organic group, the samples are calcined above 1000 ° C which may produce undesirable side effects.

Since the late 1980s, the combustion synthesis reaction has been discovered as an alternative to the sol gel process. It is the longer lasting solid state process for the production of homogeneous, crystalline, and fine grain size phosphors. This method provides a fast, exothermic, and self-sustaining reaction that takes place using the appropriate oxidants (metal nitrates, ammonium nitrate, etc.) and organic fuels (urea, carbohydrazine or glycerin). High amount of heat is released during the formation of

the products in the burning process. The advantage of the combustion synthesis reaction for oxide-based phosphorus is that it enables production of fine-sized phosphors which can be well crystallized in a short period of time. Distinctive character of this method comes from the fast removal of organic compounds and solvent simultaneously. Nano size materials are obtained in the combustion method [61].

Hydrothermal synthesis can be described as a method of synthesis of single crystals which is affected from the solubility of minerals in hot water under high pressure. The aqua solution of reactants (i.e. salts, bases, acids) is exposed to higher temperature and pressure for several hours in this method. The crystal growth is carried out in a steel cylindrical container called autoclave. In general, it is possible to control phase, morphology, and size of obtained products by changing reaction conditions (e.g. temperature, time) or using different reactants in the hydrothermal method. Diameter of the products is around micrometers (1-10) and thickness of them is around ten nanometers [34]. It is possible to obtain products with high purity and homogeneity via hydrothermal synthesis without additional calcination process [62].

Microwave assisted synthesis has become very popular for many research fields due to its strengths over classical heating methods [63]. Microwave assisted synthesis is superior to conventional heating in the aspects of energy and time saving processes. In conventional way, reactants are heated up with external heat supply which first crosses from the container wall and reaches to the reactants. Thus, this energy transfer from the suppliers to the reactants is inefficient and slow. However, energy is absorbed directly and homogenously by reactants in the microwave sintering pathway which leads to increase in temperature immediately [64]. Strengths of the microwave method over conventional ways in the aspects of its potentials can be summarized as follows: i) energy saving and shorter production time, ii) better product homogeneity and yield, iii) chance of synthesis improvable microstructures, and iv) synthesis of novel materials.

Microwave heating may occur in the presence of charged particles which are able to move freely into solids or liquids under the exposure of electric field, oscillating electric current is produced. Energy is transferred to the surroundings as heat due to the resistance to movement of these particles. This pathway is named as conducting

heating. In the absence of those moving particles but the presence of polar molecules, which have dipole moments, electric field begins to align those dipole moments. This is the dielectric heating way that is usually used for cooking in our daily life [65]. Dielectric heating directly related with the interaction of polar units and the alternating electric field. Thus, at least one polar reactant must be involved for absorption of microwave in this pathway. As an disadvantage, finding of appropriate reagent or fuel via trial and error method may be time consuming process [66].

1.8 Aim of the study

In previous studies of our group, optical properties of Dy^{3+} and Tb^{3+} single doped $LnBO_3$ (Ln: Ga, Y, La) were investigated. Although $LaBO_3$ host structure is the best for all dopants, optical properties of samples need to be enhanced. Aim of the study is to enhance the luminescence properties and to tune the color of the borate based phosphors by codoping. In accordance with this purpose, a rare earth orthoborate compound, lanthanum orthoborate $LaBO_3$ was used as a host material. $LaBO_3$ host material was codoped with different combinations of RE^{3+} ions (Ce^{3+}, Dy^{3+}, Tb^{3+}, Eu^{3+}, Bi^{3+}). Several characterizations were carried out to explain luminescence properties, colors, luminescence lifetimes, crystal structure, and morphology of samples. In addition, possible energy transfer mechanisms were discussed in the codoped samples to understand higher luminescence intensities. As far as we know, there is no study on codoped combinations of $LaBO_3$ by which is synthesized microwave assisted solid state synthesis. Thus, our study is unique and reproducible.

CHAPTER 2

MATERIALS AND METHOD

2.1 Materials

Table 3 includes the materials that were used for production of phosphors in the present study.

Table 3. Used materials, their intended purpose and labels

Material with molecular weight	Intended Purpose	Labels
La_2O_3 (1) (325.82 g/mol)	Production of $LaBO_3$	Aldrich 99.9%
La_2O_3 (2) (325.82 g/mol)	Production of $LaBO_3$	abcr-99.9%
H_3BO_3 (61.83 g/mol)	Borate source	Merck
$CO(NH_2)_2$ (Urea) (60.06 g/mol)	Fuel	Merck
Dy_2O_3 (373.0 g/mol), Eu_2O_3 (351.926g/mol), $Ce_2(CO_3)_3{\cdot}xH_2O$ (460.3 g/mol), Bi_2O_3 (465.96 g/mol)	Dopant agents	Aldrich 99.9%
Tb_4O_7 (MW: 747.69 g/mol)	Dopant agents	Alfa Aesar-99.9%

2.2 Instrumentation

2.2.1 Furnace

Protherm furnace PLF-130-6 with the capability of heating up to 1300° was utilized for the annealing processes of materials.

2.2.2 Powder X-ray diffraction (XRD)

X-ray diffraction is the most reliable method for defining crystal structures of materials. Crystal structures of synthesized borate phosphors were investigated by the powder XRD measurements. Rigaku Miniflex X-Ray Diffractometer instrument with CuKα (30 kV, 15mA, λ= 1.54051 Å) source was used. The range of 2θ degree was set between 5° and 80° degrees. Scanning speed was 1° per minute (1°/ min). Resolution of scanning was set to 0.01. Diffraction pattern of lanthanum orthoborate was obtained from International Centre for Diffraction Database (ICDD) with card number 12-0762.

2.2.3 Attenuated total reflectance- fourier transform infrared spectrometer (ATR- FTIR)

ATR-FTIR spectra of prepared phosphors were recorded with Bruker IFS 66/S spectrometer collected with ZnSe crystal at an incident angle of 45°. The spectra were obtained between 4000-550 cm^{-1} with 4 cm^{-1} resolution.

2.2.4 Far-IR spectrometer

Far-IR spectra of samples in range of 640 to 70 cm^{-1} were collected by Nicolet 6700 FTIR from sample pellets under dry air conditions. For pellet production, mixtures which are containing 10 mg of powder sample and 100 mg of high density polyethylene (HDPE) were prepared. Then, 5 tons of pressure was applied to the mixture for 5 minutes. Before the data collection from obtained pellet samples, they were purged with dry air for 4 hours in the instrument to reduce water attenuation at low frequencies. Resolution was set as 4 cm^{-1}.

2.2.5 Luminescence spectrometer

Photoluminescence properties of samples were investigated by Varian Cary Eclipse Fluorescence Spectrometer. Measurements were carried on powder form of samples with solid sample holder equipment of the instrument. Sample holder position was set for optimum signal collection. Emission spectra were collected in the range of 430 to 700 nm with 100 nm per minute scanning speed. Both excitation and emission slits were arranged to 5 nm. In addition, 240-395 nm band pass filter was utilized as excitation filter while 430-1100 nm band pass filter was applied for emission filter.

2.2.6 Scanning electron microscope (SEM)

Morphology of materials has been investigated by scanning electron microscope at the central laboratory of Middle East Technical University. QUANTA 400F Field Emission SEM instrument with 1.2 nm resolution has been used for the analyses. Moreover, analyses were completed under high vacuum conditions.

2.2.7 Luminescence lifetime measurement

Luminescence lifetimes or decay times were recorded with an home-made instrument available in Physics Department of METU. The instrument is equipped with UV-365 pulsed LED (Prismatix model blcc-02) which was coupled to a fiber. A monochromator (Newport- 78025), photomultiplier tube (Oriel-70680), and Scott (GG420) long pass filter with 3mm thickness and 25 mm radius were used for data collection. Decay curves were recorded with the help of a multichannel scaler (Stanford Research Systems SR430). Measurements were taken from KBr pellets which were prepared from a mixture of 100 mg of KBr and 2 mg of samples.

2.2.8 Laser source for photoshoot

Photographs of synthesized phosphors have been taken under excitation of a laser source with 355 nm wavelength (Coherent-Genesis CX355-60) available in Physics Department of METU.

2.3. Synthesis of codoped $LaBO_3$ powders

In the present work, $LaBO_3$ crystalline powders have been prepared by using urea as a fuel with microwave assisted solid state synthesis method. Luminescence intensity increases nearly two times in microwave assisted solid state synthesis with respect to solid state synthesis (**Appendix A**). Lanthanum oxide (La_2O_3), boric acid (H_3BO_3) dysprosium oxide (Dy_2O_3), bismuth oxide (Bi_2O_3), cerium carbonate hydrate ($Ce_2(CO_3)_3 \cdot xH_2O$), europium oxide (Eu_2O_3), terbium oxide (Tb_4O_7) and urea ($CO(NH_2)_2$) were used as raw materials. According to their stoichiometric ratio, they were precisely weighed and thoroughly mixed in agate mortar. After transferring the mixture to a ceramic crucible, it was heated in a commercial microwave oven for 10 minutes and further 2 hours of heating was applied at 950 °C in conventional oven. Both dopants and codopants were added to the initial mixture in accordance with their mole percent in desired products. Finally, white crystalline powders of $Dy_xLa_{1-x}BO_3$, $Eu_xLa_{1-x}BO_3$, $Dy_xBi_yLa_{1-x-y}BO_3$, $Dy_xBi_yLa_{1-x}BO_3$, $Dy_xCe_yLa_{1-x-y}BO_3$, $Dy_xEu_yLa_{1-x-y}BO_3$, and $Tb_xCe_yLa_{1-x-y}BO_3$ phosphors were obtained. The molar ratio of La_2O_3 to urea is calculated as 1: 1.33, on the other side molar ratio of La_2O_3: H_3BO_3 is 1:2. Stoichiometric amounts of reactants are given in the **Table 4-10.** In addition, weight of other used materials is given in **Table 11.** Lanthanum orthobotate synthesis reaction is as follows:

$$La_2O_3(s) + 3H_3BO_3\ (s) \xrightarrow{\text{Urea}} 2LaBO_3(s) + 3H_2O\ (g) \qquad (2.3.1)$$

Table 4. Stoichiometric amounts of Dy^{3+} doped $LaBO_3$

	La_2O_3 (g)	**Dy_2O_3 (g)**
$LaBO_3$	1.69	-
$Dy_{0.05}La_{0.95}BO_3$	1.60	0.097
$Dy_{0.06}La_{0.94}BO_3$	1.59	0.116
$Dy_{0.07}La_{0.93}BO_3$	1.57	0.135
$Dy_{0.09}La_{0.91}BO_3$	1.53	0.174
$Dy_{0.11}La_{0.89}BO_3$	1.50	0.212

Table 5. Stoichiometric amounts of Eu^{3+} doped $LaBO_3$

	La_2O_3 (g)	**Eu_2O_3 (g)**
$LaBO_3$	1.69	-
$Eu_{0.01}La_{0.99}BO_3$	1.66	0.018
$Eu_{0.03}La_{0.97}BO_3$	1.64	0.055
$Eu_{0.05}La_{0.95}BO_3$	1.60	0.091
$Eu_{0.07}La_{0.93}BO_3$	1.57	0.128

Table 6. Stoichiometric amounts of Dy^{3+}/ Bi^{3+} codoped $LaBO_3$

	La_2O_3 (g)	**Dy_2O_3 (g)**	**Bi_2O_3 (g)**
$LaBO_3$	1.69	-	-
$Dy_{0.05}La_{0.95}BO_3$	1.60	0.097	-
$Dy_{0.02}Bi_{0.01}La_{0.97}BO_3$	1.64	0.039	0.0241
$Dy_{0.05}Bi_{0.01}La_{0.94}BO_3$	1.59	0.097	0.0241
$Dy_{0.07}Bi_{0.01}La_{0.92}BO_3$	1.56	0.135	0.0241
$Dy_{0.07}Bi_{0.05}La_{0.93}BO_3$	1.57	0.135	0.121
$Dy_{0.06}Bi_{0.05}La_{0.94}BO_3$	1.59	0.116	0.121
$Dy_{0.05}Bi_{0.05}La_{1.00}BO_3$	1.69	0.097	0.121

Table 7. Stoichiometric amounts of Dy^{3+}/ Ce^{3+} codoped $LaBO_3$

	La_2O_3 (g)	**Dy_2O_3 (g)**	**$(Ce_2(CO_3)_3 \cdot xH_2O)$**
$LaBO_3$	1.69	-	-
$Dy_{0.07}La_{0.93}BO_3$	1.57	0.135	-
$Dy_{0.07}Ce_{0.01}La_{0.92}BO_3$	1.55	0.135	0.0238
$Dy_{0.07}Ce_{0.03}La_{0.90}BO_3$	1.52	0.135	0.0175
$Dy_{0.07}Ce_{0.05}La_{0.88}BO_3$	1.48	0.135	0.1192
$Dy_{0.07}Ce_{0.07}La_{0.86}BO_3$	1.45	0.135	0.1669

Table 8. Stoichiometric amounts of Dy^{3+}/ Ce^{3+} codoped $LaBO_3$

	La_2O_3 (g)	**Dy_2O_3 (g)**	**$(Ce_2(CO_3)_3 \cdot xH_2O)$**
$LaBO_3$	1.69	-	-
$Dy_{0.05}Ce_{0.05}La_{0.90}BO_3$	1.52	0.097	0.1192
$Dy_{0.07}Ce_{0.05}La_{0.88}BO_3$	1.48	0.135	0.1192
$Dy_{0.09}Ce_{0.05}La_{0.86}BO_3$	1.45	0.174	0.1192
$Dy_{0.11}Ce_{0.05}La_{0.84}BO_3$	1.42	0.212	0.1192
$Dy_{0.09}Ce_{0.07}La_{0.84}BO_3$	1.42	0.174	0.1669
$Dy_{0.11}Ce_{0.07}La_{0.82}BO_3$	1.38	0.212	0.1669

Table 9. Stoichiometric amounts of Dy^{3+}/ Eu^{3+} codoped $LaBO_3$

	La_2O_3 (g)	**Dy_2O_3 (g)**	**Eu_2O_3 (g)**
$LaBO_3$	1.69	-	-
$Dy_{0.07}Eu_{0.01}La_{0.92}BO_3$	1.55	0.135	0.018
$Dy_{0.07}Eu_{0.03}La_{0.90}BO_3$	1.52	0.135	0.055
$Dy_{0.07}Eu_{0.05}La_{0.88}BO_3$	1.48	0.135	0.091
$Dy_{0.07}Eu_{0.07}La_{0.86}BO_3$	1.45	0.135	0.128

Table 10. Stoichiometric amounts of Tb^{3+}/ Ce^{3+} codoped $LaBO_3$

	La_2O_3 (g)	**Tb_4O_7 (g)**	**$(Ce_2(CO_3)_3 \cdot xH_2O)$**
$LaBO_3$	1.69	-	-
$Tb_{0.07}La_{0.93}BO_3$	1.57	0.135	-
$Tb_{0.07}Ce_{0.01}La_{0.92}BO_3$	1.55	0.135	0.024
$Tb_{0.07}Ce_{0.03}La_{0.90}BO_3$	1.52	0.135	0.072
$Tb_{0.07}Ce_{0.05}La_{0.88}BO_3$	1.48	0.135	0.119
$Tb_{0.07}Ce_{0.07}La_{0.86}BO_3$	1.45	0.135	0.167

Table 11. Moles and weight of used materials for pure $LaBO_3$ and pure $CeBO_3$.

Materials	**Mol**	**Weight (g)**
La_2O_3	5.18×10^{-3}	1.690
$Ce_2(CO_3)_3 \cdot xH_2O$	5.18×10^{-3}	2.384
Urea	6.9×10^{-3}	0.415
H_3BO_3	0.0103	0.640

CHAPTER 3

RESULTS AND DISCUSSION

3.1 X-ray Diffraction Patterns of undoped, doped, codoped $LaBO_3$

XRD patterns of $Dy_xLa_{1-x}BO_3$, $Eu_xLa_{1-x}BO_3$, $Dy_xBi_yLa_{1-x-y}BO_3$- $Dy_xBi_yLa_{1-x}BO_3$, $Dy_xCe_yLa_{1-x-y}BO_3$, $Dy_xEu_yLa_{1-x-y}BO_3$, and $Tb_xCe_yLa_{1-x-y}BO_3$ phosphors with assigned h-k-l values for $LaBO_3$ are shown in **Figure 14- 20**, respectively. Recorded diffraction peaks of all undoped, doped and codoped $LaBO_3$ powders match well with the JCPDS card number 12-0762, which indicate the phosphors were successfully synthesized by microwave solid state synthesis method. The phosphors were crystallized in an orthorhombic crystal structure with the Pnma space group and the unit cell parameters: a= 5.87 Å, b=5.10 Å, c= 8.25 Å.

In all patterns, shifts in peak positions can be observed by increasing doping or codoping amounts; however, these shifts are negligible as they are too small. Reason for these negligible shifts can be explained with the similar radius of RE^{3+} ions i.e. La^{3+}: 1.045 Å, Dy^{3+}: 0.912 Å, Eu^{3+}: 0.947 Å, Tb^{3+}: 0.923 Å, Ce^{3+}: 1.01 Å, Bi^{3+}: 1.03 Å [67, 68]. In conclusion, they can form substitutional or/ and interstitial alloy with $LaBO_3$ host matrix.

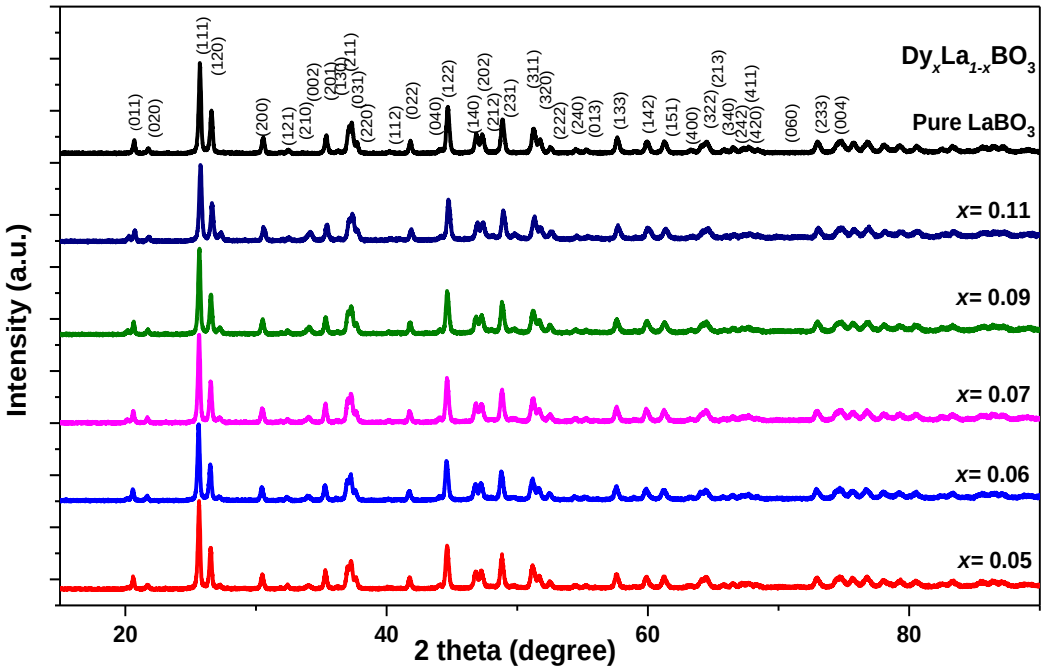

Figure 14. XRD patterns of undoped and Dy^{3+} doped $LaBO_3$

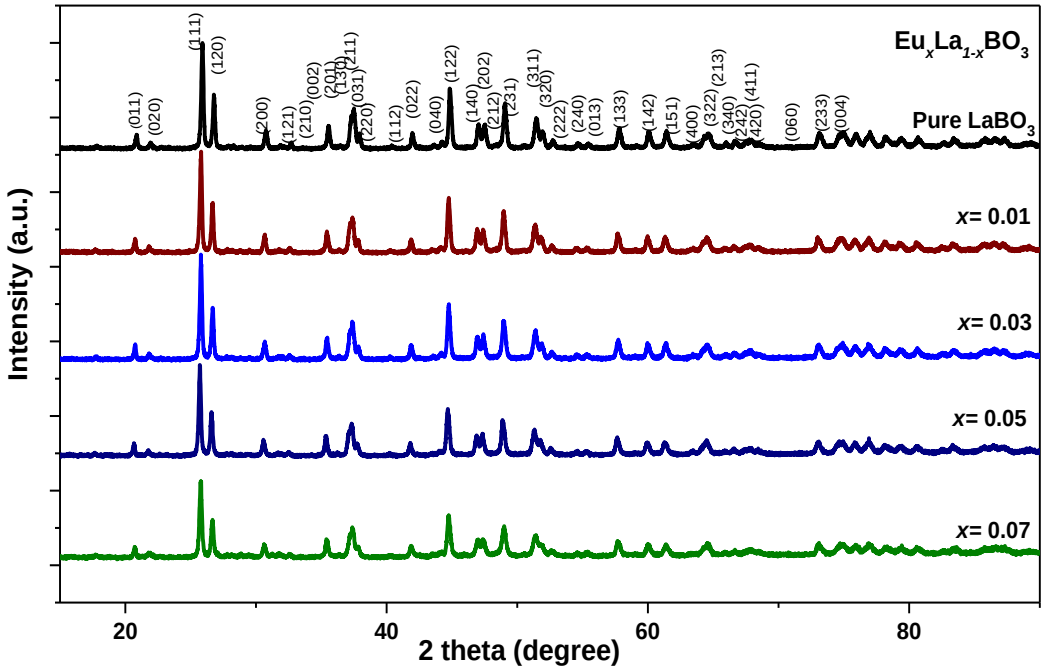

Figure 15. XRD patterns of undoped and Eu^{3+} doped $LaBO_3$

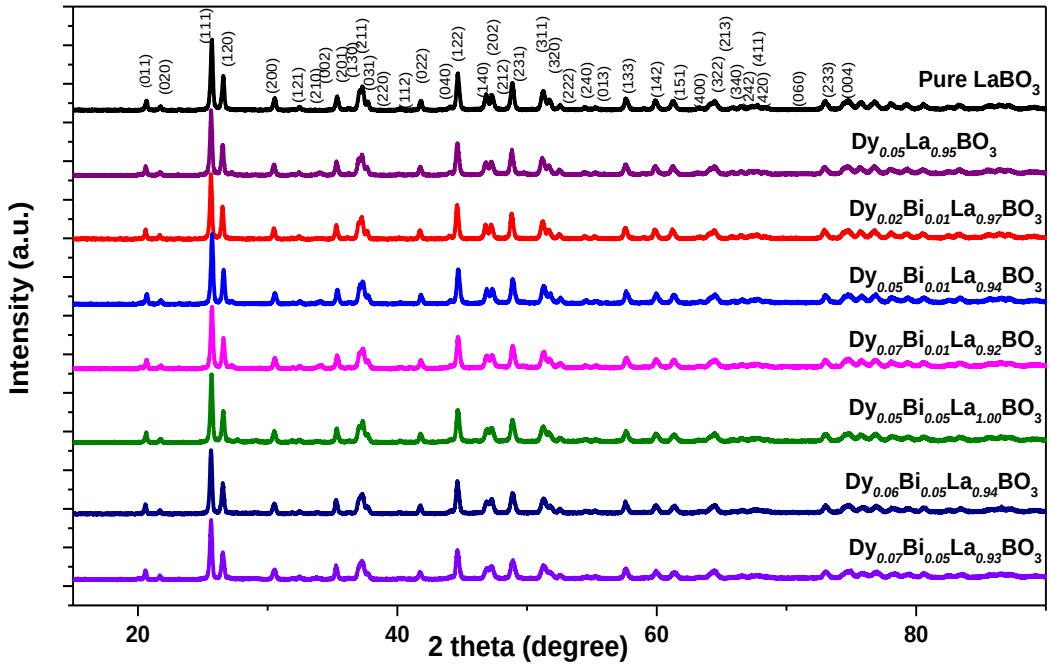

Figure 16. XRD patterns of undoped and Dy^{3+}/Bi^{3+} codoped $LaBO_3$**.**

Although recorded diffraction peaks of all samples totally match the $LaBO_3$ XRD pattern, unidentified peaks assigned as **a, b, c** with very low intensities become visible while doping amounts of Ce^{3+} reach higher values in Dy^{3+}/Ce^{3+} codoped (**Figure 17-18)** and Tb^{3+}/Ce^{3+} codoped (**Figure 20)** $LaBO_3$ samples. Higher doping amounts of both dopants and codopants may lead the formation of $CeBO_3$ and those peaks may come from the $CeBO_3$ structure. In the aspect of this view, X-ray diffraction pattern of synthesized $CeBO_3$ was matched with these unidentified peaks. We can offer that the highest three peaks of $CeBO_3$ are in accordance with those new peaks. However, there is no consistent relation between unidentified peaks and emission intensities of phosphors. Thus, they do not affect the luminescence properties of samples.

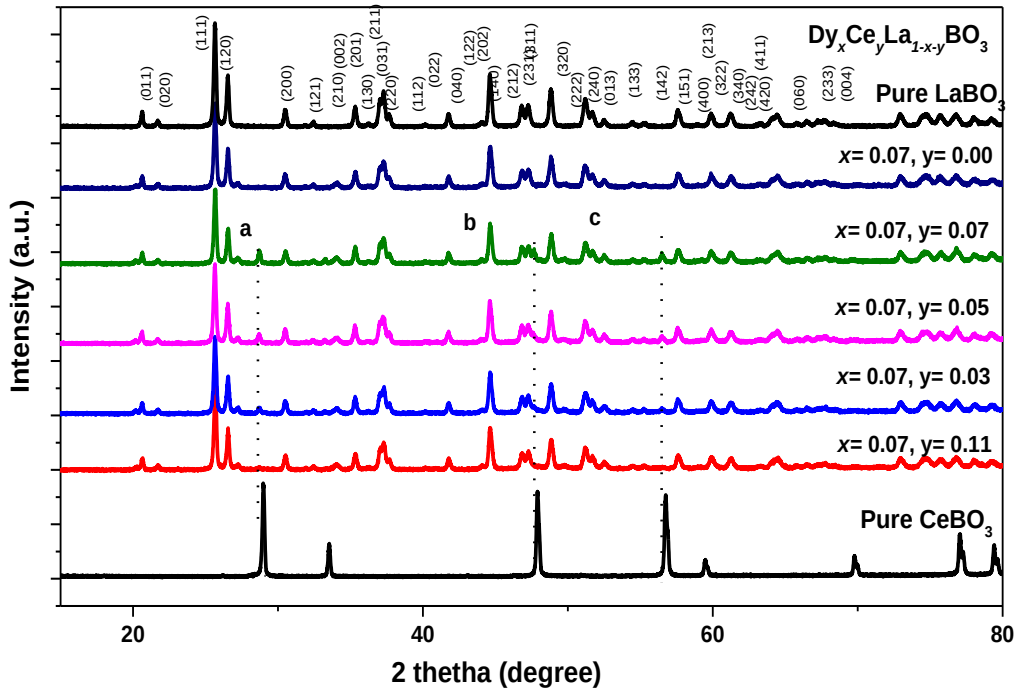

Figure 17. XRD patterns of $CeBO_3$, undoped, and Dy^{3+}/Ce^{3+} codoped $LaBO_3$.

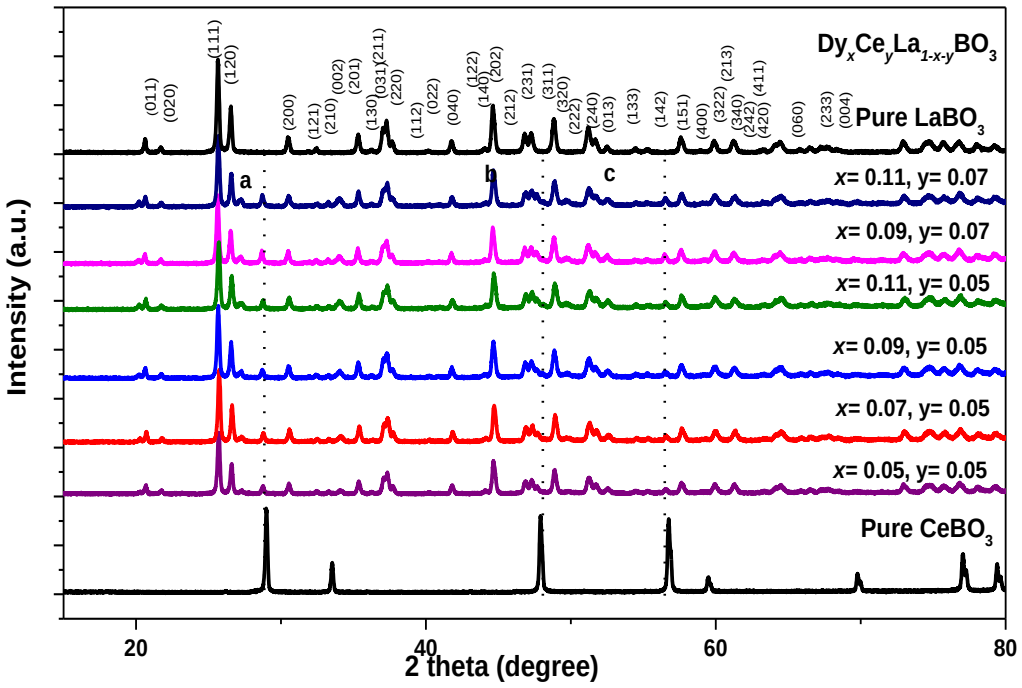

Figure 18. XRD patterns of $CeBO_3$, undoped, and Dy^{3+}/Ce^{3+} codoped $LaBO_3$.

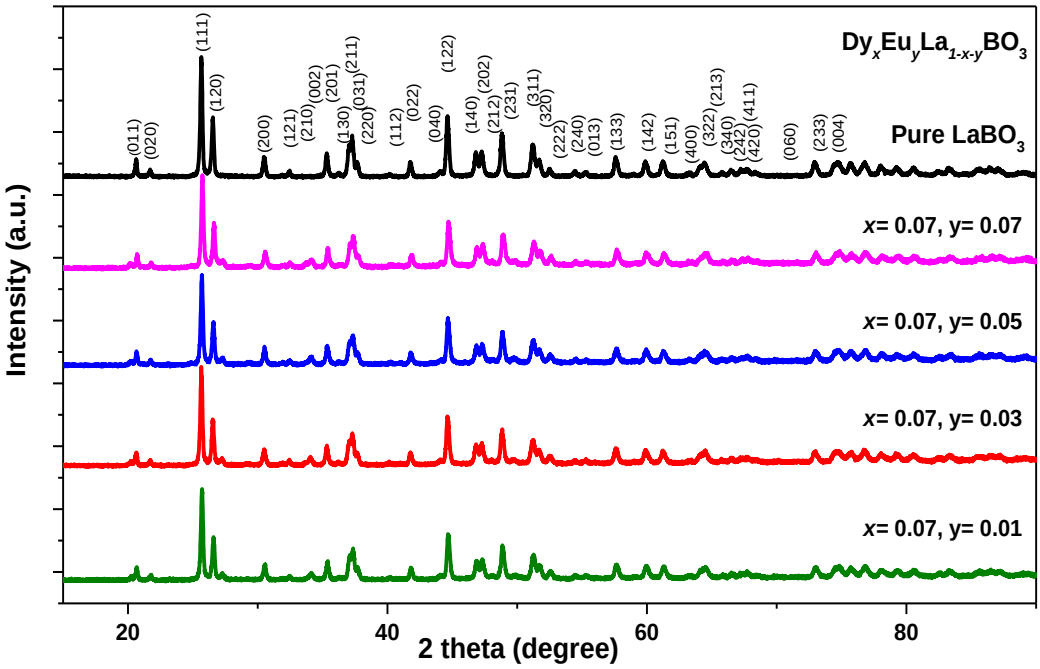

Figure 19. XRD patterns of undoped and Dy^{3+}/ Eu^{3+} codoped $LaBO_3$.

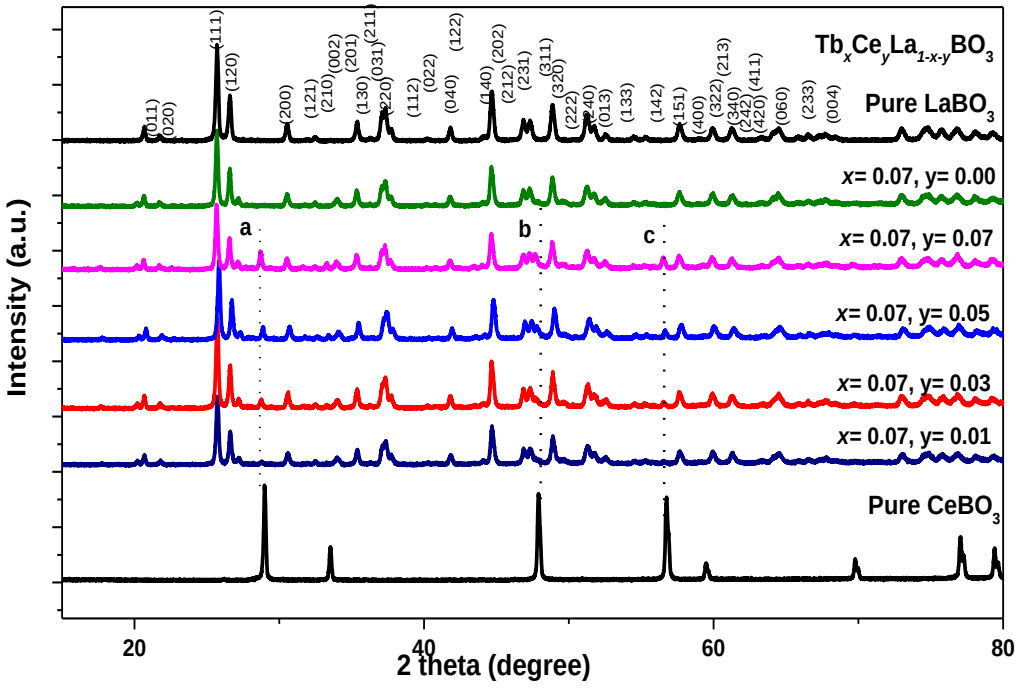

Figure 20. XRD patterns of $CeBO_3$, undoped, and Tb^{3+}/Ce^{3+} codoped $LaBO_3$

3.2 SEM images of undoped, doped, codoped $LaBO_3$

Figure 21 reveal SEM images of undoped, Dy^{3+} doped, Dy^{3+}/ Bi^{3+}; Dy^{3+}/ Ce^{3+}; Eu^{3+}/ Dy^{3+}; Tb^{3+}/ Ce^{3+} codoped $LaBO_3$ phosphors. Undoped, doped and codoped $LaBO_3$ samples show fine size and regular morphology. It can be said that codoped samples have relatively small sizes with **(Figure 21.c-f)** respect to undoped and Dy^{3+} samples (**Figure 21.a-b**). In addition, doping or codoping does not affect the morphology of host material, significantly. These properties and micron size of the phosphors may lead to have various advantages such as well slurry character and high packing densities. Thus, mixture preparation process for solid state light emitting devices is applicable with these properties [35].

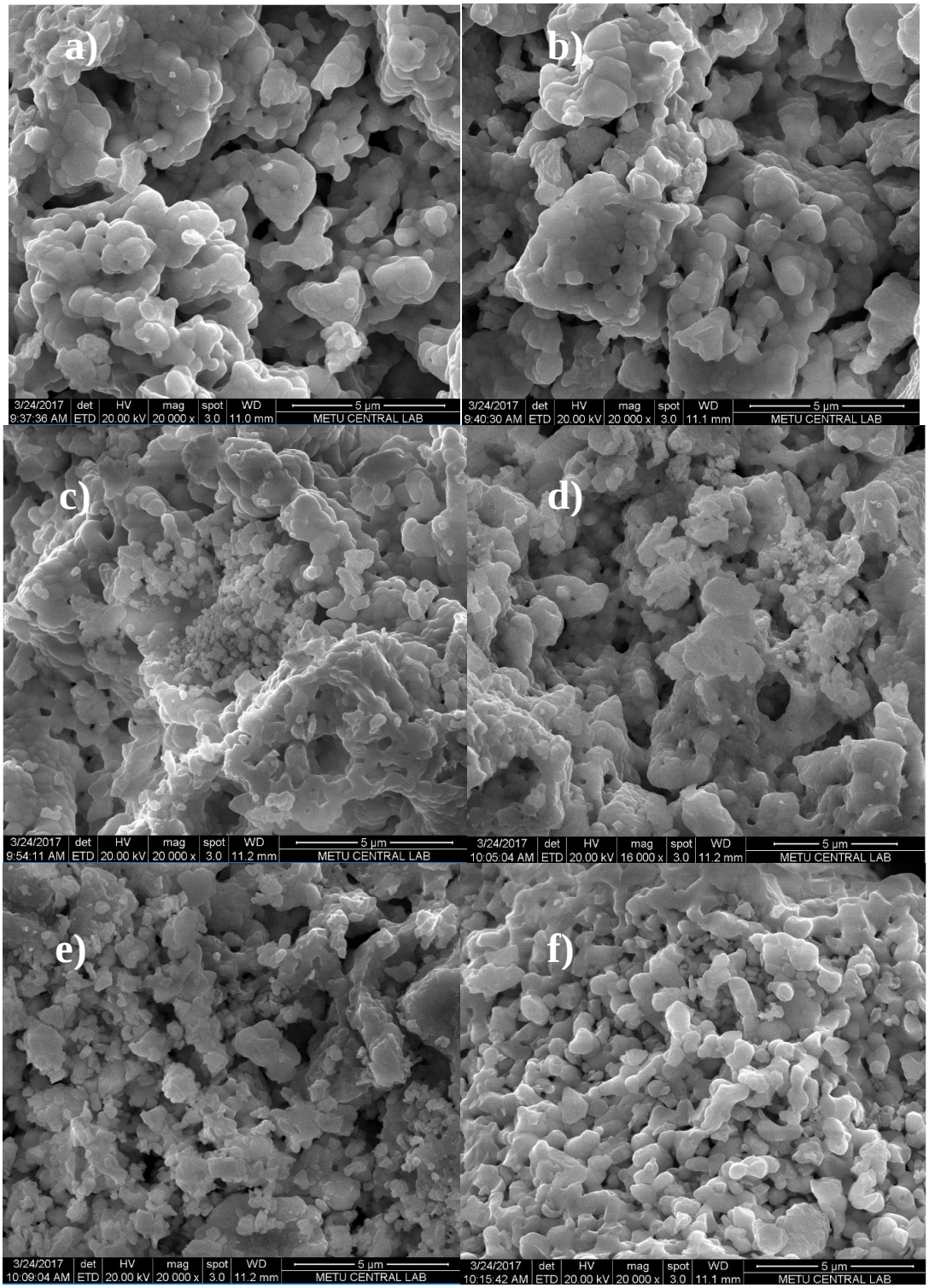

Figure 21. SEM images of **a)** undoped, **b)** Dy^{3+} doped, **c)** Dy^{3+}/ Ce^{3+} codoped, **d)** Dy^{3+}/ Eu^{3+} codoped, **e)** Dy^{3+}/ Bi^{3+} codoped, **f)** Tb^{3+}/ Ce^{3+} codoped $LaBO_3$ materials

3.3 ATR-FTIR spectra of undoped, doped, codoped $LaBO_3$

The ATR-FTIR spectra of $Dy_xLa_{1-x}BO_3$, $Eu_xLa_{1-x}BO_3$, $Dy_xBi_yLa_{1-x-y}BO_3$-$Dy_xBi_yLa_{1-x}BO_3$, $Dy_xCe_yLa_{1-x-y}BO_3$, $Dy_xEu_yLa_{1-x-y}BO_3$, and $Tb_xCe_yLa_{1-x-y}BO_3$ samples are demonstrated in **Figure 22-28,** respectively**.** Aragonite type $LaBO_3$ has trigonal planar borate units (BO_3^{3-}). Vibrational modes of BO_3^{3-} units were detected in the range of 1650 to 550 cm^{-1}. Band around 1245 cm^{-1} is associated with asymmetric stretching (v3); band at 940 cm^{-1} is attributed to symmetric stretching (v1); the band centered at 708 cm^{-1} corresponds to out of plane bending band (v2); and the bands at 591 and 611 cm^{-1} belong to in-plane bending (v4) modes of BO_3^{3-} group. All of the vibrational modes of BO_3^{3-} planar borate units have been detected clearly for all synthesized $LaBO_3$ crystalline powder materials. It can be noted that ATR results support the XRD patterns of samples. Therefore, samples were prepared successfully according to our previous studies and literature [57, 54].

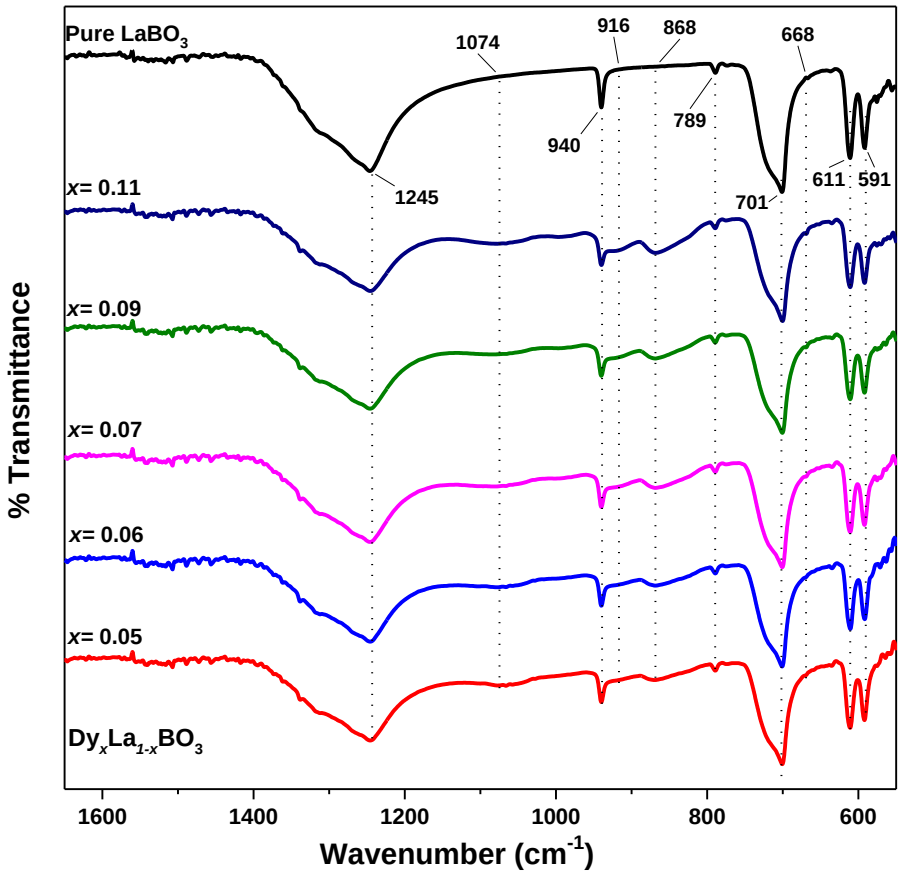

Figure 22. ATR spectra of undoped and Dy^{3+} doped $LaBO_3$ materials.

No significant changes or new bands were observed in spectra of Eu^{3+} doped (**Figure 23**) and Dy^{3+}/Bi^{3+} codoped (**Figure 24**) $LaBO_3$ samples with low doping amounts. On the other hand, small and new bands at 1074, 916, 868, 668 cm^{-1} were observed for Dy^{3+} doped (**Figure 22)**, Dy^{3+}/Ce^{3+} codoped (**Figure 25-26**), Dy^{3+}/Eu^{3+} codoped (**Figure 27**), Tb^{3+}/Ce^{3+} codoped (**Figure 28**) $LaBO_3$ phosphors. Those bands become more prominent with increasing concentrations. Higher amounts of dopants or codopants may lead to band changes in their ATR spectra.

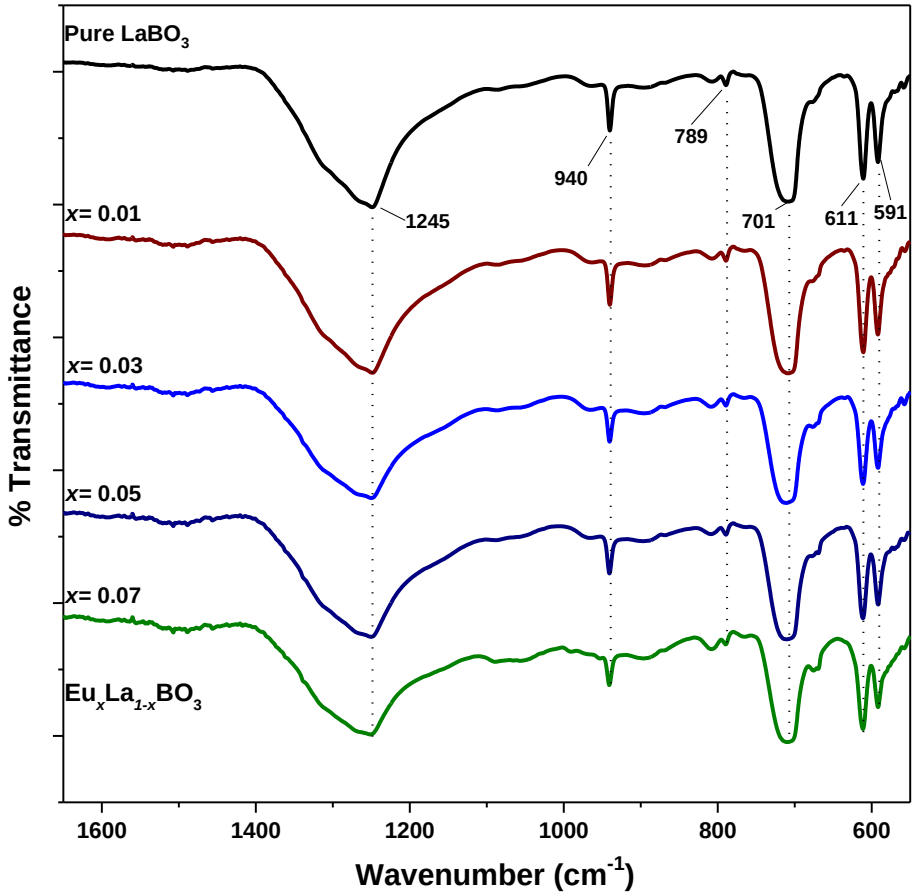

Figure 23. ATR spectra of undoped and Eu^{3+} doped $LaBO_3$ materials.

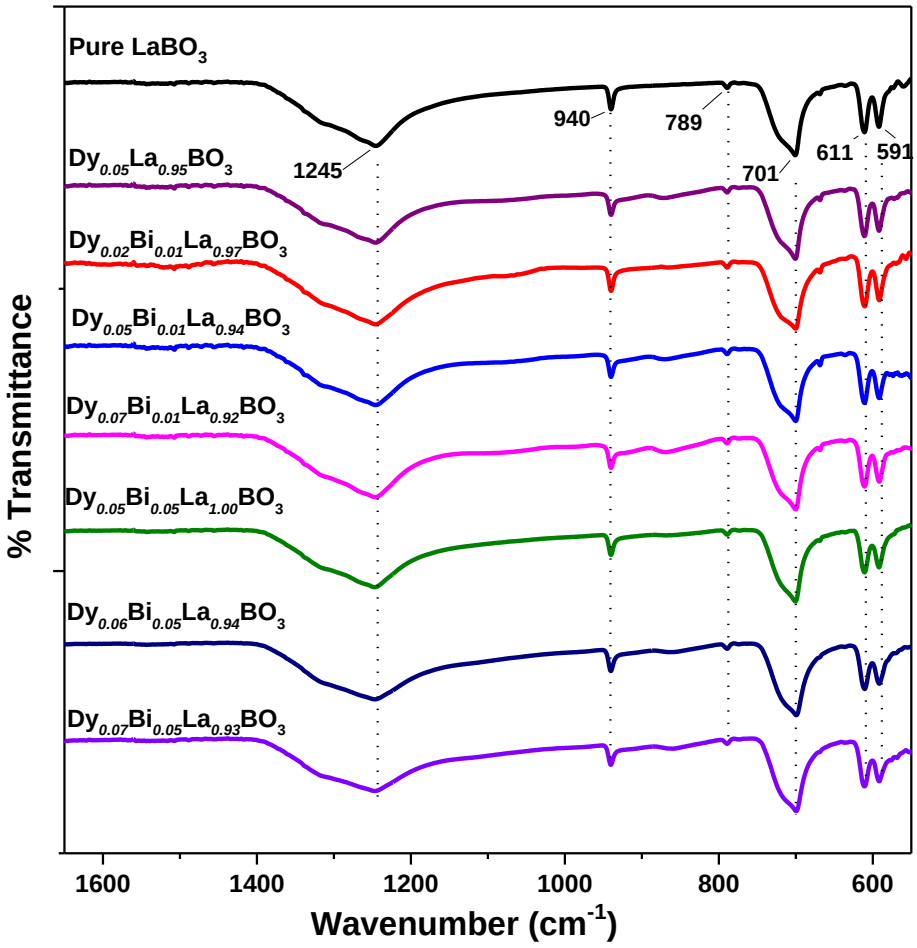

Figure 24. ATR spectra of undoped and Dy^{3+}/ Bi^{3+} codoped $LaBO_3$ materials.

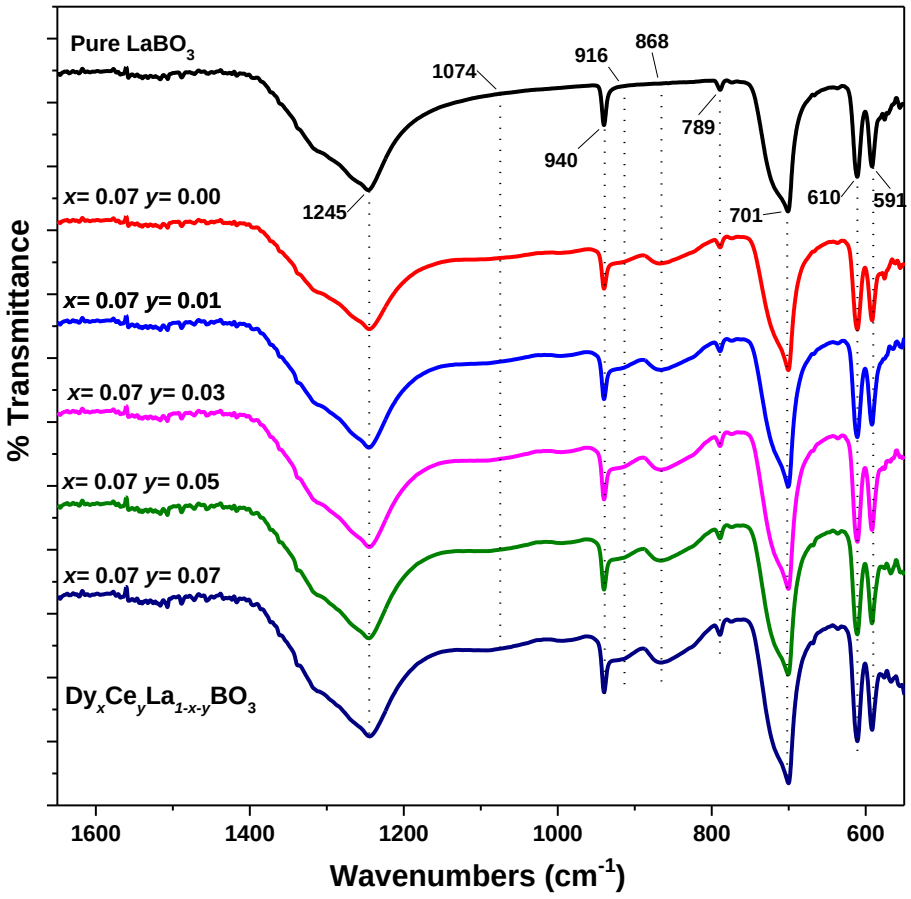

Figure 25. ATR spectra of undoped and Dy^{3+}/Ce^{3+} codoped $LaBO_3$ materials.

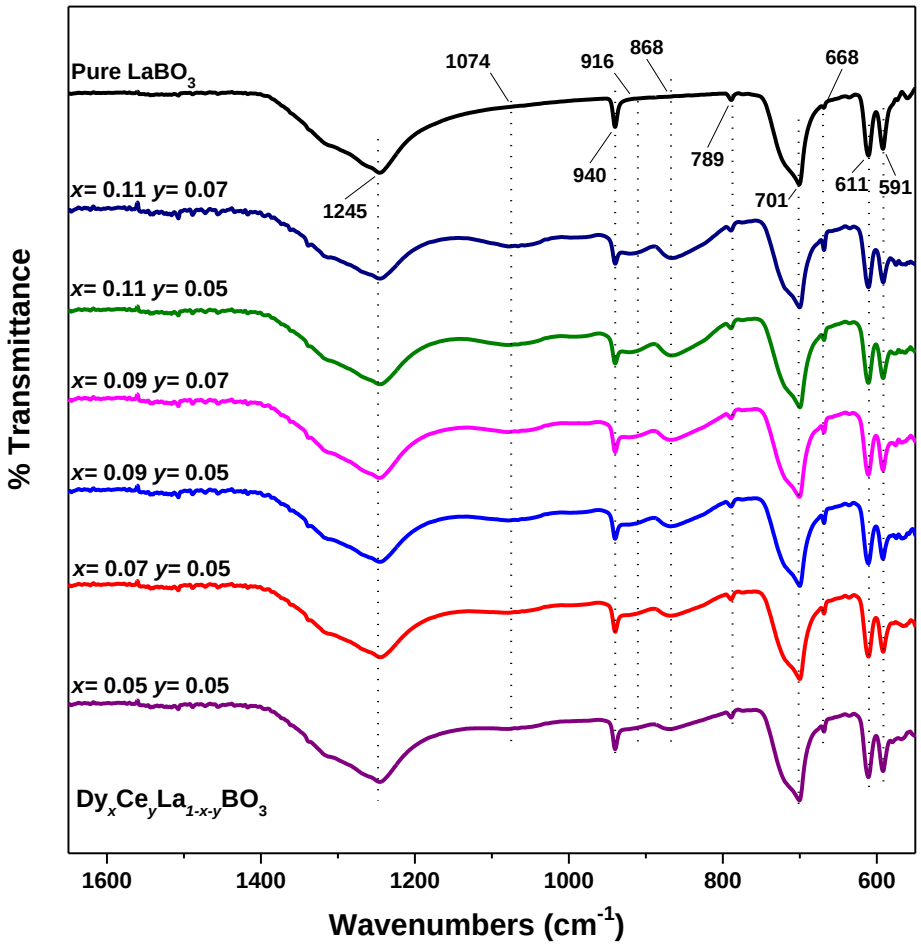

Figure 26. ATR spectra of undoped and Dy^{3+}/Ce^{3+} codoped $LaBO_3$ materials.

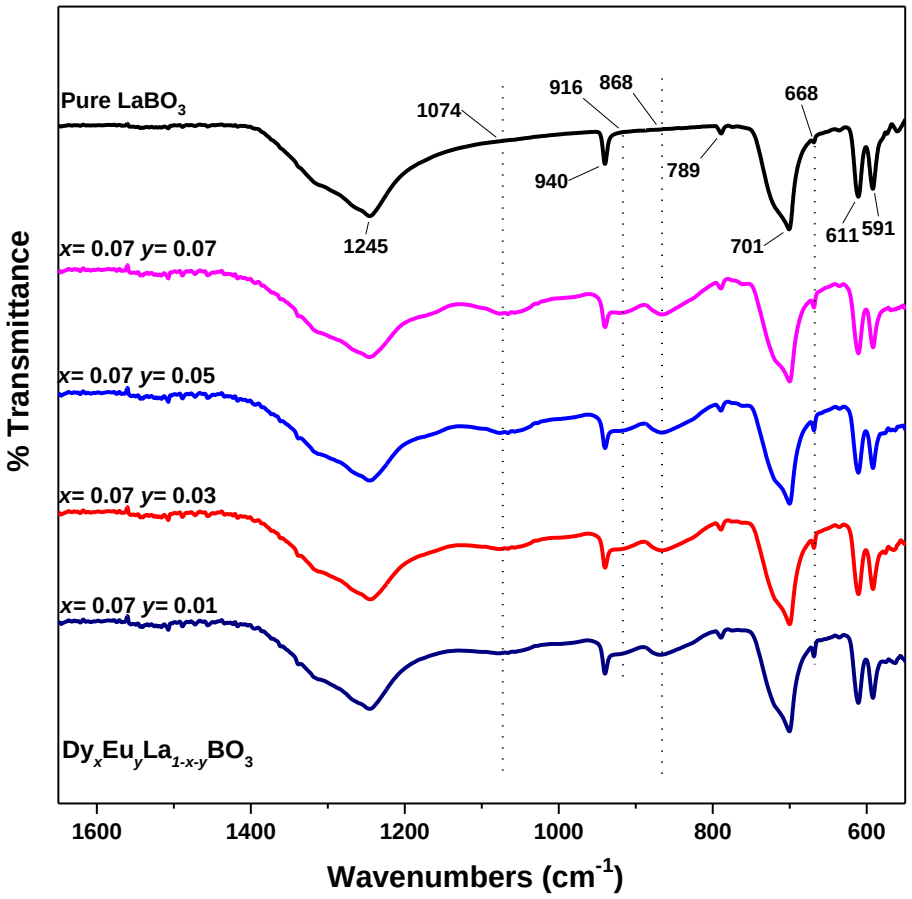

Figure 27. ATR spectra of undoped and Dy^{3+}/ Eu^{3+} codoped $LaBO_3$ materials.

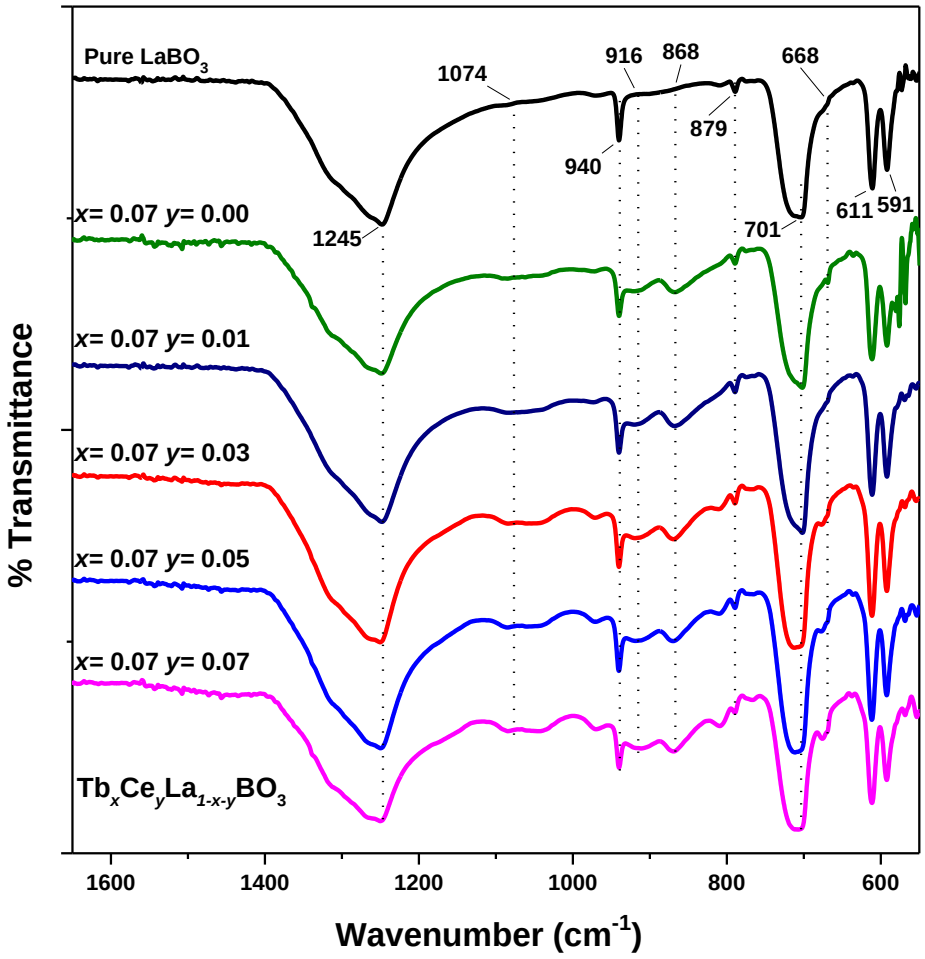

Figure 28. ATR spectra of undoped and Tb^{3+}/Ce^{3+} codoped $LaBO_3$ materials.

3.4 Far- IR results of undoped, doped, codoped $LaBO_3$

Vibrational modes of lanthanide elements are expected to be in low frequency region as they are heavy atoms. Far-IR region of electromagnetic spectrum was studied in order to examine low frequency modes of samples. There is no study about low frequency region for similar compounds in literature. Thus, there may be difficulties in definition of those spectra. Recorded Far-IR spectra of our samples may explain nature of doping and its relation with luminescence. **Figure 29- 34** show Far-IR spectra of $Dy_xLa_{1-x}BO_3$, $Eu_xLa_{1-x}BO_3$, $Dy_xBi_yLa_{1-x-y}BO_3$, $Dy_xCe_yLa_{1-x-y}BO_3$, $Dy_xEu_yLa_{1-x-y}BO_3$, and $Tb_xCe_yLa_{1-x-y}BO_3$, respectively.

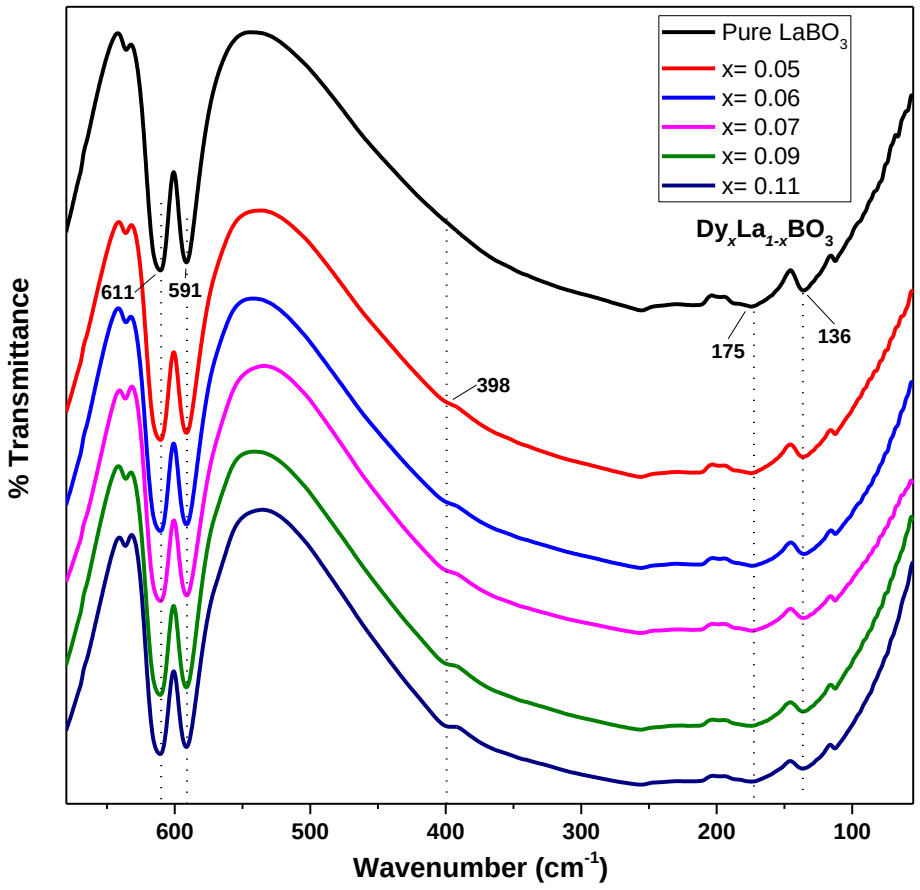

Figure 29. Far-IR spectra of undoped and Dy^{3+} doped $LaBO_3$ materials.

In-plane bending (ν4) modes of BO_3^{3-} group which are located on 591 and 611 cm^{-1} band positions are also observed in Far-IR spectra for all materials. In addition, low frequency bands appeared at 175 and 136 cm^{-1} for all undoped, doped, and codoped $LaBO_3$ samples. Therefore, these bands are considered to be La-O vibrational modes in La-O-B network. A new band appears at 398 cm^{-1} for all Dy^{3+} included samples. When doping amount of Dy^{3+} ion is increased, relative intensity of this peak becomes more prominent. Moreover, the band is not observed in the $LaBO_3$ spectrum and spectrum of $CeBO_3$ sample which is shown in **Figure 35.c**. This band must be associated with Dy-O modes of $DyBO_3$ considering that the band is also observed at 398 cm^{-1} in $DyBO_3$ spectra (**Figure 35.b**). Thus, the new band at 398 cm^{-1} may be correlated with Dy^{3+} ion which can change the $LaBO_3$ vibrational modes or create some new bands for Dy-BO_3. In addition, Dy^{3+} ions may prefer both interstitial and substitutional displacements at the lower concentrations. However, substitutional displacements may be become more prominent at higher concentrations. Observation of 398 cm^{-1} band in $DyBO_3$ spectra may support the assignment of the peak to $DyBO_3$ vibrational modes.

A new band peaked at 560 cm^{-1} is observed with increasing concentration of Eu^{3+} (7%) doped $LaBO_3$ in **Figure 30** and Dy^{3+}/ Eu^{3+} codoped $LaBO_3$ in **Figure 33**. This band is associated with Eu-O modes of $EuBO_3$ as the band is detected in $EuBO_3$ spectra (**Figure 35.d**). Thus, the band may be correlated with substitutional displacement of Eu^{3+} ion at higher concentrations.

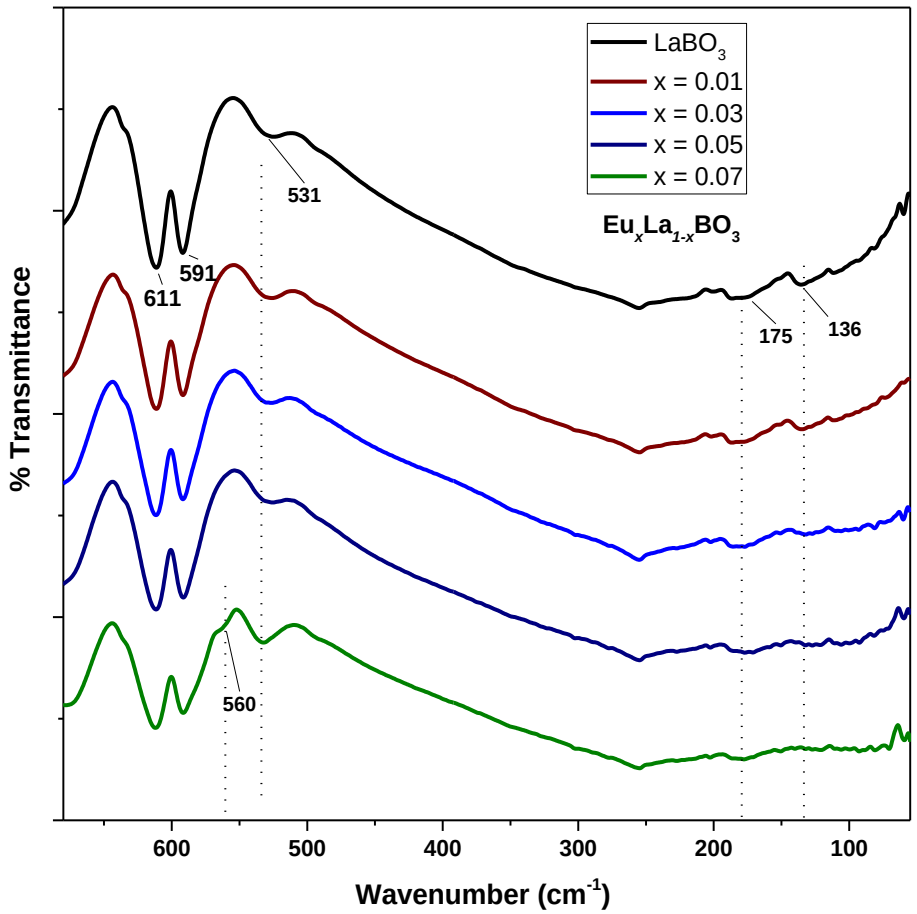

Figure 30. Far-IR spectra of undoped and Eu^{3+} doped $LaBO_3$ materials.

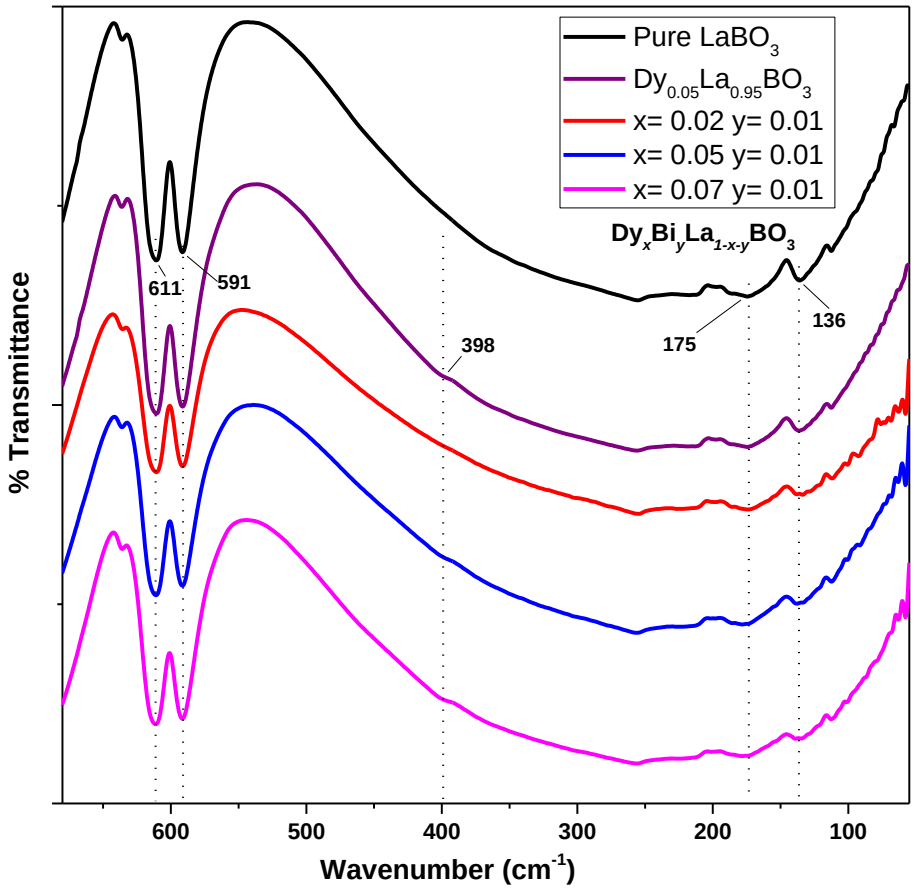

Figure 31. Far-IR spectra of undoped and Dy^{3+}/Bi codoped $LaBO_3$ materials.

In **Figure 32.a-b**, a new band was observed at around the 528 cm^{-1} for Dy^{3+}/Ce^{3+} codoped $LaBO_3$ materials while it was not observed in the spectrum of $LaBO_3$ samples. In addition to that the band becomes visible with the increase in the concentration of Ce^{3+} ions. Thus, this band might be based on the Ce-O vibrational modes in La-O-B network. The reason of the absence of this band in $CeBO_3$ spectra (**Figure 35.c)** may be the lower amount of $CeBO_3$ sample included in the measurement. In addition, Ce^{3+} ions may prefer only interstitial displacement.

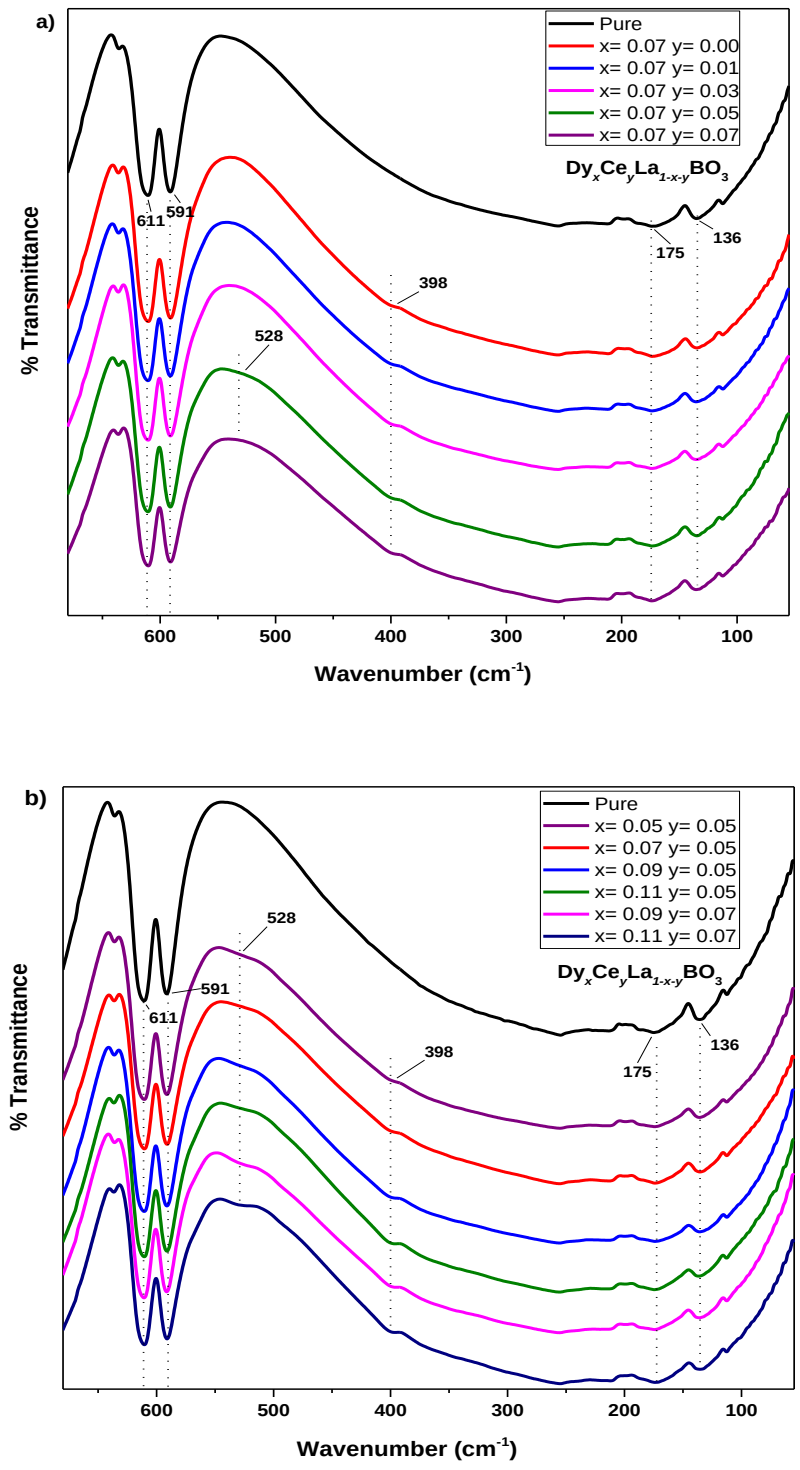

Figure 32. Far-IR spectra of undoped and Dy^{3+}/Ce^{3+} codoped $LaBO_3$ materials.

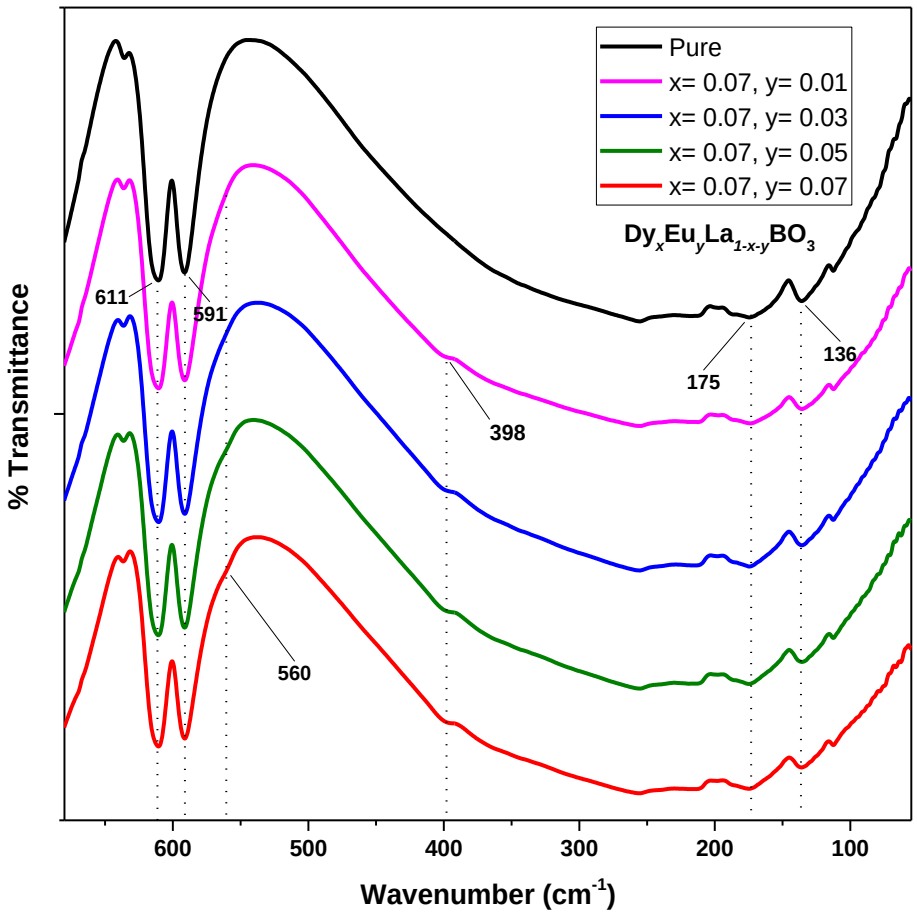

Figure 33. Far-IR spectra of undoped and Dy^{3+}/Eu^{3+} codoped $LaBO_3$ materials

Another new band was observed at around 396 cm^{-1} in the spectra of Tb^{3+}/ Ce^{3+} codoped $LaBO_3$ samples (**Figure 34**). Moreover, a band at 395 cm^{-1} was observed in $TbBO_3$ spectra (**Figure 35.a**). Since the band does not exist in the spectra of both $LaBO_3$ and $CeBO_3$, but only observed in the $TbBO_3$ spectrum, the band may be associated with the substitutional displacement of Tb^{3+} ion similar in the Dy^{3+} and Eu^{3+} ions case. Thus, this band must be associated with Tb-O modes of $TbBO_3$ considering that the band exists in $TbBO_3$ spectra.

It is important to note that Tb^{3+}/ Ce^{3+} codoped and Eu^{3+} doped samples were synthesized with the La_2O_3 (1) source while La_2O_3 (2) was used in other synthesis processes. When spectra of Tb^{3+}/ Ce^{3+} codoped (**Figure 34**) and Eu^{3+} doped samples (**Figure 30**) investigated, a new band was detected at 531 cm^{-1}. Given the band appeared in both undoped and Tb^{3+}/ Ce^{3+} codoped and Eu^{3+} doped $LaBO_3$ materials, this peak is most likely be correlated with the La_2O_3 source. This could be an impurity in the reactant. In a previous study of our group by Metehan et al. with the La_2O_3 (1) source the band is also observed in the spectra of both undoped and doped $LaBO_3$ samples [69]. However, the band becomes broader as the doping amount of Ce^{3+} ion increases in the spectra of Tb^{3+}/Ce^{3+} codoped $LaBO_3$ materials. This broadness may due to the overlap with nearby 528 cm^{-1} band of Ce-O vibration as mentioned above.

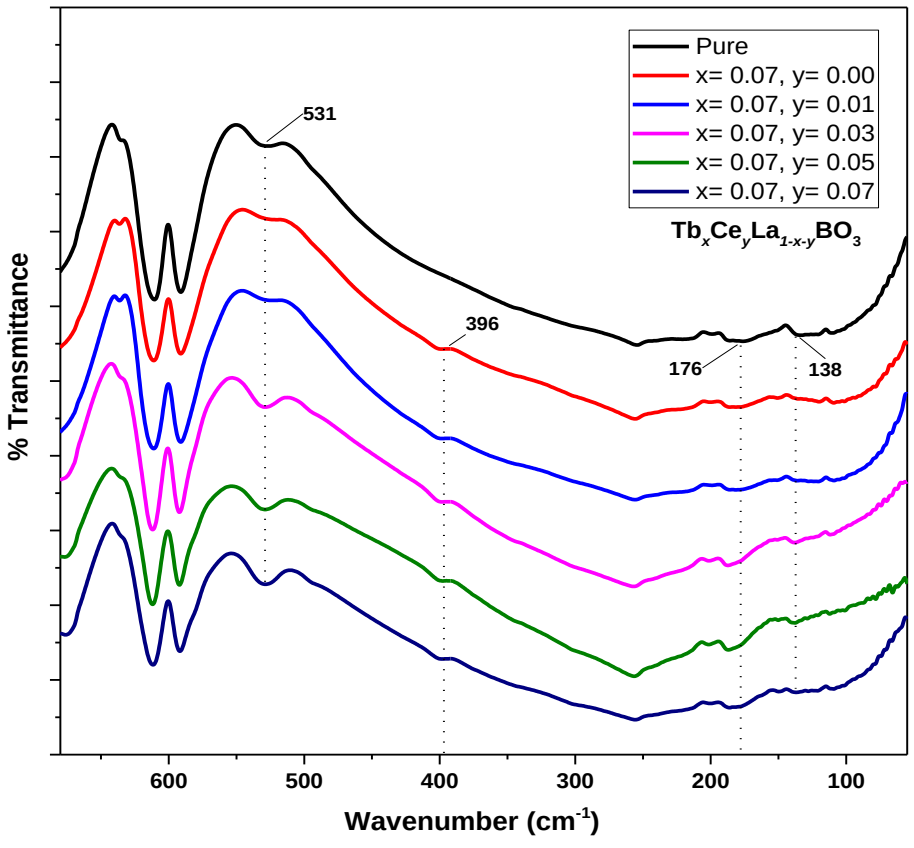

Figure 34. Far-IR spectra of undoped and Tb^{3+}/Ce^{3+} codoped $LaBO_3$ materials

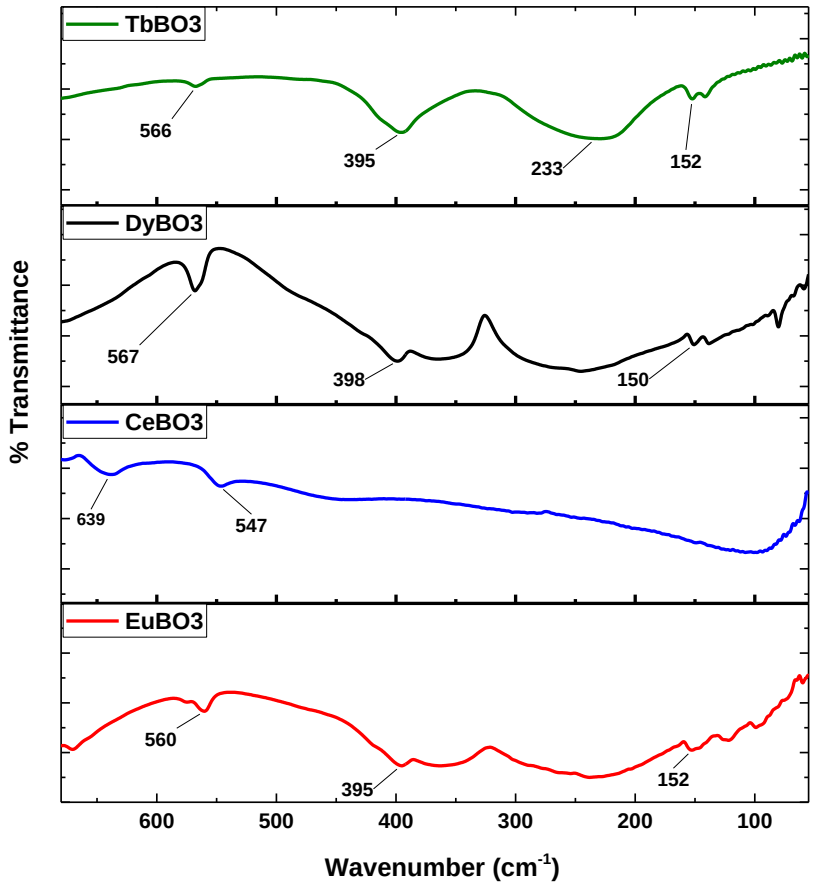

Figure 35. Far-IR spectra of **a)** $TbBO_3$, **b)** $DyBO_3$, **c)** $CeBO_3$, **d)** $EuBO_3$ material

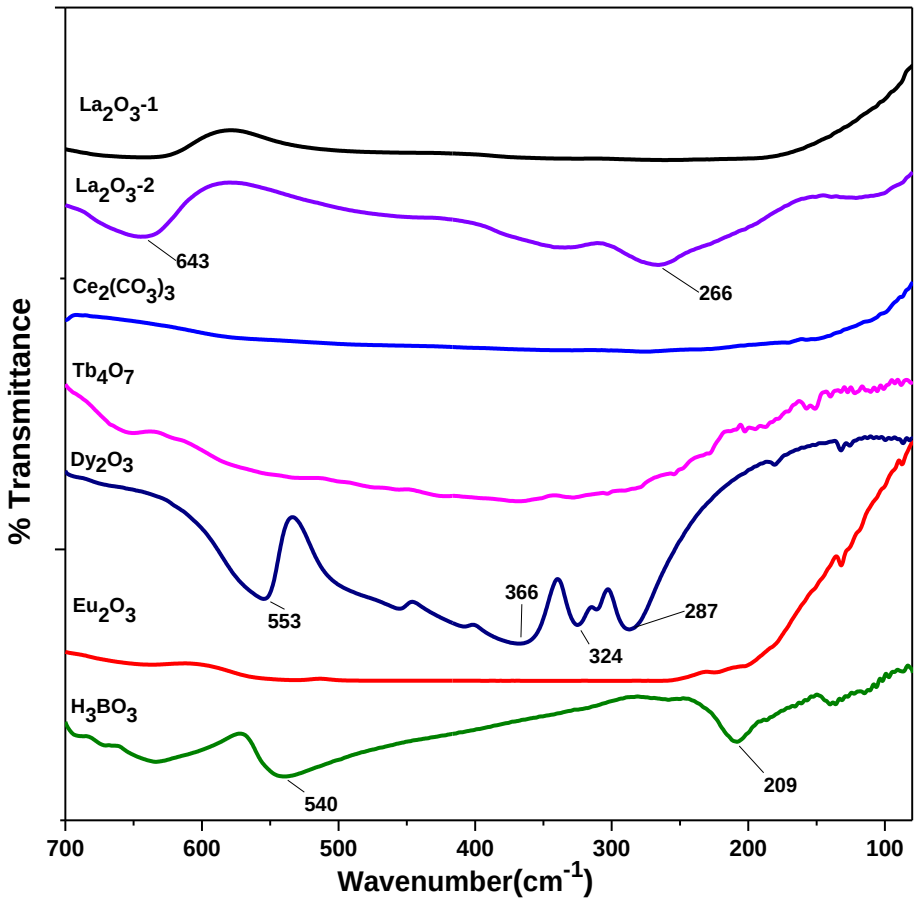

Figure 36. Far-IR spectra of oxides of rare earth elements and boric acid.

Figure 36 represents the Far-IR spectra of oxides of rare earth elements and boric acid. According to the spectra low frequency vibrational modes may pertain to La-O stretching. Any bands of boric acid were not observed in the spectrums of products. It can be concluded that vibrational modes of heavier atoms present at the low frequencies.

3.5 Photoluminescence (PL) results of undoped, doped, codoped $LaBO_3$

The luminescence properties of $LaBO_3$ materials which are doped or codoped with various percentage of trivalent rare earth elements (Ce^{3+}, Dy^{3+}, Tb^{3+}, Eu^{3+}) were investigated at room temperature. Observed minimal deviations and weak negative bands are due to imperfect background correction with undoped $LaBO_3$ in the spectra. In addition, Y/B ratios did not change much with the change in the Dy^{3+} ion concentration as expected since Dy, other dopants and La ions have similar radius (i.e. La^{3+}: 1.045 Å, Dy^{3+}: 0.912 Å, Eu^{3+}: 0.947 Å, Tb^{3+}: 0.923 Å, Ce^{3+}: 1.01 Å, Bi^{3+}: 1.03 Å) [4]. Yellow emission of Dy^{3+} is higher than the blue one in all samples. Thus, it can be said that Dy^{3+} ions prefer the low symmetry site because of the similar radius size of Dy^{3+} and the La^{3+} ions in the host material.

Photoluminescence excitation (PLE) spectra of Dy^{3+} doped $LaBO_3$ phosphors at 575 nm emission wavelength is given in **Figure 37.a.** An excitation peak with highest intensity was observed at 351 nm. **Figure 37.b** shows emission spectra (PL) of Dy^{3+} doped $LaBO_3$ phosphors upon 351 nm excitation. The phosphors emitted three bands in 450-700 nm region at this excitation wavelength. The blue emission (485 nm) corresponds to $^4F_{9/2} \rightarrow {}^8H_{15/2}$ transition, the strongest yellow emission (575 nm) is associated with $^4F_{9/2} \rightarrow {}^6H_{13/2}$ transition, and the weak peak (665 nm) is related to the transition from $^4F_{9/2}$ to $^6H_{11/2}$. Obtained emission bands are consistent with the literature [19]. These products were prepared in order to investigate the best luminescence intensities with the Dy^{3+} ion doping, including codoped samples. The results may also offer possible energy transfer mechanisms for codoped samples.

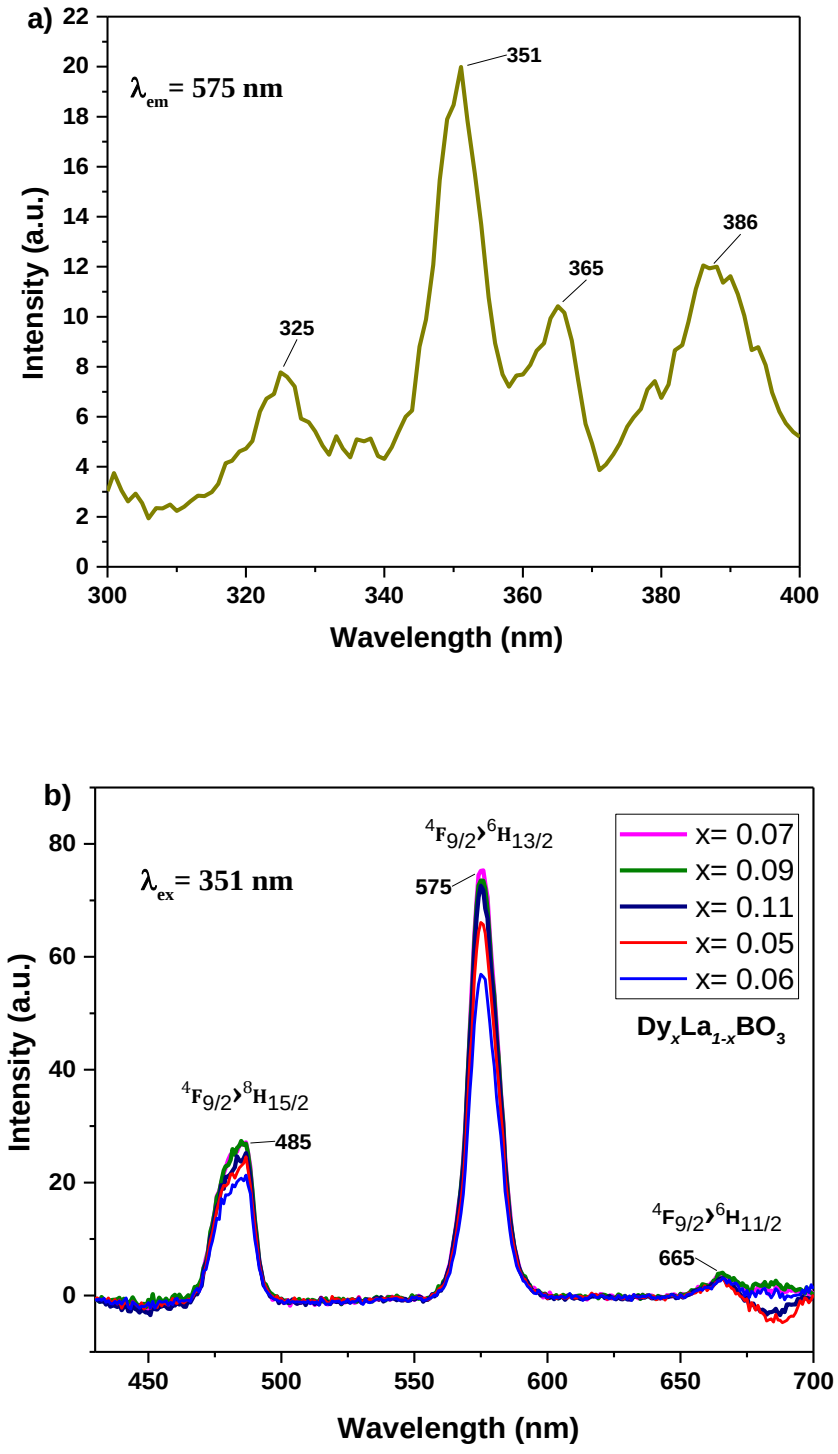

Figure 37. a) Excitation spectra, **b)** emission spectra of Dy^{3+} doped $LaBO_3$ materials

Figure 38.a shows PLE spectra of Eu^{3+} doped $LaBO_3$ materials at 615 nm emission wavelength. Highest excitation peak was observed at 394 nm. **Figure 38.b** exhibits PL spectra of Eu^{3+} doped $LaBO_3$ materials under 394 nm excitation. Two main emission bands are observed in 450-700 nm region from the phosphors. Emission centered at 615 nm and 590 nm are due to $^5D_0 \rightarrow {}^7F_2$, $^5D_0 \rightarrow {}^7F_1$ electronic transitions, respectively. These transitions are also consistent with literature [26]. As the concentration of Eu^{3+} ion increases from 1 to 7 percent, luminescence intensities of phosphors gradually increase. These phosphors were prepared to investigate the best luminescence intensities with Eu^{3+} ion doping, including codoped samples. Additionally, spectra of those products may explain possible energy transfer mechanisms for codoped samples.

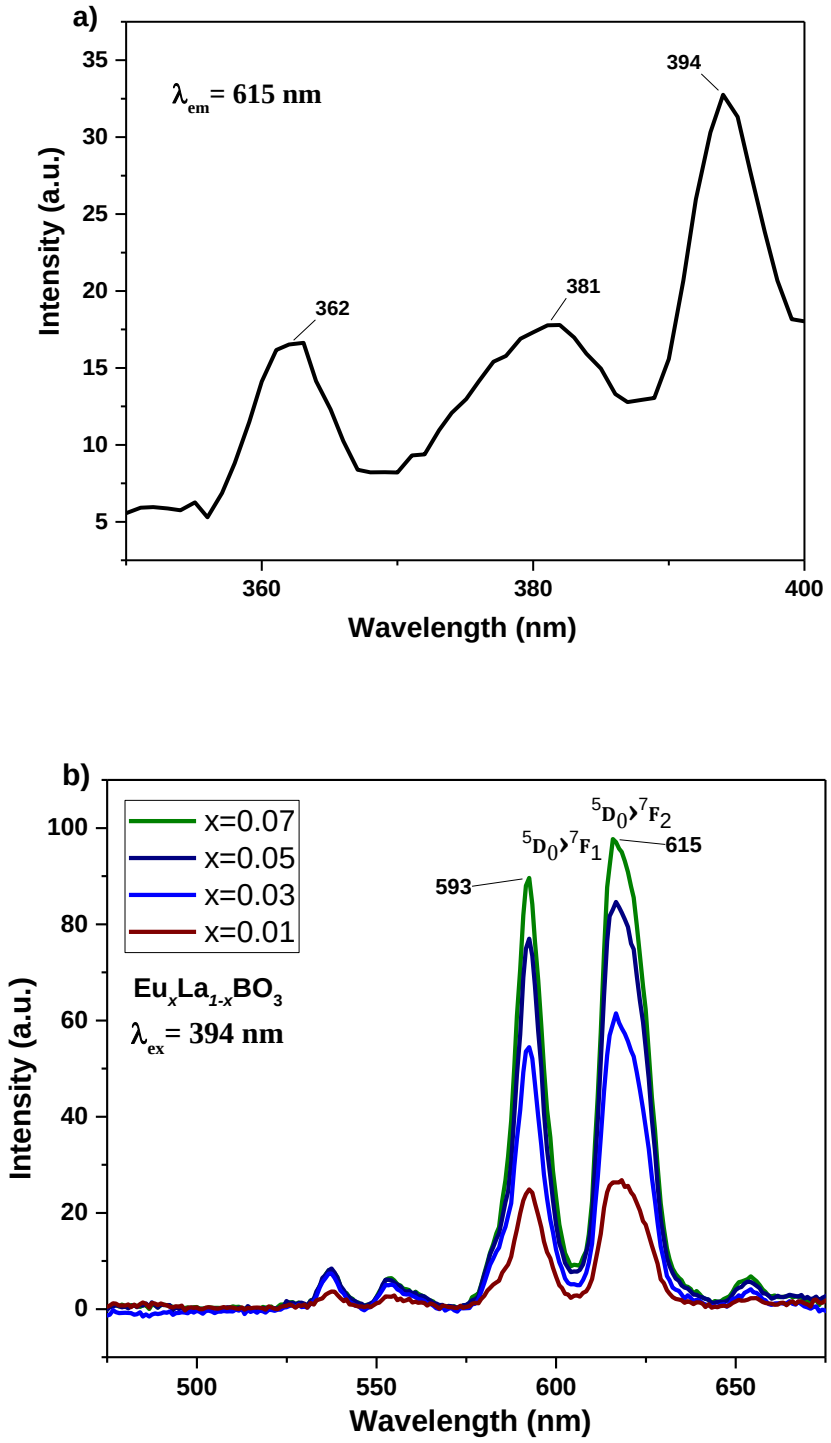

Figure 38. **a)** Excitation spectra**, b)** emission spectra of Eu^{3+} doped $LaBO_3$ materials.

PLE spectra of Dy^{3+}/ Bi^{3+} codoped $LaBO_3$ at 575 nm emission wavelength is shown in **Figure 39.a.** Excitation peak at 351 nm associated with Dy^{3+} ion has the highest intensity. The PL spectra of Dy^{3+} doped and Dy^{3+}/ Bi^{3+} codoped samples are demonstrated in **Figure 39.b.** Three emission bands of Dy^{3+} (485 nm, 575 nm and 665 nm) were observed upon 351 nm excitation wavelength. Luminescence intensities of band emissions becomes lower with the adding Bi^{3+} ions as a codopant. Even low concentrations of Bi^{3+} ions (1 %) cause considerable decrease in intensity of phosphors. Although different concentration variations of Dy^{3+}/ Bi^{3+} codoped samples were synthesized, no enhancement in luminescent intensity was observed. Thus, Bi^{3+} ions are not good sensitizer for Dy^{3+} ions in $LaBO_3$ host structure. There may be no possible energy transfer between Dy^{3+} and Bi^{3+} ions in $LaBO_3$ host matrix.

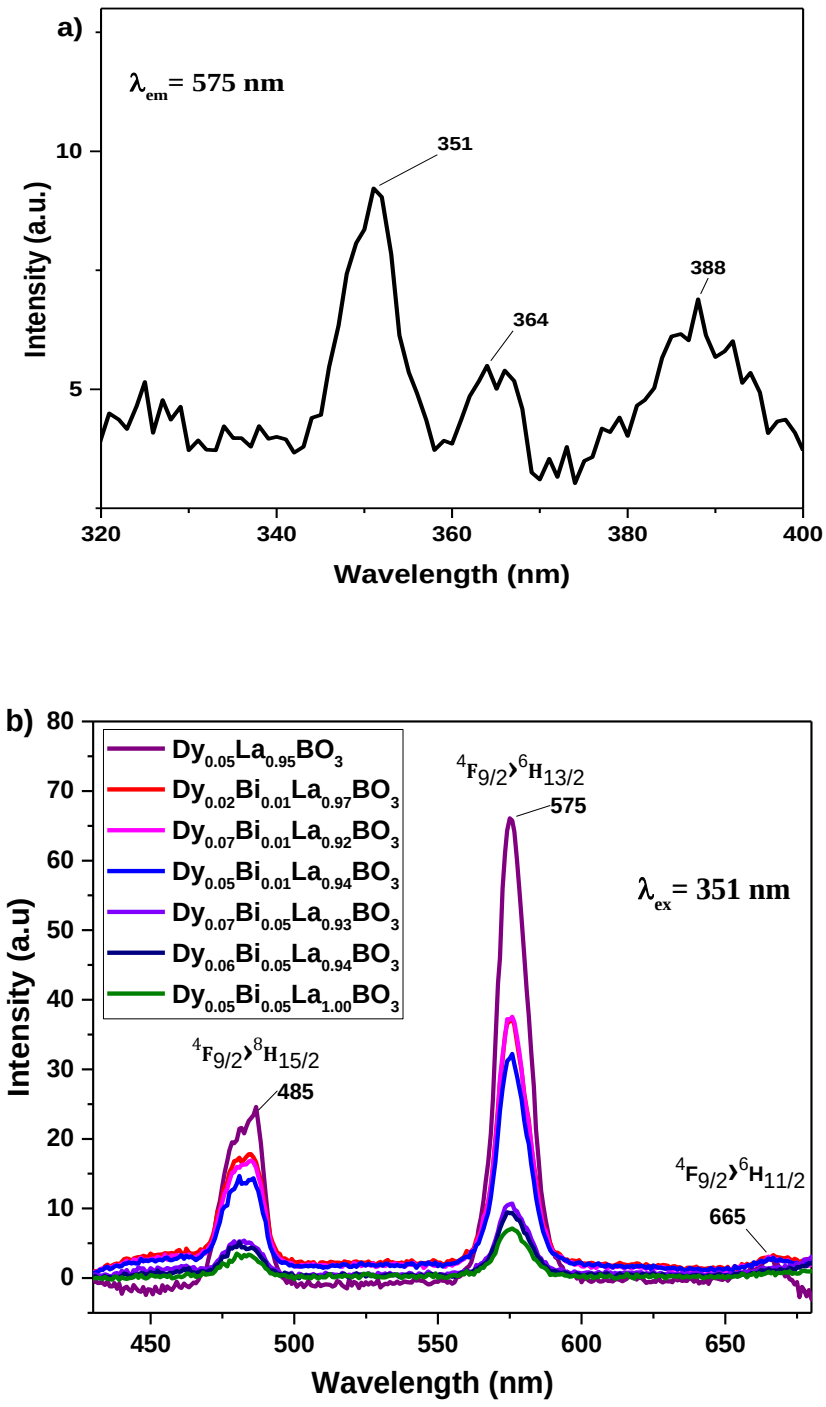

Figure 39. a) Excitation spectra of Dy^{3+}/ Bi^{3+} codoped $LaBO_3$, **b)** emission spectra of 5 % Dy^{3+} and Dy^{3+}/ Bi^{3+} codoped $LaBO_3$ materials.

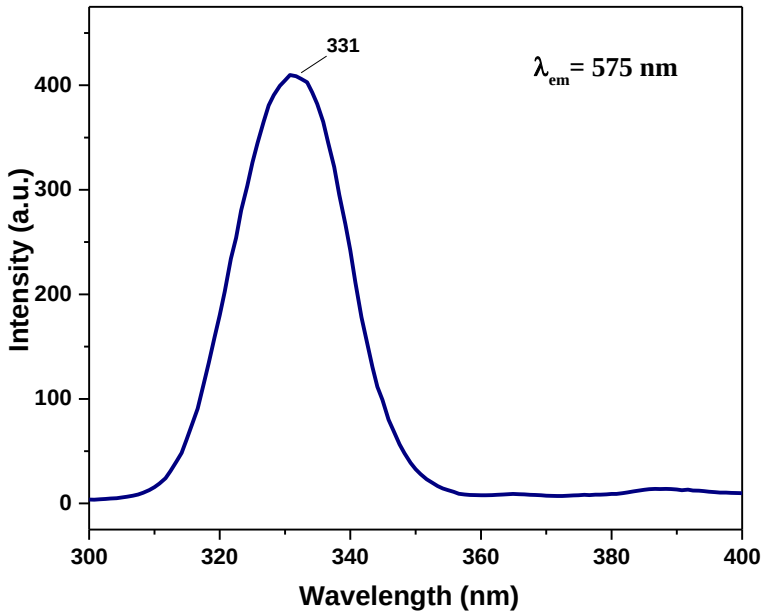

Figure 40. Excitation spectra of Dy^{3+}/ Ce^{3+} codoped $LaBO_3$ materials.

Figure 40 demonstrates PLE spectra of Dy^{3+}/ Ce^{3+} codoped $LaBO_3$ samples at 575 nm emission wavelength. A broad and intense excitation peak was centered around 331 nm. **Figure 41 and 42** are the emission spectra of different concentrations of Dy^{3+}/ Ce^{3+} codoped $LaBO_3$ phosphors at an excitation wavelength of 331 nm. The spectra show broad band centered at 437 nm which is attributed to the 5d→4f transition of Ce^{3+} ions [28]. Moreover, it contains three emission bands of Dy^{3+} ions at 485, 575 and 665 nm due to the electric transitions discussed before. In comparison with single Dy^{3+} doped samples (**Figure 37.b**), the $^4F_{9/2} \rightarrow {}^8H_{13/2}$ transition intensity of Dy^{3+} increases ten times in codoped sample (**Appendix B**).

Since unlike many other RE^{3+} ions, Ce^{3+} ions have allowed 4f-5d transitions, luminescence intensity of Dy^{3+} ion in the Ce^{3+}/ Dy^{3+} codoped $LaBO_3$ sample is increased through exciting Ce^{3+} ion (331 nm). This substantial increase in intensity also proves that there is an energy transfer from Ce^{3+} to Dy^{3+} ions. Thus, Ce^{3+} ion is an excellent sensitizer for Dy^{3+} ion in $LaBO_3$ host matrix. It is worth to note that luminescence intensity of samples can be tuned by changing both the activator and the sensitizer ion concentration.

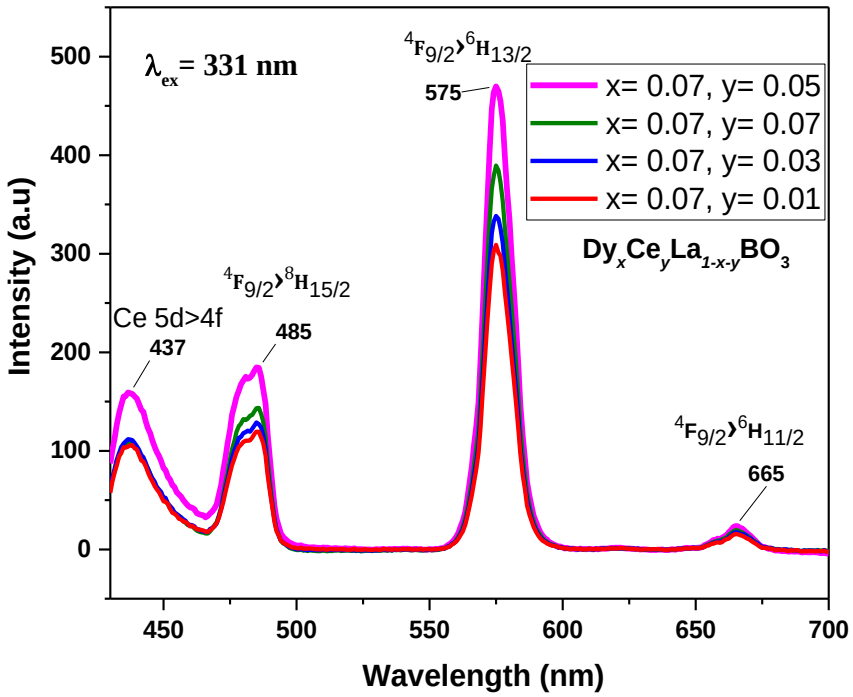

Figure 41. Emission spectra of Dy^{3+}/ Ce^{3+} codoped $LaBO_3$ materials.

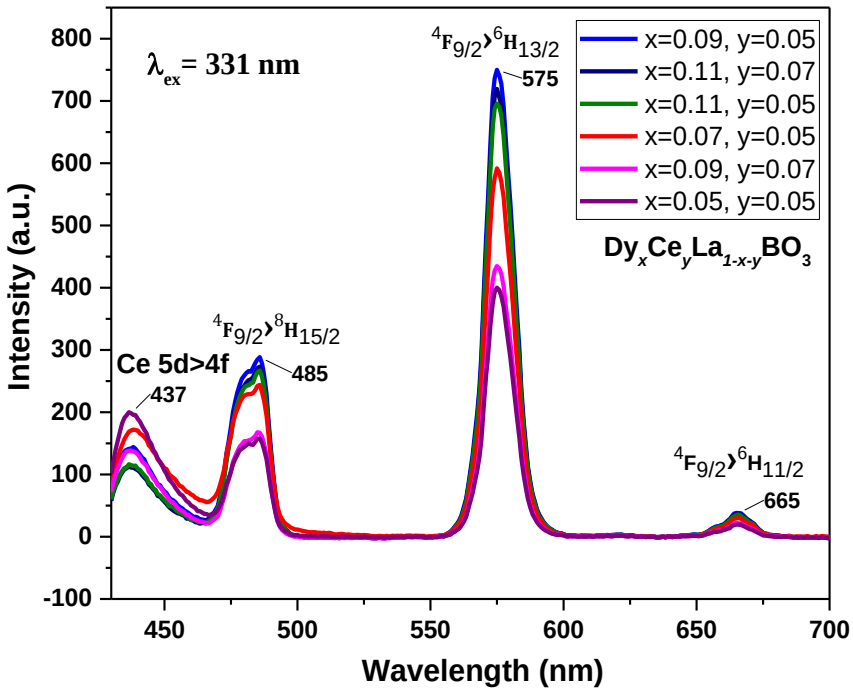

Figure 42. Emission spectra of Dy^{3+}/ Ce^{3+} codoped $LaBO_3$ materials.

PLE spectra of Eu^{3+}/ Dy^{3+} codoped samples at 575 nm and 615 nm emission wavelengths are given in **Figure 43.a-b.** Highest excitation peaks were obtained at 351 nm and 394 nm for 575 and 615 emission wavelengths, respectively. **Figure 44.a-b** exhibit emission spectra of Eu^{3+}/ Dy^{3+} codoped samples recorded with 351 nm and 394 nm excitation wavelengths, respectively**.** As Dy^{3+} single doped samples have deficiency in the red region, Eu^{3+} ions which have strong red emissions were doped along with Dy^{3+} ions to obtain white light. In addition to three emission bands of Dy^{3+} (485 nm, 575 nm and 665 nm), the weak emission centered at 615 nm due to $^5D_0 \rightarrow {}^7F_2$ electronic transition of Eu^{3+} ion was observed under 351 nm excitation [24]. Intensity of this transition is on the rise with increasing concentration of Eu^{3+} ion.

Observing the emission band of Eu^{3+} ion with exciting (351 nm) Dy^{3+} ion proves that there is an energy transfer from Dy^{3+} to Eu^{3+}**.** Additionally, emission intensity of Dy^{3+} ion decreases as concentration of Eu^{3+} ion increases. It is also a sign of the energy transfer process between Dy^{3+} and Eu^{3+} ions under 351 nm excitation [24].

On the other hand, there is no energy transfer between the ions upon exciting Eu^{3+} ions (394 nm) because intensity of characteristic bands of Eu^{3+} ions increase proportionally to their increasing concentration. Herein, emission bands of Dy^{3+} ions at 485, 575 nm decreases with the increasing concentration of Eu^{3+} ions.

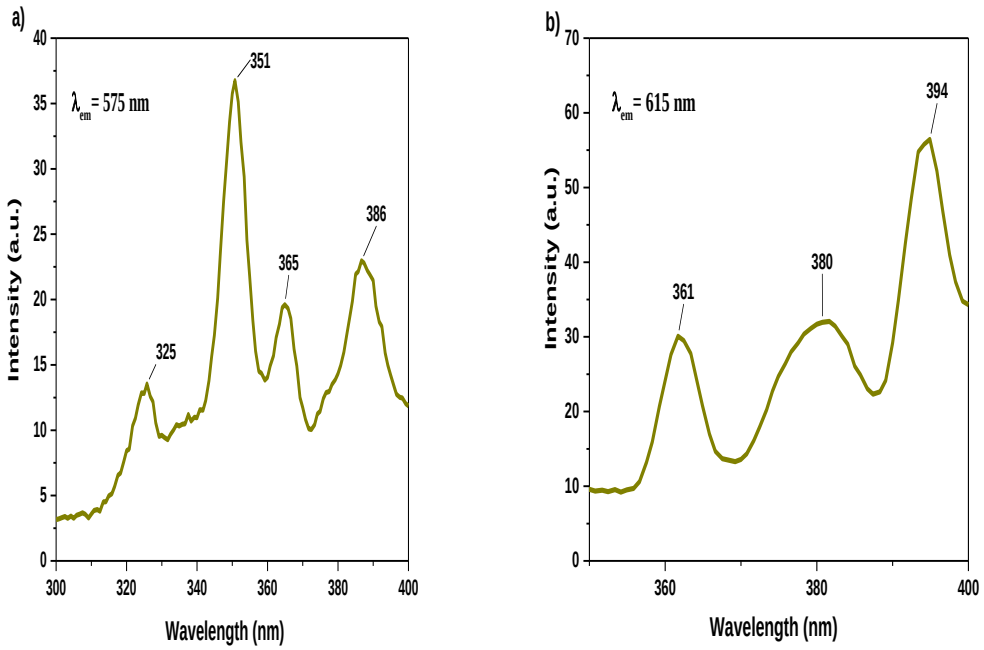

Figure 43. Excitation spectra of Dy^{3+}/ Eu^{3+} codoped $LaBO_3$ materials **a)** λ_{em} = 575 nm **b)** λ_{em} = 615 nm.

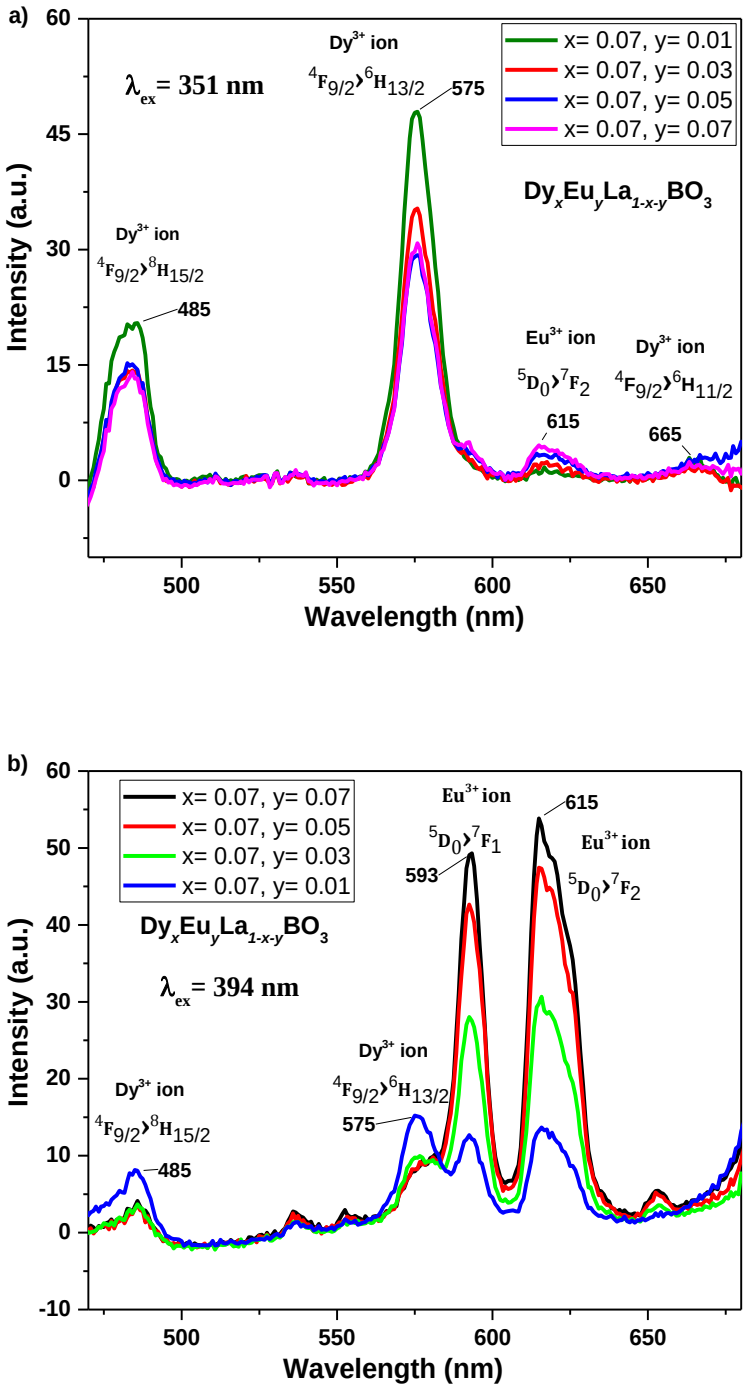

Figure 44. Emission spectra of Dy^{3+}/ Eu^{3+} codoped $LaBO_3$ materials **a)** λ_{ex} = 351 nm **b)** λ_{ex} = 394 nm.

Figure 45.a shows the PLE spectra of Tb^{3+} doped $LaBO_3$ materials at 544 nm emission wavelength. Broad excitation peaks around 352 nm and 378 nm with comparable intensities were detected. In addition, PLE spectra of Tb^{3+}/ Ce^{3+} codoped $LaBO_3$ at 544 nm emission wavelength is given in **Figure 45.b.** A broad and intense excitation peak was observed around 331 nm**. Figure 46.a-b** reveals emission spectra of Tb^{3+} doped Tb^{3+}/ Ce^{3+} codoped $LaBO_3$ phosphors monitored by the 378 nm and 331 nm excitation, respectively. The emission spectra ranging between 430 and 700 nm have four bands centered at 437, 489, 544, 586 and 622 nm. The band around 437 nm is associated with 5d $\rightarrow$ 4f transition of Ce^{3+} ions. Other bands are associated with emissions of $^5D_4 \rightarrow {}^7F_J$ (J= 6, 5, 4, 3) transitions of Tb^{3+} that are located at 489,544,586, and 622 nm, respectively. Compared to the single Tb^{3+} doped lanthanum orthoborate sample which is excited by 378 nm, emission band intensity of Tb^{3+} ion at 544 nm increases over thirteen times in Tb^{3+}/ Ce^{3+} codoped $LaBO_3$ sample (**Appendix C**). Sharpness of f-f transitions of Tb^{3+} ion in the codoped sample can be increased via exciting Ce^{3+} ion due to its allowed f-d transitions [70]. Thus, Ce^{3+} ion is excellent sensitizer for Tb^{3+} ion in $LaBO_3$ host structure.

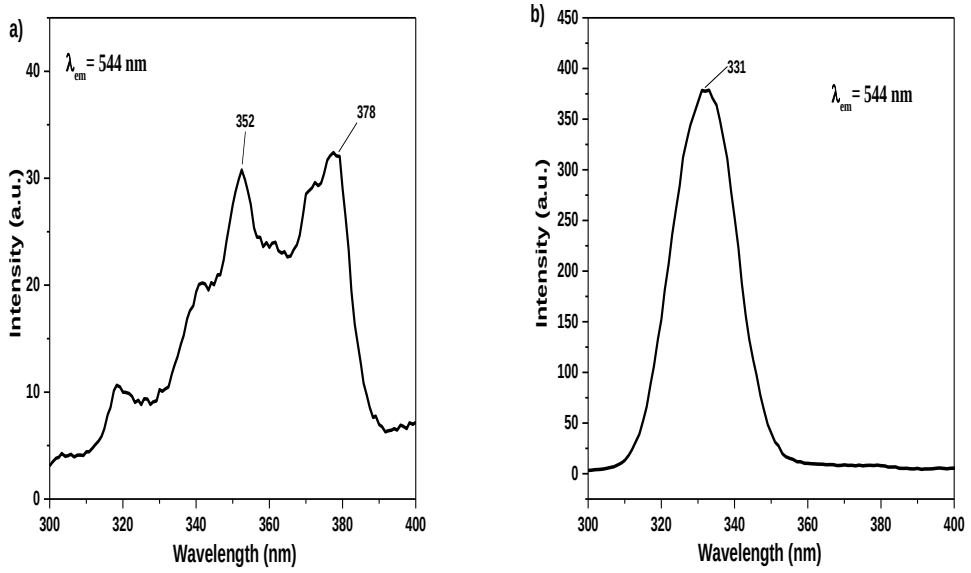

Figure 45 Excitation spectra of **a)** Tb^{3+} doped, **b)** Tb^{3+}/ Ce^{3+} codoped $LaBO_3$ materials.

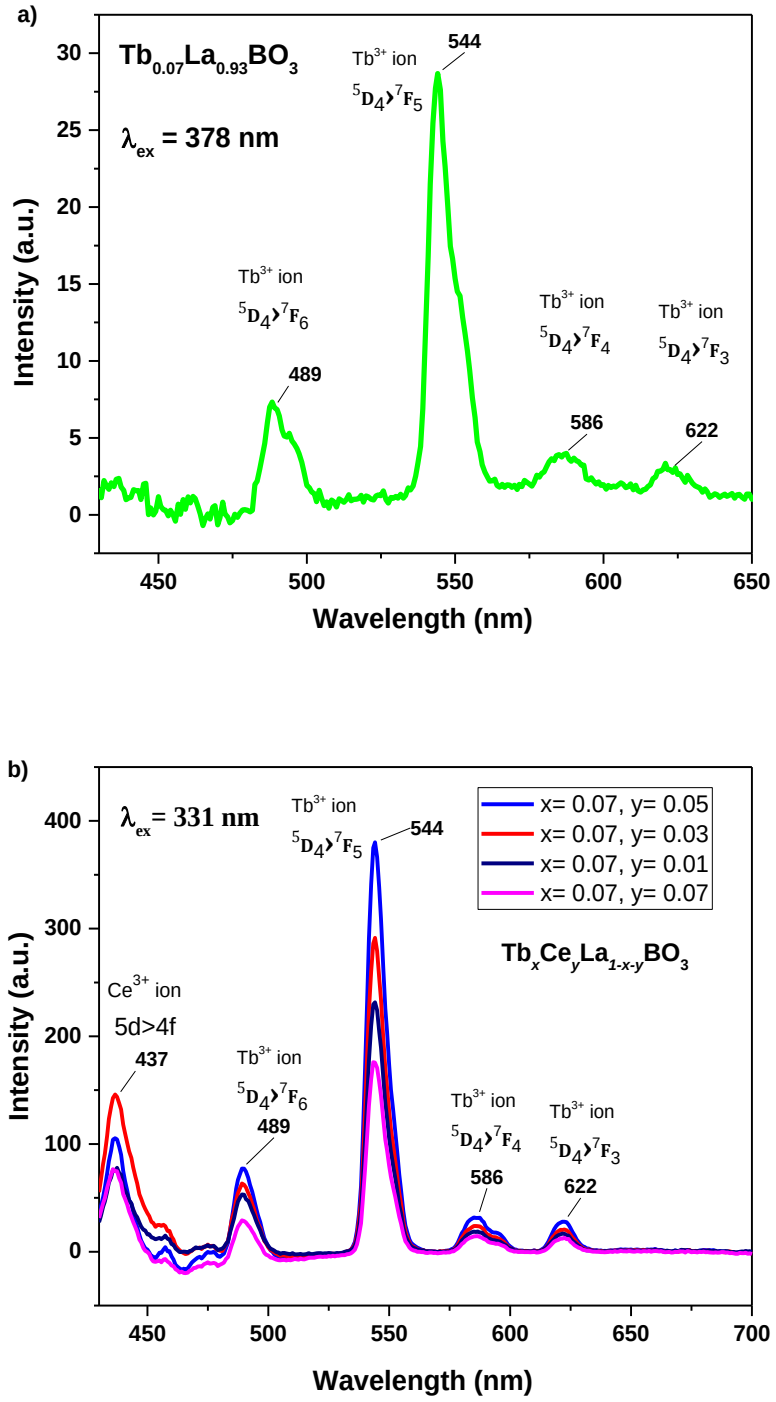

Figure 46. Emission spectra of **a)** Tb^{3+} doped (λ_{ex} = 378 nm) and **b)** Tb^{3+}/ Ce^{3+} codoped (λ_{ex} = 331 nm) $LaBO_3$ materials**.**

3.6 CIE results of doped, codoped $LaBO_3$

Figure 47-52 represent CIE 1931 color space chromaticity diagram of Dy^{3+}; Eu^{3+} doped, Dy^{3+}/ Bi^{3+}; Dy^{3+}/ Ce^{3+}; Eu^{3+}/ Dy^{3+}; Tb^{3+}/ Ce^{3+} codoped $LaBO_3$ phosphors. Moreover, photographs of phosphors taken under 355 nm excitation are shown in the insets of these figures**.** CIE coordinates of Dy^{3+} doped samples are ranging from (0.425, 0.445) to (0.427,0.450) that correspond to pale yellow color **(Figure 47)**. Colors of samples do not change so much with increasing concentration of the ion.

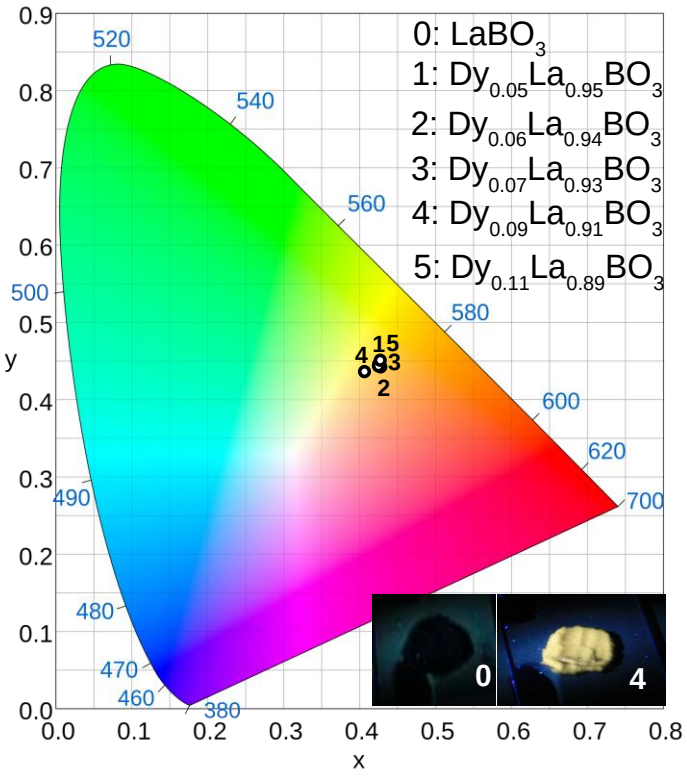

Figure 47. CIE coordinates and inset photographs of undoped, Dy^{3+} doped $LaBO_3$ materials.

CIE coordinates of Eu^{3+} doped $LaBO_3$ are calculated as (0.557, 0.355), (0.607, 0.370), (0.614, 0.372) for $Eu_{0.01}La_{0.99}BO_3$, $Eu_{0.05}La_{0.95}BO_3$, $Eu_{0.07}La_{0.93}BO_3$ phosphors, respectively, at various shades of red (**Figure 48)**. As shown in the inset, picture of phosphor (3) emission is pure red. Moreover, redness of samples increases with the increase in Eu^{3+} ion concentration.

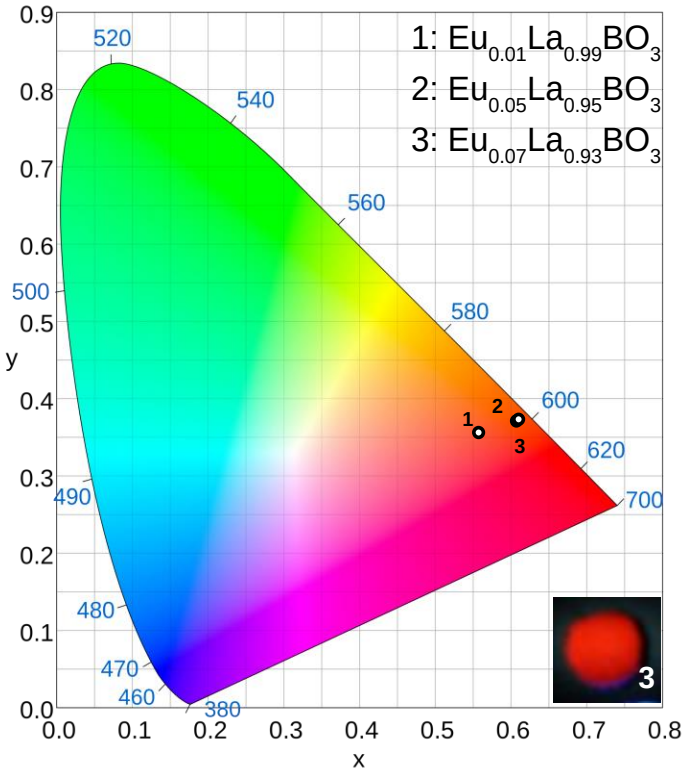

Figure 48. CIE chromaticity and inset photographs of Eu^{3+} doped $LaBO_3$ materials

CIE coordinates of Dy^{3+}/ Bi^{3+} codoped samples are (0.387, 0.430), (0.394,0.432), (0.391,0.433), (0.402, 0.415) for $Dy_{0.01}Bi_{0.01}La_{0.98}BO_3$, $Dy_{0.05}Bi_{0.01}La_{0.94}BO_3$, $Dy_{0.07}Bi_{0.01}La_{0.92}BO_3$, $Dy_{0.07}Bi_{0.05}La_{0.93}BO_3$. These coordinates correspond to pale yellow color **(Figure 49)**. Colors of samples do not change so much with increasing concentration of the activator or sensitizer ion.

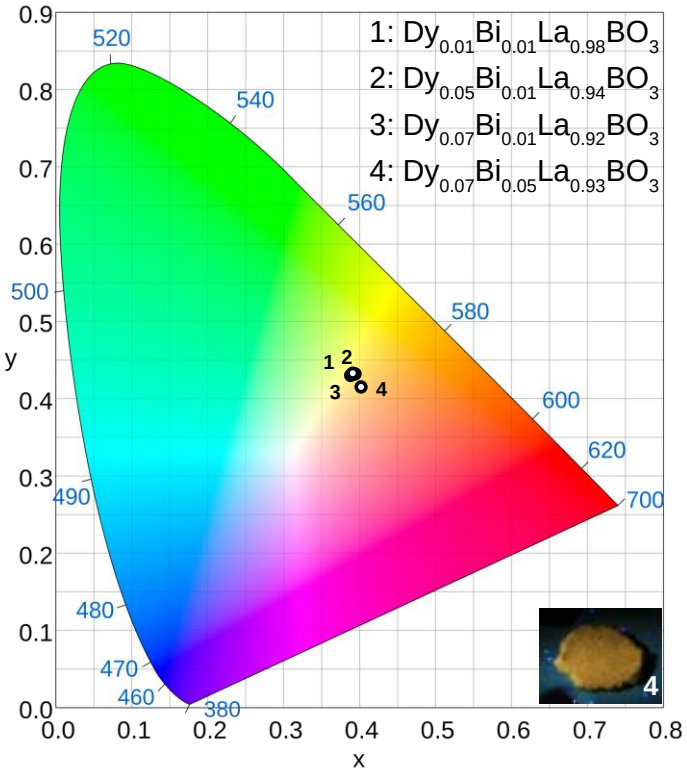

Figure 49. CIE chromaticity and inset photographs of Dy^{3+}/ Bi^{3+} codoped $LaBO_3$ materials.

On the other hand, Ce^{3+}/ Dy^{3+} codoped phosphors have whiter color under 331 nm excitation with CIE coordinates (0.280,0.235), (0.319,0.297), (0.330,0.315), (0.333,0.306), (0.363, 0.358), (0.340, 0.329) for $Dy_{0.05}Ce_{0.05}La_{0.90}BO_3$, $Dy_{0.07}Ce_{0.05}La_{0.88}BO_3$, $Dy_{0.09}Ce_{0.05}La_{0.86}BO_3$, $Dy_{0.09}Ce_{0.07}La_{0.84}BO_3$, $Dy0_{.11}Ce_{0.05}La_{0.84}BO_3$, and $Dy_{0.11}Ce_{0.07}La_{0.82}BO_3$, respectively **(Figure 50)**. According to the results, we conclude that colors of phosphor can be tuned from pale yellow to white by changing concentrations ratio of activator and sensitizer ions. Although Dy^{3+}/ Ce^{3+} codoped phosphor shows whiter color under 331 nm excitation, the inset photograph taken under 355 nm excitation has yellow color **(Inset of Figure 50)** because Dy^{3+} ion is excited by 355 nm wavelength, we observed mainly emissions of Dy^{3+} ion and its color.

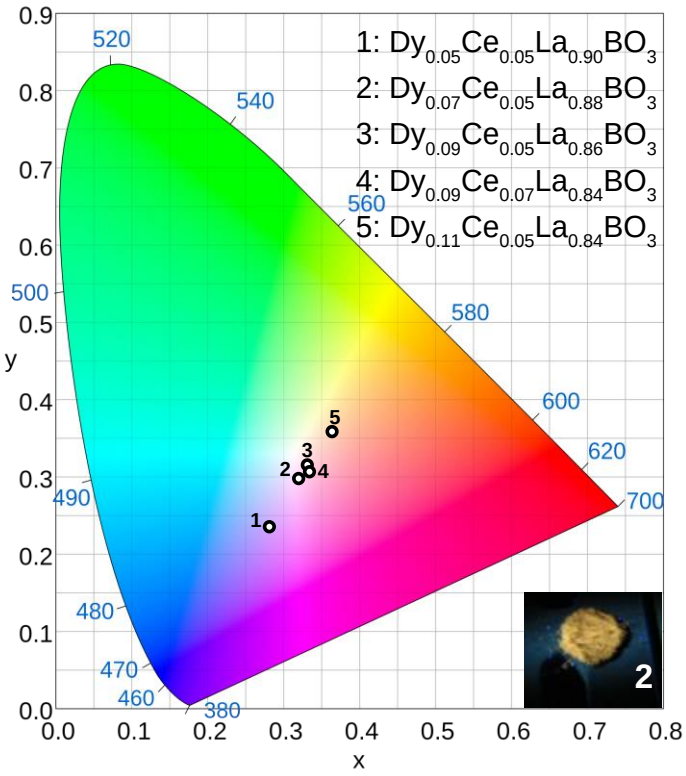

Figure 50. CIE chromaticity and inset photographs of Dy^{3+}/ Ce^{3+} codoped $LaBO_3$ materials

Calculated CIE coordinates were indicated as (0.429, 0.466), (0.464, 0.488), (0.463, 0.462), (0.483, 0.479) for $Dy_xEu_yLa_{1-x-y}BO_3$ x= 0.07, y= 0.01, 0.03, 0.05, 0.07 respectively as showed in **Figure 51.** It also confirms the tunability of color from yellowish to reddish region by changing the concentration ratio of dopant ions. As shown in inset, Photographs of Eu^{3+}/ Dy^{3+} codoped samples become reddish while concentration of Eu^{3+} ion is increased.

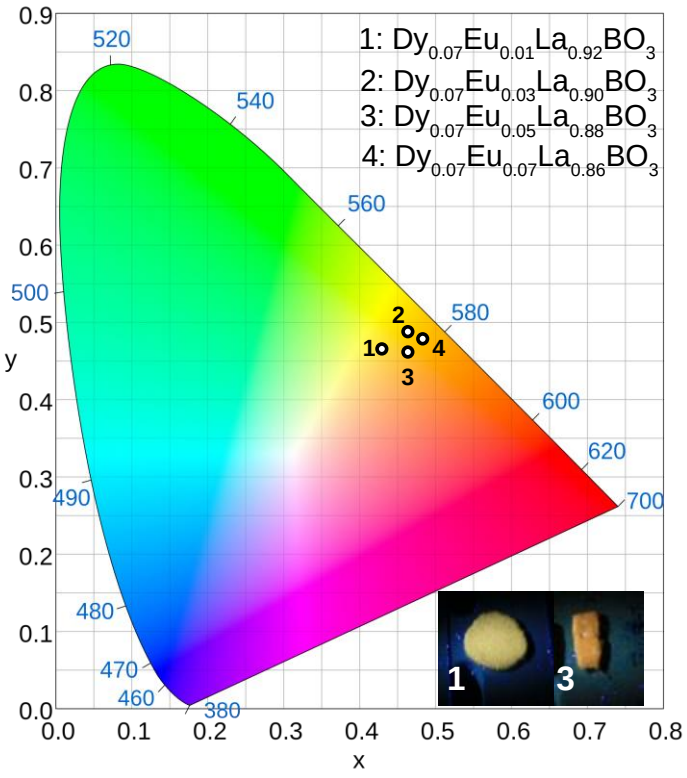

Figure 51. CIE chromaticity and inset photographs of Dy^{3+}/ Eu^{3+} codoped $LaBO_3$ materials.

CIE color coordinates of $Tb_xCe_yLa_{1-x-y}BO_3$ phosphors were calculated as (0.256, 0.437), (0.243, 0.371), (0.281, 0.514), (0.286, 0.494) for x=0.07, y=0.01, 0.03, 0.05, 0.07 concentrations respectively **(Figure 52)**. Colors of phosphors are tunable from the blue to green region by changing concentrations of dopants. It is clearly observed from inset photo of Tb^{3+}/ Ce^{3+} codoped $LaBO_3$ (3) phosphors that they emit quite strong green light.

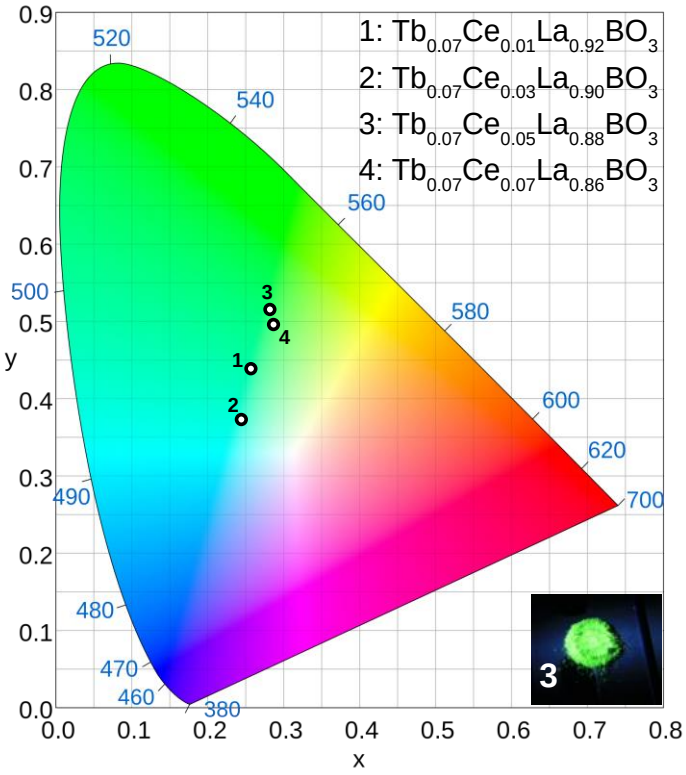

Figure 52. CIE chromaticity and inset photographs of Tb^{3+}/ Ce^{3+} codoped $LaBO_3$ materials.

3.7 Decay curves of undoped, doped, codoped $LaBO_3$

Luminescence lifetimes of samples were measured according to their highest emission bands. It would have been to selectively measure decay lifetimes of samples by exciting the RE^{3+} ions at their selected excitation wavelengths, but we had a blue-365 nm laser for excitation of phosphors only. Thus, it may have excited both the ion at interest and the codoped RE^{3+} ion and results may reflect a combination decay times when there is an overlap of emission bands. The observed decay curves of materials were generally fitted to a double exponential function. However, we have also fit the decay curves to a single exponential function and results are given in **Appendix D.** Fitting with single exponential function confirms emission of ions occupying one type of site whereas double exponential offers emission of ions occupying two sites [71].

Table 12 includes luminescence lifetimes of Dy^{3+}, Tb^{3+}, Eu^{3+} ions in different host structures reported in literature. The host material affects the luminescence lifetimes of significantly. **Table 13** presents a summary of the double exponential decay function fit parameters. The full list is given in the **Appendix D**.

Table 12. Reported decay times of Dy^{3+}, Eu^{3+}, Tb^{3+} emissions in different hosts**.**

HOST	Dy (575)	Eu (615)	Tb (544)
$LaBO_3$ [26]		1.68 ms	2.13 ms
$KCa_4(BO_3)_3$ [36]		0.46 ms	0.45 ms
$NaBaBO_3$ [72]	0.695 ms		
$Na_3Bi(PO_4)_2$ [73]			2.50- 1.00 ms
$LiSrPO_4$ [74]	0.85-0.57 ms		

Table 13. Summary of the exponential fit function parameters and their errors.

	A_1	t_1 (ms)	t_1 (ms)	A_2	t_2 (ms)	t_2 (ms)	Statistics	t_{av} (ms)
Dopant (observed wavelength)	Value	Value	Std. Error	Value	Value	Std. Error	R-Square	
CeTb(544nm)	7820.832	1.210	0.0319	15102.158	2.800	0.0262	0.9996	2.509
Dy(575nm)	25018.811	0.352	0.0218	43140.647	0.908	0.0188	0.999	0.806
DyCe(575nm)	3875.933	0.478	0.0345	2042.745	1.18	0.0917	0.993	0.875
DyEu(615nm)	602.114	0.523	0.1129	2059.871	2.090	0.0870	0.990	1.983
Tb(544)	321.813	0.316	0.0999	1091.961	2.770	0.0755	0.914	2.690
Eu(615)	8186.628	1.910	0.0575	-	-	-	-	-

Figure 53-58 presents examples of decay curves of RE^{3+} ions excited at 365 nm. **Figure 53** shows the decay curve of 7% Dy^{3+} doped $LaBO_3$ with t_{av} = 0.806 ms luminescence lifetimes (t_1= 0.352±0.0218 ms, t_2=0.907±0.0188 ms) measured at 575 nm. This curve is well fitted by double exponential function. Whereas, the decay of Eu^{3+} emissions (615 nm) of 7% Eu^{3+} doped $LaBO_3$ is fitted to single exponential function with t = 1.91 ms. (**Figure 54).** Thus, single exponential fitting offers that emission of Eu^{3+} ion occupying one site whereas double exponential fitting suggests that emission of Dy^{3+} ion occupying two sites or sites with dissimilar environment.

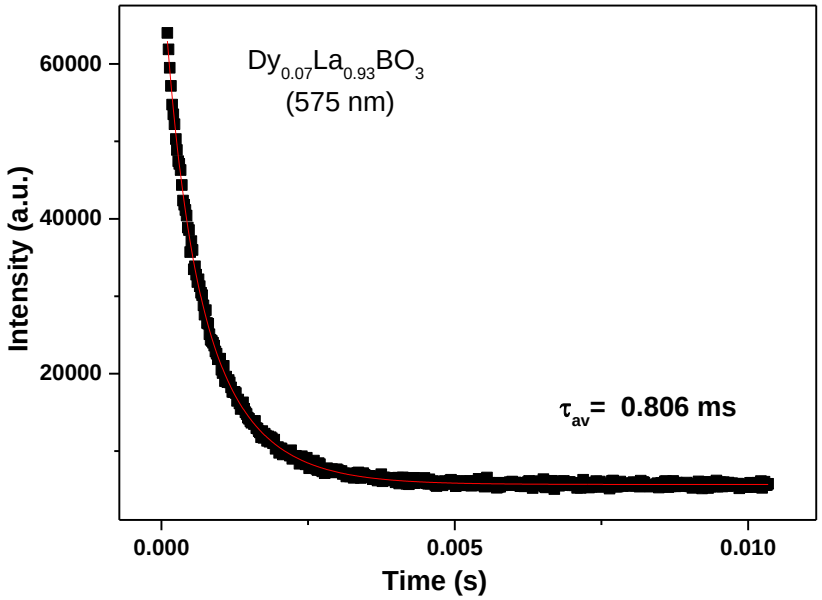

Figure 53. Decay curve of Dy^{3+} doped $LaBO_3$ materials

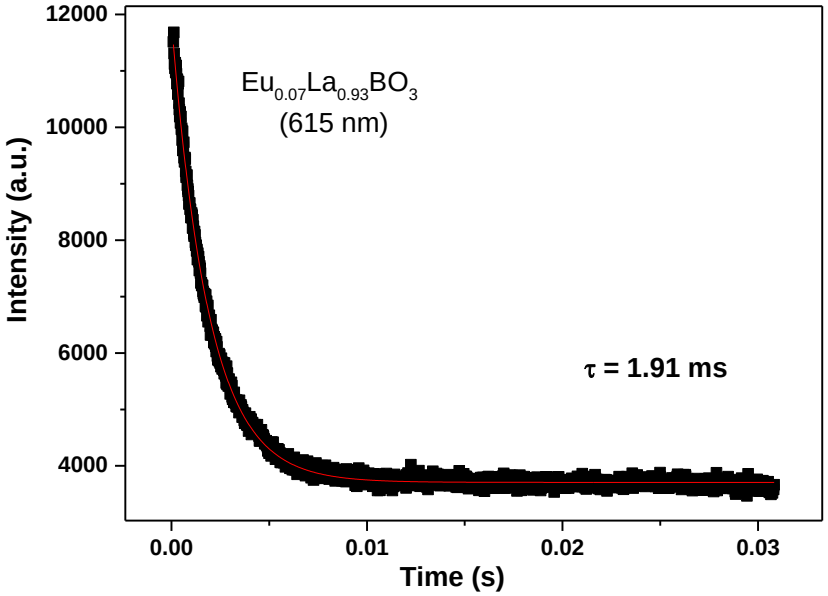

Figure 54. Decay curve of Eu^{3+} doped $LaBO_3$ materials

Similar to Dy^{3+} doped $LaBO_3$ 575 emission, decay curves of 7% Tb^{3+} doped $LaBO_3$ and other codoped samples are fitted with double exponential functions. Thus, their average luminescence lifetimes are calculated with the equation 1.4.3 by using fast and slow luminesce lifetimes. **Figure 55** exibits decay curve of 7% Tb^{3+} doped $LaBO_3$ phosphors which has 2.69 ms average luminescence lifetime with t_1= 0.316±0.099 ms, and t_2= 2.77±0.075 ms at 544 nm.

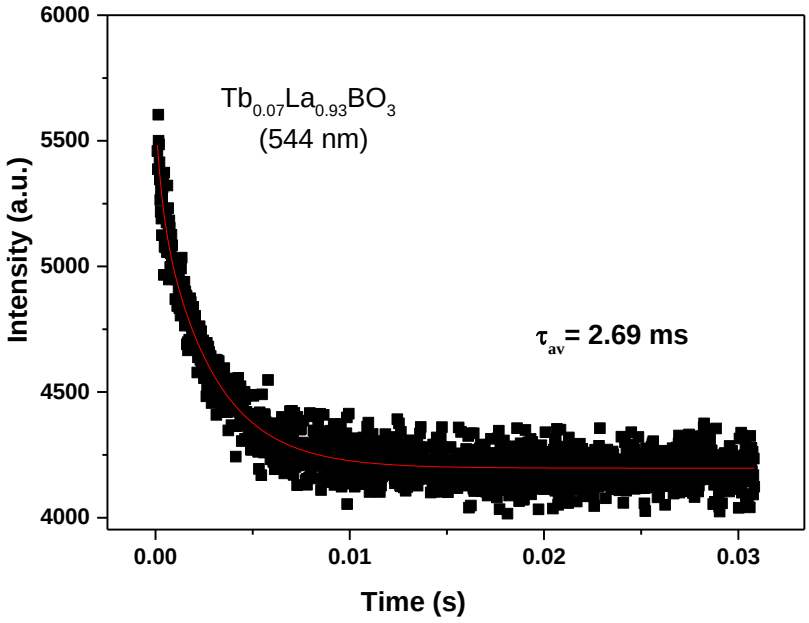

Figure 55. Decay curve of Tb^{3+} doped $LaBO_3$ materials

In **Figure 56**, decay curve of 7% Dy^{3+} and 5% Ce^{3+} codoped $LaBO_3$ samples at 575 nm is represented. The codoped phosphor has average luminescent lifetime, t_{av} = 0.875 ms with t_1= 0.478±0.0345 ms, and t_2= 1.18±0.0917 ms. Comparing to single Dy^{3+} doped sample (t_1= 0.352±0.0218 ms, t_2=0.907±0.0188 ms), increase of the lifetime of Dy^{3+} emission by codoping of Ce^{3+} ions may be a proof of the presence of slow energy transfer from Ce^{3+} to Dy^{3+} ions. This is confirming the observed strong increase in Dy^{3+} emission with Ce^{3+} codoping.

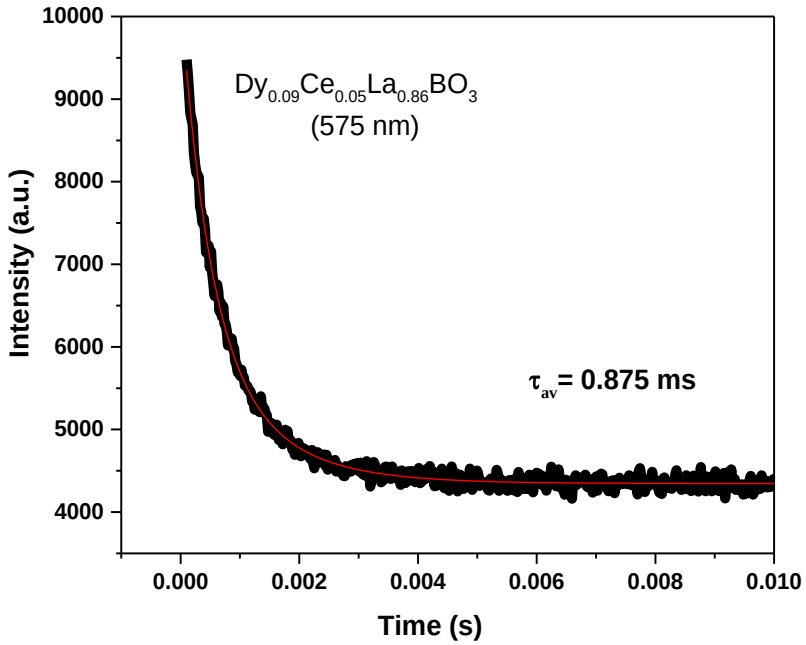

Figure 56. Decay curve of Dy^{3+} / Ce^{3+} codoped $LaBO_3$ materials

Average decay times of Eu^{3+} emission (615 nm) of 7% Dy^{3+} and 5% Eu^{3+} codoped $LaBO_3$ phosphor is recorded as 1.98 ms with t_1= 0.523±0.1129 ms, and t_2= 2.09±0.087 ms (**Figure 57**). In order to make a comparison, decay curve of Dy^{3+}/ Eu^{3+} codoped sample is well fitted with single exponential function. Decay times of the codoped sample were determined as t= 1.77±0.0198 ms. Decay time of Eu^{3+} emission decreases in the codoped sample with respect to single doped one (1.91±0.0575 ms). This suggests that there is fast energy transfer from Dy^{3+} to Eu^{3+} ions. In addition, Dy^{3+}/ Eu^{3+} codoped sample is excited with lower wavelength (365 nm higher in energy) than Eu^{3+} excitation wavelength. Thus, non- radiative energy transfers may have taken a while. On the other hand, energy is directly transferred from Dy^{3+} to Eu^{3+} ions and less non-radiative energy transfer may have led to faster decay times in codoped one.

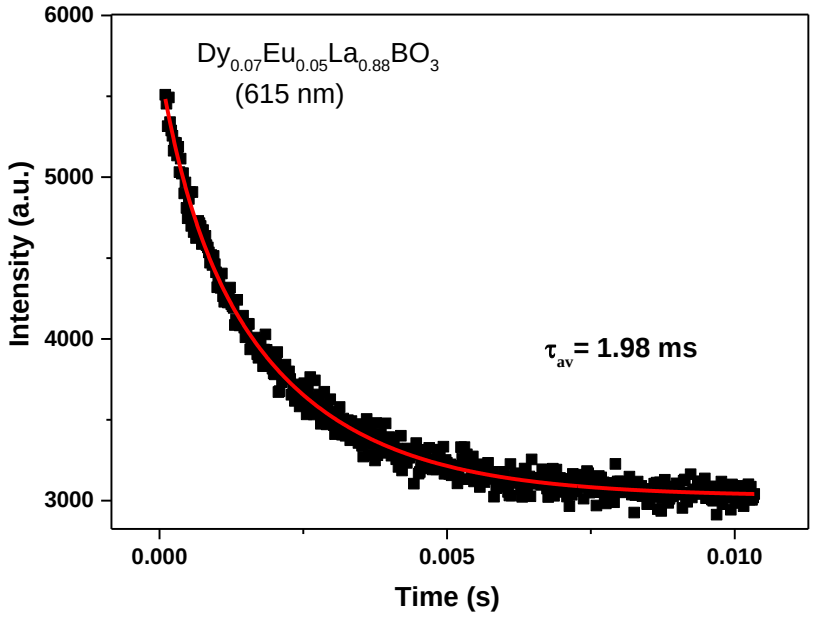

Figure 57. Decay curve of Dy^{3+} / Eu^{3+} codoped $LaBO_3$ materials

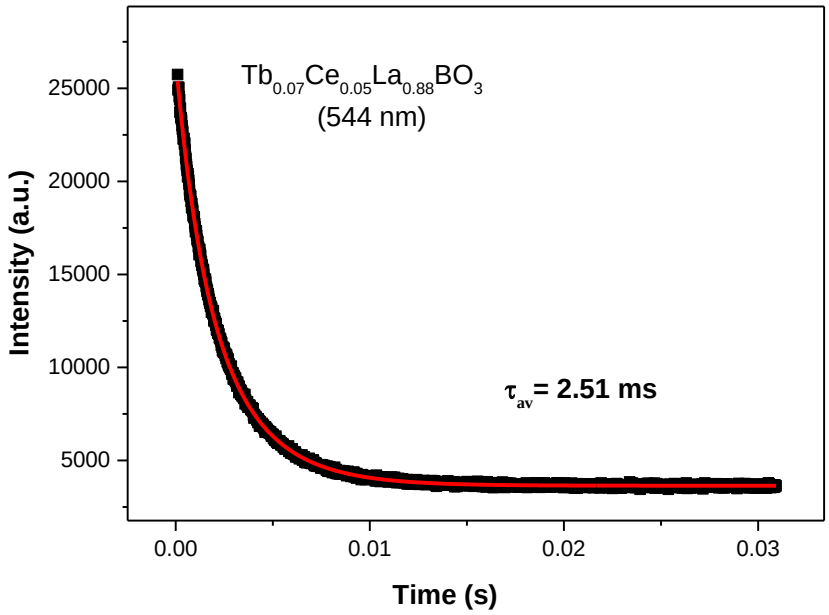

Figure 58. Decay curve of Tb^{3+} / Ce^{3+} codoped $LaBO_3$ materials

Figure 58 exhibits the decay curve of 7% Tb^{3+} and 5% Ce^{3+} codoped phosphors based at Tb^{3+} ion emission at 544 nm. The average luminescence lifetime is calculated as 2.51 ms with t_1= 1.21±0.031 ms, and t_2= 2.80±0.026 ms . Initial decay times of codoped sample is longer than the single Tb^{3+} doped $LaBO_3$ (t_1= 0.316±0.099 ms, t_2= 2.77±0.075 ms). Therefore, this increase of decay times may be the evidence for the slow energy transfer from Ce^{3+} to Tb^{3+} ions. It is worth to note that suggested possible energy transfer mechanisms based on the decay curves of samples are consistent with the photoluminescence results.

CHAPTER 4

CONCLUSION

XRD patterns of samples proves that $LaBO_3$ crystals are successfully synthesized by employing microwave assisted solid state synthesis method. Even though, Ce^{3+} including samples suggest the $CeBO_3$ in their XRD patterns, no significant changes are observed other recorded patterns. Recorded diffraction peaks of all undoped, Eu^{3+}, Dy^{3+} doped and Dy^{3+}/ Bi^{3+}; Dy^{3+} /Ce^{3+}; Dy^{3+}/ Eu^{3+}; Tb^{3+} /Ce^{3+} codoped $LaBO_3$ powders match well with the JCPDS card number 12-0762. The $LaBO_3$ powder crystals have the Pnma space group and orthorhombic crystal structure with the a= 5.87 Å, b=5.10 Å, and c= 8.25 Å unit cell parameters.

Planar borate (BO_3^{3-}) groups of $LaBO_3$ structure have been confirmed by observing their four main vibrational modes, ν1 (symmetric stretching) was detected at 940 cm^{-1}, ν2 (out of plane bending band) around 708 cm^{-1}, ν3 (asymmetric stretching) at 1245 cm^{-1}, and ν4 (in-plane bending) modes at 591 and 611 cm^{-1}. Some new bands at 1074, 916, 868, 668 cm^{-1} were observed for Dy^{3+} doped, Dy^{3+}/ Ce^{3+}; Dy^{3+}/ Eu^{3+}; Tb^{3+}/ Ce^{3+} codoped $LaBO_3$ phosphors.

Low frequency vibrational modes of RE^{3+} doped and codoped samples are provided by Far-Ir studies. In addition, Far-Ir spectra of oxides and boric acid were collected due to lack of information in the low frequency region. Based on the recorded spectra, we can suggest that La-O vibrational modes in La-O-B network were detected with very broad bands centered at 175 and 136 cm^{-1}. Some new bands were observed with increasing doping amounts of RE^{3+}. Thus, it suggests that doping might be both interstitial and substitutional in $LaBO_3$ and higher doping amounts leads observation of new bands.

Emissions of doped and codoped RE^{3+} ions were observed due to the transitions of Dy^{3+}: $^4F_{9/2} \rightarrow {}^8H_{15/2}$, $^4F_{9/2} \rightarrow {}^6H_{13/2}$, $^4F_{9/2} \rightarrow {}^6H_{11/2}$, Eu^{3+}: $^5D_0 \rightarrow {}^7F_2$, $^5D_0 \rightarrow {}^7F_1$, Tb^{3+}: $^5D_4 \rightarrow {}^7F_J$ (J= 6, 5, 4, 3), and Ce^{3+}: 5d $\rightarrow$ 4f. Since $^4F_{9/2} \rightarrow {}^6H_{13/2}$ (Y) emission is higher than $^4F_{9/2} \rightarrow {}^8H_{15/2}$ (B), it can be concluded that Dy^{3+} ions prefer low symmetry sites in all Dy^{3+} containing samples. Moreover, Y/B intensity ratio does not vary with the change in Dy^{3+} concentration because of the similar radii of host and dopant ions.

When luminescence properties of phosphors are compared, Dy^{3+} / Ce^{3+} and Tb^{3+} / Ce^{3+} codoped $LaBO_3$ samples have the highest luminescence intensities. In fact, compared to single Dy^{3+} doped $LaBO_3$ phosphors, emission band intensity of Dy^{3+} at 575 nm increases by nearly ten times in Dy^{3+} / Ce^{3+} codoped samples. In addition, emission band intensity of Tb^{3+} ion at 544 nm increases over thirteen times in Tb^{3+} / Ce^{3+} codoped $LaBO_3$ phosphor with respect to single Tb^{3+} doped $LaBO_3$ samples. Highest luminescence intensities were observed for $Dy_{0.09}Ce_{0.05}La_{0.86}BO_3$ and $Tb_{0.07}Ce_{0.05}La_{0.88}BO_3$ materials.

SEM images proves that all synthesized $LaBO_3$ samples have fine particle size and regular morphology. When size of materials is compared, codoped ones are relatively smaller than undoped and single Dy^{3+} doped $LaBO_3$.

The CIE coordinates calculations represent that Dy^{3+} doped and Dy^{3+}/ Bi^{3+} codoped samples have pale yellow color, and Eu^{3+} doped samples have red color. Moreover, different doping concentrations do not change the color of emitted light in those samples. On the other hand, color can be tuned by changing doping concentrations in Dy^{3+}/ Ce^{3+}; Tb^{3+}/ Ce^{3+}; Dy^{3+}/ Eu^{3+} codoped phosphors which emit white, green, yellow-orange light, respectively. The photographs of samples are consistent with the calculated color coordinates of them.

Luminescence decay times of samples were recorded to explain energy transfers between the RE^{3+} ions. Single and double exponential behaviors were observed according to materials. Fast energy transfers were detected from Dy^{3+} to Eu^{3+} ion and slow energy transfers were observed for the emissions where energy transfers occur from Ce^{3+} to Dy^{3+} and Ce^{3+} to Tb^{3+} ions. It can be also suggested that single

Tb^{3+} doped and Tb^{3+}/ Ce^{3+} codoped samples have the highest luminescence decay times among the synthesized phosphors.

REFERENCES

[1] D. Bera, L. Qian, and P. H. Holloway, *2 Phosphor Quantum Dots*. 2008.

[2] M. Lastusaari, T. Laamanen, M. Malkamäki, K. O. Eskola, A. Kotlov, S. Carlson, E. Welter, H. F. Brito, M. Bettinelli, H. Jungner, and J. Hölsä, "The Bologna Stone: history's first persistent luminescent material," *Eur. J. Mineral.*, vol. 24, no. 5, pp. 885–890, 2012.

[3] and H. Y. William M. Yen, Shigeo Shionoya, *Phosphor Handbook*, vol. 23, no. 1. 2007.

[4] M. Shang, C. Li, and J. Lin, "How to produce white light in a single-phase host?," *Chem. Soc. Rev.*, vol. 43, no. 5, pp. 1372–86, 2014.

[5] A. Mnoyan, Y. Lee, H. Jung, and S. Kim, *Phosphors, Up Conversion Nano Particles, Quantum Dots and Their Applications*, vol. 1. 2016.

[6] W. M. Yen, S. Shionoya, and H. Yamamoto, *Practical Applications of Phosphors*. 2007.

[7] Jablonski A., "Efficiency of Anti-Stokes Fluorescence in Dyes," *Nature*, vol. 131, no. 3319, pp. 839–840, 1933.

[8] J. Hofkens, J. Enderlein, M. Sauer, J. Hofkens, and J. Enderlein, "Basic Principles of Fluorescence Spectroscopy," *Handb. Fluoresc. Spectrosc. Imaging From Single Mol. to Ensembles*, pp. 1–30, 2011.

[9] B. Valeur and M. N. Berberan-Santos, "A brief history of fluorescence and phosphorescence before the emergence of quantum theory," *J. Chem. Educ.*, vol. 88, no. 6, pp. 731–738, 2011.

[10] G. G. Stokes, "On the Change of Refrangibility of Light. No. II," *Philos. Trans. R. Soc. London*, vol. 143, no. 0, pp. 385–396, 1853.

[11] K. Mariselvam and R. A. Kumar, "Borate Glasses for Luminescence Applications – Potential Materials for White LEDs and Laser Sources," vol. 4, no. 2. Universal Journal of Chemistry, India, pp. 55–64, 2016.

[12] S. Özkar and N. K. Tunalı, *Anorganik Kimya*. OzBaran Ofset, 2009.

[13] H. G. Dieke, *Spectra and energy levels of rare earth ions in crystals*. John Wiley & Sons, 1968.

[14] C. G. Ma, M. G. Brik, D. X. Liu, B. Feng, Y. Tian, and A. Suchocki, "Energy level schemes of fN electronic configurations for the di-, tri-, and tetravalent lanthanides and actinides in a free state," *J. Lumin.*, vol. 170, no. February, pp. 369–374, 2016.

[15] K. N. Shinde, S. J. Dhoble, H. C. Swart, and K. Park, *Phosphate Phosphors*

for Solid-State Lighting, vol. 174. 2012.

[16] M. Vijayakumar, K. Mahesvaran, D. K. Patel, S. Arunkumar, and K. Marimuthu, "Structural and optical properties of Dy^{3+} doped Aluminofluoroborophosphate glasses for white light applications," *Opt. Mater. (Amst).*, vol. 37, pp. 695–705, 2014.

[17] R. Hussin, S. Hamdan, D. N. F. A. Halim, and M. S. Husin, "The origin of emission in strontium magnesium pyrophosphate doped with Dy_2O_3," *Mater. Chem. Phys.*, vol. 121, no. 1–2, pp. 37–41, 2010.

[18] S. Chemingui, M. Ferhi, K. Horchani-Naifer, and M. Férid, "Synthesis and luminescence characteristics of Dy^{3+} doped $KLa(PO_3)_4$," *J. Lumin.*, vol. 166, pp. 82–87, 2015.

[19] P. P. Pawar, S. R. Munishwar, and R. S. Gedam, "Intense white light luminescent Dy^{3+} doped lithium borate glasses for W-LED: A correlation between physical, thermal, structural and optical properties," *Solid State Sci.*, vol. 64, no. January 2017, pp. 41–50, 2017.

[20] N. Wazir, V. Kumar, J. Sharma, O. M. Ntwaeaborwa, and H.C. Swart, "Synthesis and photoluminescence study of a single dopant near white light emitting $Li_4CaB_2O_6$: Dy^{3+} nanophosphor," *J. Alloys Compd.*, vol. press, pp. 4–10, 2016.

[21] L. Y. Zhou, J. S. Wei, J. X. Shi, M. L. Gong, and H. Bin Liang, "A novel green phosphor $GdCaAlO_4$:Tb^{3+} for PDP application," *J. Lumin.*, vol. 128, no. 8, pp. 1262–1266, 2008.

[22] A. Potdevin, G. Chadeyron, D. Boyer, B. Caillier, and R. Mahiou, "Sol–gel based YAG : Tb^{3+} or Eu^{3+} phosphors for application in lighting sources," *J. Phys. D. Appl. Phys.*, vol. 38, no. October 2016, pp. 3251–3260, 2005.

[23] J. Zmojda, M. Kochanowicz, P. Miluski, and D. Dorosz, "Side-Detecting Optical Fiber Doped with Tb^{3+} for Ultraviolet Sensor Application," *Fibers*, vol. 2, no. 2, pp. 150–157, 2014.

[24] V. kumar M., "Tailoring the luminescence of Eu^{3+} codoped Dy^{3+} incorporated Aluminofluoro-borophosphate glasses for White light applications." Journal of Luminescence, 2016.

[25] H. M. Yang, J. X. Shi, and M. L. Gong, "A novel red emitting phosphor Ca_2SnO_4: Eu^{3+}," *J. Solid State Chem.*, vol. 178, no. 3, pp. 917–920, 2005.

[26] G. Jia, C. Zhang, C. Wang, L. Liu, C. Huang, and S. Ding, "Uniform and well-dispersed $LaBO_3$ hierarchical architectures: synthesis, formation, and luminescence properties," *CrystEngComm*, vol. 14, no. 2, pp. 579–584, 2012.

[27] S. K. Sharma, S. Som, R. Jain, and A. K. Kunti, "Spectral and CIE parameters of red emitting $Gd_3Ga_5O_{12}$:Eu^{3+} phosphor," *J. Lumin.*, vol. 159, pp. 317–324, 2015.

[28] C. H. Yang, Y. X. Pan, and Q. Y. Zhang, “Enhanced white light emission from Dy^{3+}/Ce^{3+} codoped $GdAl_3(BO_3)_4$ phosphors by combustion synthesis,” *Mater. Sci. Eng. B Solid-State Mater. Adv. Technol.*, vol. 137, no. 1–3, pp. 195–199, 2007.

[29] J. Wu, H. Zhang, and S. Du, “Tunable luminescence and white light emission of mixed lanthanide–organic frameworks based on polycarboxylate ligands,” *J. Mater. Chem. C*, vol. 4, no. 16, pp. 3364–3374, 2016.

[30] A. Kawski, “Zwischenmolekulare Energiewanderung und Konzentrationsdepolarisation der Fluoreszenz,” *Ann. Phys.*, vol. 463, no. 1–2, pp. 116–119, 1961.

[31] D. L. Dexter, “A Theory of Sensitized Luminescence in Solids,” *J. Chem. Phys.*, vol. 21, no. 5, pp. 836–850, 1953.

[32] J. wu, L. Zhang, Y. Ben, H. Chen, X. Fu, and C. Wong, “Improved full-color emission and switched luminescence in single $Ca_3(PO_4)_2$: Dy^{3+}, Eu^{3+} phosphors for white LEDs,” *J. Alloys Compd.*, vol. 3, no. 2017, 2016.

[33] J. Zhao, C. Guo, and T. Li, “Enhanced near-infrared emission by co-doping Ce^{3+} in $Ba_2Y(BO_3)_2Cl:Tb^{3+}$, Yb^{3+} phosphor,” *RSC Adv.*, vol. 5, no. 36, pp. 28299–28304, 2015.

[34] A. Shyichuk, “Synthesis , physicochemical characterization and computational studies of selected lanthanide-doped luminophores,” 2015.

[35] W. Zhang, S. Liu, Z. Hu, Y. Liang, Z. Feng, and X. Sheng, “Preparation of $YBO_3:Dy^{3+},Bi^{3+}$ phosphors and enhanced photoluminescence,” *Mater. Sci. Eng. B Solid-State Mater. Adv. Technol.*, vol. 187, pp. 108–112, 2014.

[36] A. A. Reddy, S. Das, A. Goel, R. Sen, R. Siegel, L. Mafra, G. V. Prakash, and J. M. F. Ferreira, “$KCa_4(BO_3)_3:Ln^{3+}$ (Ln = Dy, Eu, Tb) phosphors for near UV excited white–light–emitting diodes,” *AIP Adv.*, vol. 3, no. 2, p. 22126, 2013.

[37] K. Ambast, K. Kunti, S. Som, and S. K. Sharma, “Near-white-emitting phosphors based on tungstate for phosphor-converted light-emitting diodes,” *Appl. Opt.*, vol. 52, no. 35, p. 8424, 2013.

[38] Q. F. Lu, J. Li, and D. J. Wang, “Single-phased silicate-hosted phosphor with 660 nm-featured band emission for biological light-emitting diodes,” *Curr. Appl. Phys.*, vol. 13, no. 7, pp. 1506–1511, 2013.

[39] Q. Ren, B. Wang, X. Wu, T. Wei, and Z. Huo, “Luminescence properties and energy transfer in Dy^{3+} and Eu^{3+} co-doped $Sr_3Y(PO_4)_3$ phosphor,” *J. Alloys Compd.*, vol. 684, pp. 677–682, 2016.

[40] Z. Yang, T. Li, P. Li, Z. Wang, S. Xu, Q. Bai, and H. Dong, “Synthesis and luminescence properties of novel white emitting phosphor $KMgLa(PO_4)_2:Dy^{3+}$,” *J. Lumin.*, vol. 178, pp. 178–182, 2016.

[41] L. Han, Y. Sun, and J. Sun, “Synthesis and luminescence properties of white-light-emitting phosphor $Sr_3GdNa(PO_4)_3F:Dy^{3+}$,” *J. Rare Earths*, vol. 34, no. 1, pp. 12–16, 2016.

[42] Y. Deng, S. Yi, J. Huang, J. Xian, and W. Zhao, “White light emission and energy transfer in Dy^{3+}/Eu^{3+} co-doped BaLa2WO7 phosphors,” *Mater. Res. Bull.*, vol. 57, pp. 85–90, 2014.

[43] R. B. Kistler and C. Helvaci, “Boron and Borates,” *Ind. Miner. Rocks*, pp. 171–186, 1994.

[44] Eti Maden, “Bor Sektörü raporu,” 2016.

[45] S. Barth, “Boron Isotope Application for Tracing Sources of Contamination in Groundwater,” *Water Res.*, vol. 32, no. 3, pp. 685–690, 1998.

[46] T. Grzyb, K. Kubasiewicz, A. Szczeszak, and S. Lis, “Synthesis and spectroscopic properties of Yb^{3+} and Tb^{3+} co-doped $GdBO_3$ materials showing down- and up-conversion luminescence,” *Dalt. Trans.*, vol. 44, no. 9, pp. 4063–4069, 2015.

[47] R. Velchuri, B. V. Kumar, V. R. Devi, G. Prasad, D. J. Prakash, and M. Vithal, “Preparation and characterization of rare earth orthoborates, LnBO 3 (Ln = Tb, La, Pr, Nd, Sm, Eu, Gd, Dy, Y) and LaBO3:Gd, Tb, Eu by metathesis reaction: ESR of LaBO3:Gd and luminescence of LaBO3:Tb, Eu,” *Mater. Res. Bull.*, vol. 46, no. 8, pp. 1219–1226, 2011.

[48] M. Xin, D. Tu, H. Zhu, W. Luo, Z. Liu, P. Huang, R. Li, Y. Cao, and X. Chen, “Single-composition white-emitting $NaSrBO_3:Ce^{3+}$,Sm^{3+} ,Tb^{3+} phosphors for NUV light-emitting diodes,” *J. Mater. Chem. C*, vol. 3, no. 28, pp. 7286–7293, 2015.

[49] R. Arun Kumar and R. Dhanasekaran, “Growth and characterization of LCOB and NdLCOB single crystals for laser applications,” *J. Cryst. Growth*, vol. 318, no. 1, pp. 636–641, 2011.

[50] R. S. R. and J. B. M. Ernest M. Levin, “Polymorphism of ABO3 type rare earth borates,” *Am. Mineral.*, vol. 46, no. 1954, pp. 1030–1055, 1961.

[51] H. Giesber, J. Ballato, G. Chumanov, J. Kolis, and M. Dejneka, “Spectroscopic properties of Er^{3+} and Eu^{3+} doped acentric $LaBO_3$ and $GdBO_3$,” *J. Appl. Phys.*, vol. 93, no. 11, pp. 8987–8994, 2003.

[52] A. Pitscheider, R. Kaindl, O. Oeckler, and H. Huppertz, “The crystal structure of $ErBO_3$: New single-crystal data for an old problem,” *J. Solid State Chem.*, vol. 184, no. 1, pp. 149–153, 2011.

[53] S. Seyyidoğlu, “Synthesis and Characterization of Novel Rare Earth Phosphates and Rietveld Structural Analysis of Rare Earth Orthoborates,” no. September, p. 209, 2009.

[54] S. Lemanceau, “Synthesis and Characterization of H-$LnBO_3$ Orthoborates (Ln=La, Nd, Sm, and Eu),” *J. Solid State Chem.*, vol. 148, pp. 229–235, 1999.

[55] A. S. Kipcak, N. Acarali, F. T. Senberber, M. Yildirim, S. N. T. Koc, S. A. Yuksel, M. B. Piskin, E. M. Derun, and N. Tugrul, "Synthesis of dehydrated zinc borates using the solid-state method: Characterization and investigation of the physical properties," *Main Gr. Chem.*, vol. 15, no. 4, pp. 301–313,2016.

[56] C. Heyward, C. D. McMillen, and J. Kolis, "Hydrothermal synthesis and structural analysis of new mixed oxyanion borates: $Ba_{11}B_{26}O_{44}(PO_4)_2(OH)_6$, $Li_9BaB_{15}O_{27}(CO_3)$ and $Ba_3Si_2B_6O_{16}$," *J. Solid State Chem.*, vol. 203, pp. 166–173, 2013.

[57] C. Badan, O. Esenturk, and A. Yilmaz, "Microwave-assisted synthesis of Eu^{3+} doped lanthanum orthoborates, their characterizations and luminescent properties," *Solid State Sci.*, vol. 14, no. 11–12, pp. 1710–1716, 2012.

[58] A. Szysiak, L. Lipińska, W. Ryba-Romanowski, P. Solarz, R. Diduszko, and A. Pajaczkowska, "Nanopowders of $YAl_3(BO_3)_4$ doped by Nd, Yb and Cr obtained by sol-gel method: Synthesis, structure and luminescence properties," *Mater. Res. Bull.*, vol. 44, no. 12, pp. 2228–2232, 2009.

[59] T. Grzyb and S. Lis, "Structural and Spectroscopic Properties of LaOF : Eu^{3+} Nanocrystals Prepared by the Sol À Gel Pechini Method," pp. 8112–8120, 2011.

[60] D. Boyer, G. Bertrand-Chadeyron, R. Mahiou, A. Brioude, and J. Mugnier, "Synthesis and characterization of sol–gel derived Y_3BO_6:Eu^{3+} powders and films," *Opt. Mater. (Amst).*, vol. 24, no. 1–2, pp. 35–41, 2003.

[61] A. Kopp Alves, C. P. Bergmann, and F. A. Berutti, "Novel Synthesis and Characterization of Nanostructured Materials," 2013.

[62] L. Wang, L. Shi, N. Liao, H. Jia, P. Du, Z. Xi, L. Wang, and D. Jin, "Photoluminescence properties of Y_2O_3:Tb^{3+} and YBO_3:Tb^{3+} green phosphors synthesized by hydrothermal method," *Mater. Chem. Phys.*, vol. 119, no. 3, pp. 490–494, 2010.

[63] M. Nüchter, B. Ondruschka, W. Bonrath, and A. Gum, "Microwave assisted synthesis a critical technology overview," *Green Chem.*, vol. 6, no. 3, pp. 128–141, 2004.

[64] B. L. Hayes, "Recent Advances in Microwave Assisted Synthesis," *Aldrichimica Acta*, vol. 37, no. 2, pp. 66–76, 2004.

[65] E. A. M. Lesley E. Smart, *Solid State Chemistry An Introduction*. 2012.

[66] C. Badan, "Microwave Assisted Synthesis of Rare Earth Ions Doped Lanthanum Orthoborate, Their Characterizations and Investigations of Luminescence Properties," p. 58, 2012.

[67] "Encyclopædia Britannica, 'rare-earth element,.'" [Online]. Available: http://global.britannica.com/science/rare-earth-element. [Accessed: 04-Jul-2017].

[68] R. D. Shannon and A. Crystallogr, *Handbook of Chemistry and Physics*. 1974.

[69] M. Severoğlu, “microwave assisted solid state synthesis of rare earth ions doped $LaBO_3$, YBO_3 and $GdBO_3$, their characterizations and investigations of luminiscence properties,” 2016.

[70] F. Wang, H. Song, G. Pan, L. Fan, B. Dong, L. Liu, X. Bai, R. Qin, X. Ren, Z. Zheng, and S. Lu, “Luminescence properties of $Ce^{3+}$and Tb^{3+} ions codoped strontium borate phosphate phosphors,” *J. Lumin.*, vol. 128, no. 12, pp. 2013–2018, 2008.

[71] A. Szczeszak, K. Kubasiewicz, and S. Lis, “Photophysical characterization of $La_{1-x}Eu_xBO_3$ and $La_{1-x}Tb_xBO_3$ nanopowders synthesized by sol–gel Pechini method,” *Opt. Mater. (Amst).*, vol. 35, no. 6, pp. 1297–1303, 2013.

[72] J. Zheng, Q. Cheng, J. Wu, X. Cui, R. Chen, W. Chen, and C. Chen, “A novel single-phase white phosphor NaBaBO:Dy^{3+},K^+ for near-UV white light-emitting diodes,” *Mater. Res. Bull.*, vol. 73, pp. 38–47, 2016.

[73] Z. Zhu, G. Fu, Y. Yang, Z. Yang, and P. Li, “Energy transfer, tunable luminescence, and thermal stability of Tb^{3+} Sm^{3+}-codoped $Na_3Bi(PO_4)_2$ phosphors,” *J. Mater. Sci.*, vol. 51, no. 14, pp. 1–11, 2016.

[74] J. Sun, X. Zhang, Z. Xia, and H. Du, “Synthesis and luminescence properties of novel $LiSrPO_4$:Dy^{3+} phosphor,” *Mater. Res. Bull.*, vol. 46, no. 11, pp. 2179–2182, 2011.

APPENDICES

Appendix A

Luminescence intensity comparision of microwave assisted solid state synthesis and solid state synthesis without urea

Luminescence intensity increases nearly two times in microwave assisted solid state synthesis with respect to solid state synthesis

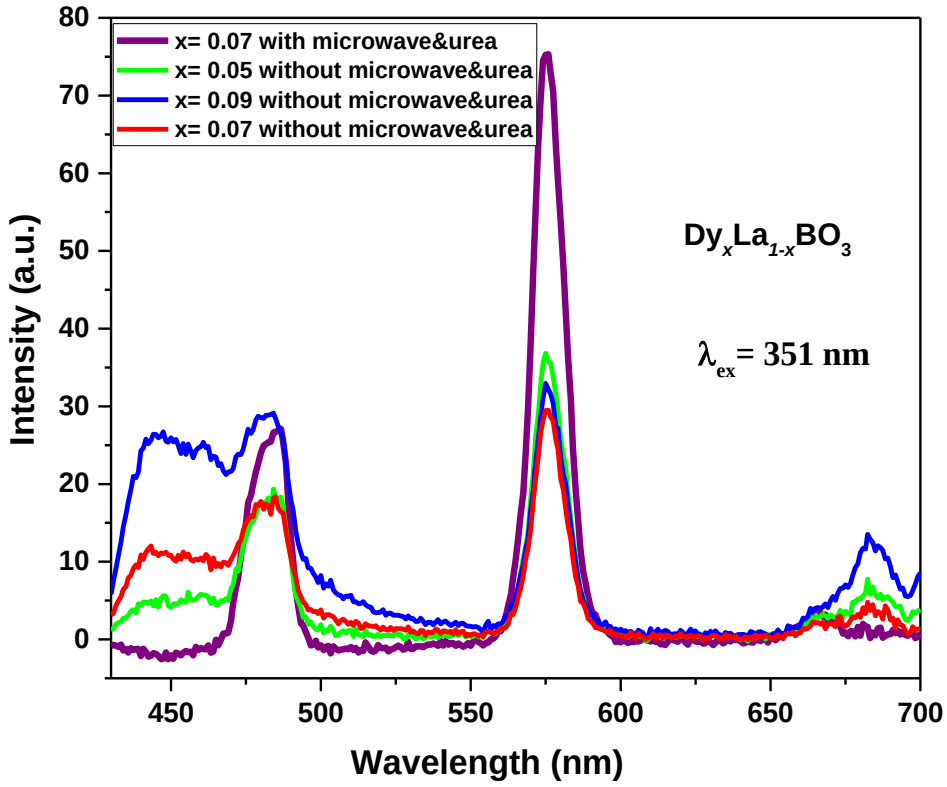

Figure A.1. Emission spectra of Dy^{3+} doped $LaBO_3$ with and without urea

Appendix B

Luminescence intensity comparision of $Dy_{0.07}La_{0.93}BO_3$ and $Dy_{0.09}Ce_{0.05}La_{0.88}BO_3$

In comparison with single Dy^{3+} doped sample, the $^4F_{9/2} \rightarrow {}^8H_{13/2}$ transition intensity of Dy^{3+} increases ten times in codoped sample

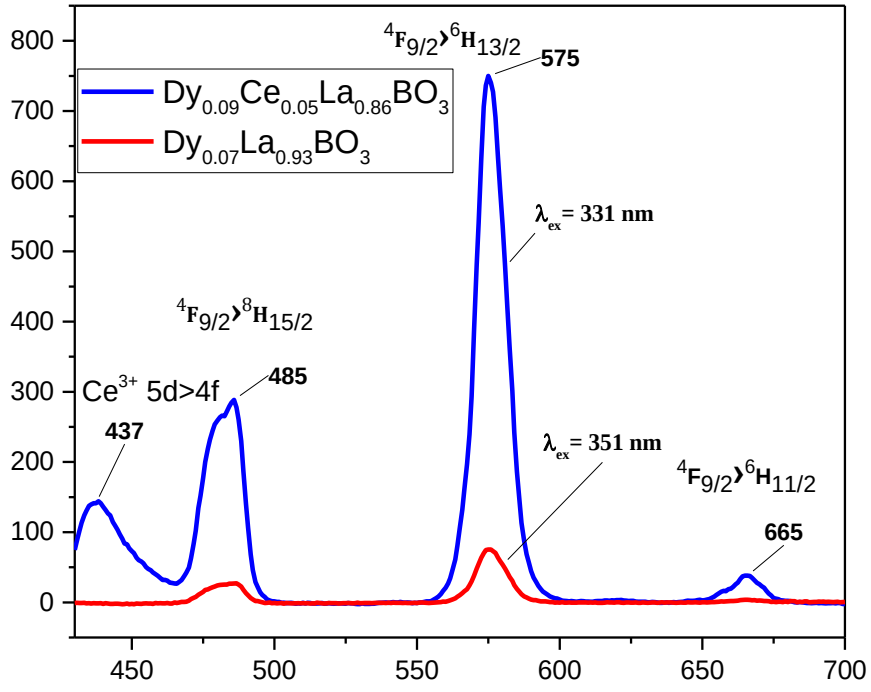

Figure B.1. Emission spectra of $Dy_{0.07}La_{0.93}BO_3$ and $Dy_{0.09}Ce_{0.05}La_{0.88}BO_3$

Appendix C

Luminescence intensity comparision of $Tb_{0.07}La_{0.93}BO_3$ and $Tb_{0.07}Ce_{0.05}La_{0.88}BO_3$

Compared to the single Tb^{3+} doped lanthanum orthoborate sample which is excited by 378 nm, emission band intensity of Tb^{3+} ion at 544 nm increases over thirteen times in Tb^{3+}/ Ce^{3+} codoped $LaBO_3$ sample

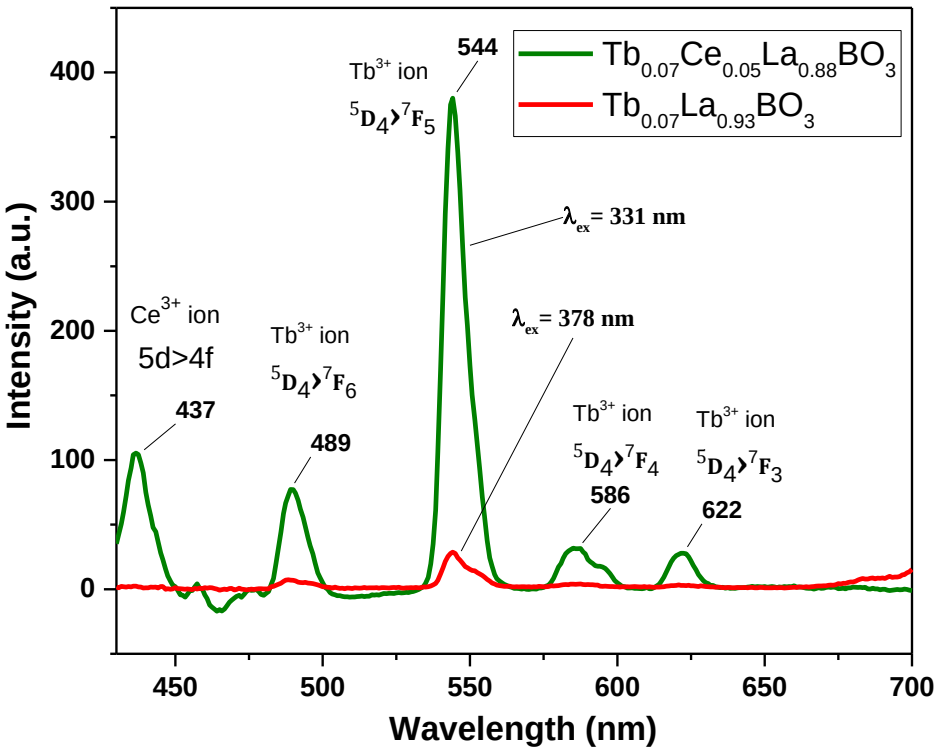

Figure C.1. Emission spectra of $Tb_{0.07}La_{0.93}BO_3$ and $Tb_{0.07}Ce_{0.05}La_{0.88}BO_3$

Appendix D

Summary of double exponential decay function fit parameters

Table D.1 Double exponential decay function fit parameters

Dopant (observed wavelength)	A_1	t_1 (ms)	t_1 (ms)	A_2	t_2 (ms)	t_2 (ms)	Statistics	t_{av} ms
	Value	Value	Std.Error	Value	Value	Std. Error	R-Square	
DyEu(575nm)	6961.144	0.395	0.01614	9442.513	1.030	0.01844	0.999	0.890
CeTb(489nm)	2882.130	1.300	0.08117	4798.130	2.880	0.07607	0.998	2.543
CeTb(622nm)	550.470	1.300	0.38967	962.164	2.950	0.35375	0.947	2.618
Dy(485nm)	9550.301	0.311	0.02968	14680.541	0.915	0.02983	0.996	0.805
Dy(665nm)	807.170	0.416	0.14256	970.277	1.000	0.17792	0.956	0.850
DyCe(485nm)	1848.933	0.283	0.04072	2738.635	0.937	0.04399	0.988	0.826
DyEu(485nm)	3665.991	0.356	0.02695	6464.280	0.932	0.02305	0.998	0.829
Eu(593)	2378.020	1.160	0.07994	3686.745	2.710	0.08152	0.996	2.375
Tb(489)	2804.042	0.382	0.01683	11222.960	2.740	0.010	0.999	2.661
Tb(622)	351.541	0.253	0.08646	1611.576	2.670	0.04915	0.950	2.621

Appendix E

Summary of single exponential decay function fit parameters

Table E.1. Single exponential deceay function fit parameters

Dopant (observed wavelength)	A_1	A_1	t_1 (ms)	t_1 (ms)	Statistics
	Value	Std. Error	Value	Std. Error	R-Square
CeTb(544nm)	21902.244	28.33759	2.28	0.00441	0.99864
Dy(575nm)	62890.834	210.87325	0.729	0.00333	0.99747
DyCe(575nm)	5507.583	35.08007	0.719	0.00622	0.99098
DyEu(575nm)	15069.513	50.47904	0.781	0.00362	0.9974
CeTb(489nm)	7358.024	14.7913	2.30	0.00691	0.99672
CeTb(622nm)	1446.461	12.03304	2.37	0.02962	0.94633
Dy(485nm)	21706.756	117.84805	0.714	0.00526	0.99345
Dy(665nm)	1651.098	23.69105	0.752	0.01480	0.95506
DyCe(485nm)	3997.626	33.69609	0.724	0.00830	0.98427
DyCe(665nm)	300.911	29.87376	0.748	0.10185	0.30594
DyEu(485nm)	9337.795	34.59123	0.750	0.00381	0.99688
DyEu(615nm)	2435.316	14.58164	1.77	0.01981	0.98789
Eu(593)	5765.789	14.67922	2.12	0.00797	0.99486
Eu(615)	8186.628	16.97169	1.91	0.00575	0.99667
Tb(489)	12288.979	24.37882	2.51	0.00757	0.99673
Tb(544)	1192.350	12.8042	2.54	0.04161	0.91211
Tb(622)	1697.648	13.67192	2.53	0.03105	0.94865